Universidade Federal de Pernambuco
Centro de Tecnologia e Geociências
Programa de Pós-Graduação em Engenharia Elétrica

Gabriel de Freitas Fernandes

Theory and Engineering Techniques in Metal Hydride Plasmonics for Hydrogen Sensing

Recife
2025

Gabriel de Freitas Fernandes

Theory and Engineering Techniques in Metal Hydride Plasmonics for Hydrogen Sensing

Tese apresentada ao Programa de Pós-Graduação em Engenharia Elétrica da Universidade Federal de Pernambuco, como requisito parcial para a obtenção do título de Doutor em Engenharia Elétrica.

Orientador(a): Prof. Joaquim Ferreira Martins Filho, Ph.D.

Coorientador(a): Ignacio Llamas-Garro, Ph.D.

Recife
2025

.Catalogação de Publicação na Fonte. UFPE - Biblioteca Central

Fernandes, Gabriel de Freitas.
Theory and Engineering Techniques in Metal Hydride Plasmonics for Hydrogen Sensing / Gabriel de Freitas Fernandes. - Recife, 2025.
164f.: il.

Tese (Doutorado) - Universidade Federal de Pernambuco, Centro de Tecnologia e Geociências, Programa de Pós-Graduação em Engenharia Elétrica, 2025.
Orientação: Joaquim Ferreira Martins Filho.
Coorientação: Ignacio Llamas-Garro.
Inclui referências.

1. Plasmônica; 2. Sensores ópticos; 3. Hidretos Metálicos; 4. Grades de difração; 5. Espectroscopia; 6. Fibra óptica. I. Martins Filho, Joaquim Ferreira. II. Llamas-Garro, Ignacio. III. Título.

UFPE-Biblioteca Central

GABRIEL DE FREITAS FERNANDES

"THEORY AND ENGINEERING TECHNIQUES IN METAL HYDRIDE PLASMONICS FOR HYDROGEN SENSING"

Tese apresentada ao Programa de Pós-Graduação em Engenharia Elétrica da Universidade Federal de Pernambuco, como requisito parcial para a obtenção do título de Doutor em Engenharia Elétrica, na área de concentração em Fotônica.

Aprovada em: 25/07/2025.

BANCA EXAMINADORA

Prof. Dr. Joaquim Ferreira Martins Filho
(Orientador e Examinador Interno)
Universidade Federal de Pernambuco

Prof. Dr. João Batista Rosolem
(Examinador Externo)
Centro de Pesquisa e Desenvolvimento da Telebras, CPQD

Prof. Dr. João Crisóstomo Weyl Albuquerque Costa
(Examinador Externo)
Universidade Federal do Pará

Profª. Dra. Valéria Loureiro da Silva
(Examinadora Externa)
SENAI-CIMATEC

Prof. Dr. Eduardo Padrón Hernández
(Examinador Externo)
Universidade Federal de Pernambuco

A minha avó Lenilde Ribeiro Lima e ao meu mestre Eduardo Fontana. Uma me alfabetizou em língua portuguesa, o outro em campos e ondas.

Agradecimentos

Devo meus agradecimentos a muitas pessoas que, direta ou indiretamente, contribuíram para minha jornada educacional e me permitiram chegar ao ponto de completar um doutorado.

Primeiramente, aos meus pais, Sérgio e Luciana, por terem sido, naturalmente, os primeiros e mais duradouros apoiadores da minha educação. Também agradeço à minha esposa, Angélica, e à minha enteada, Maria, pela compreensão quanto ao tempo necessário para me dedicar à tese e aos momentos de ausência. Agradeço aos meus colegas do Programa de Pós-Graduação em Engenharia Elétrica, Keila Santos, Alexandre Oliveira e Túlio Pedrosa, pelos debates e dicas trocados ao longo dos anos. Aos que foram meus coautores, José Otávio Maciel, Raoni Góes e Felipe Araújo, também estendo meus agradecimentos.

A principal pessoa a quem devo meus agradecimentos é o professor Eduardo Fontana. Estive sob sua orientação desde 2014, quando iniciei minha trajetória na pesquisa, e fui aprendendo com seu exemplo ao longo de dez anos de convivência. Sua forma de exercer a engenharia me moldou, e sei que o engenheiro que serei ao longo da vida sempre refletirá sua imagem. Sou muito grato pela dedicação que teve a mim, este professor que, mesmo nos momentos finais de sua vida, continuou acompanhando meu trabalho, expressando interesse quando eu obtinha algum resultado curioso e sempre disponível para debater tópicos de pesquisa. Espero ter tido, como aluno, ao menos uma pequena fração do impacto que ele teve sobre mim como professor.

Não posso deixar de externar meu agradecimento a Ignacio Llamas, por ter me recebido durante minha estadia em Castelldefels e me orientado no processo de fabricação dos chips baseados em grades de paládio. Agradeço-lhe imensamente por todo o apoio prestado após o falecimento do professor Fontana, nas revisões dos artigos e desta tese, mesmo quando isso não era sua obrigação. Espero poder retribuí-lo em colaborações duradouras.

Agradeço imensamente ao professor Joaquim por ter me aceitado como seu aluno, por sua orientação e por ter sido meu guia nos meses finais do meu doutorado. Reconheço a dificuldade de orientar uma tese estando presente apenas na reta final, e não poderia estar mais grato por sua ajuda. Se consegui entregar a tese e os artigos a tempo, muito se deve ao seu trabalho. Que esses últimos meses sejam o início de muitas colaborações futuras.

Também agradeço ao professor Henrique Patriota por sua valiosa colaboração na pesquisa referente a sensores de hidrogênio com fibras ópticas perfil D. Mesmo com apenas cerca de seis meses de pesquisa, foi possível modelar um sensor prático. Obter tal resultado em tão pouco tempo não teria sido possível sem sua colaboração.

Resumo

Theory and Engineering Techniques in Metal Hydride Plasmonics for Hydrogen Sensing

Gabriel de Freitas Fernandes

Esta tese propõe três técnicas em plasmônica de hidretos metálicos para aplicações em instrumentação e sensoriamento, todas essas técnicas são investigadas e simuladas computacionalmente. Primeiramente, é introduzido o Método de Minimização de Harmônicos, juntamente com uma estratégia de otimização para sensores plasmônicos baseados em grades de difração. Essa abordagem conecta formalismos de baixa complexidade a perfis de grade mais adequados para fabricação por métodos amplamente adotados, com um tempo médio de computação de apenas 8 segundos. Em seguida, é apresentada a técnica de Espectroscopia por Grade de Difração Plasmônica com Laser de Diodo Sintonizável (TDLPGS), propondo uma arquitetura de sistema para instrumentação plasmônica portátil aplicável à detecção de hidrogênio. Esse método aproveita a periodicidade variável da rede sob carga de hidrogênio, e os efeitos das variações ópticas e mecânicas nas propriedades plasmônicas do hidreto metálico são analisados em detalhes. Rotinas de detecção harmônica são aplicadas ao sinal de reflectância para melhorar a precisão das medições. Por fim, é proposta uma estrutura Óxido/Metal/Hidreto para integração com fibras ópticas em perfil D, visando o desenvolvimento de dispositivos de detecção de hidrogênio. A influência da espessura de cada camada é investigada, e uma rotina de otimização é sugerida para maximizar a sensibilidade sob restrições específicas de fabricação. O desempenho do sensor é avaliado por uma série de experimentos computacionais.

Palavras-chave: Plasmônica; Sensores ópticos; Hidretos Metálicos; Grades de difração; Espectroscopia; Fibra óptica.

Abstract

Theory and Engineering Techniques in Metal Hydride Plasmonics for Hydrogen Sensing

Gabriel de Freitas Fernandes

This thesis proposes three techniques in metal hydride plasmonics for instrumentation and sensing applications, all of them are investigated and simulated by computation. First, the Harmonic Minimization Method is introduced, along with an optimization strategy for plasmonic sensors based on diffraction gratings. This approach connects low-complexity formalisms with grating profiles that are more amenable to fabrication using widely adopted methods, achieving an average computation time of only 8 seconds. Next, the Tunable Diode Laser Plasmonic Grating Spectroscopy (TDLPGS) technique is presented, proposing a system architecture for portable plasmonic instrumentation suited for hydrogen sensing. This method leverages variable grating periodicity under hydrogen loading, and the effects of optical and mechanical variations on the metal hydride's plasmonic properties are thoroughly analyzed. Harmonic detection routines are applied to the reflectance signal to enhance measurement precision. Finally, an Oxide/Metal/Hydride structure is proposed for integration with D-shaped optical fibers to develop hydrogen sensing devices. The influence of each layer's thickness is investigated, and an optimization routine is suggested to maximize sensitivity under specific fabrication constraints. The device performance is acessed through a series of computational experiments.

Keywords: Plasmonics; Optical Sensors; Metal Hydride; Diffraction gratings; Spectroscopy; Optical fiber.

List of Figures

List of Tables

Index

Chapter 1

Introduction

The problem of building portable instrumentation systems based on Surface Plasmon Resonance (SPR) consists of a significant engineering challenge. There are three experimental configurations that permit the observation of such effect, that is the Kretschmann (Kretschmann,1971), Otto (Otto,1968a) and diffraction grating configurations, with the first two being coupling prism-based setups with the use of planar metallic surfaces. Most commercial stage devices are based on the Kretschmann configuration, due to its simplicity of fabrication when compared to the Otto setup, in which a dielectric layer of the order of the incident wavelength has to be fabricated, or the grating configuration in which a periodic structure has to be manufactured. However, to obtain sharp resonances with prism-based architectures it is needed to employ angular variation, a procedure that represents a major difficulty in terms of building a portable system since it requires moving parts. In a fixed wavelength operation, no moving parts would be necessary, however, the presence of the prism widens the resonance to a point where broadband light sources and detectors need to be employed, considering that these equipment are bulky and hard to integrate into an embedded measurement system, this represents another impracticality. The grating configuration on the other hand permits the narrowing of the resonance compared to thin film-based architectures due to optical feedback on the periodic surface. Based on this fact, the hypothesis of measuring, at least, the most sensitive part of the resonance with Distributed Feedback (DFB) lasers,

in both thermal and electrical modulation schemes, is investigated in order to obtain a system architecture that operates in a fixed angle setup without the need for broadband sources. The investigation of the validity of this hypothesis represents the first objective of this thesis.

Since the grating resonance position is very sensitive to periodicity changes, an application in which the measured analyte causes a structural change on the grating would be adequate. Considering this intrinsic feature of our system, the application of hydrogen sensing is mainly investigated by the employment of hydride-forming metals such as Pd and Nb. These materials, when in contact with the hydrogen gas, undergo modulation of their dielectric function and lateral and vertical mechanical expansion. With the concentration of the gas being directly related to the periodicity change, this application is appropriate since it benefits an intrinsic feature of the system proposed here.

This thesis presents a system architecture for a practical and portable device that employs a DFB laser capable of operating under two regimes. First, thermal control is proposed to achieve linear spectral variation, enabling the identification of the most sensitive part of the spectrum. This approach could be employed with gratings in gold (Au) or silver (Ag), materials for which narrower resonances are expected. Additionally, a sinusoidal wavelength modulation scheme is introduced through modulation of the injection current. While thermal control has been previously suggested for fast switching in a communication context (Ueno et al., 2015), to the best of the author's knowledge, its use for interrogating plasmonic devices has not been explored.

The proposed technique is then applied to the sensing of hydrogen gas (H_2) using palladium (Pd) and niobium (Nb) optimized gratings, metals known to form hydrides in the presence of this gas, resulting in optical and structural variations. This application is selected due to the critical need for monitoring H_2 in various industries (Le et al., 2023), as well as the challenges associated with handling the gas. Hydrogen has a Lower Explosive Limit (LEL) of only 4% volume concentra-

tion, being a small molecule with a high risk of leakage, and poses significant safety concerns in its storage and transportation. Additionally, when ignited, its flame is invisible (PubChem, 2025; Yang et al., 2021). There is also an increasing necessity for technologies to store and measure hydrogen gas concentration due to its applicability as a combustible in a renewable energy scenario. Another motivation is the exploration of periodicity changes in the grating when the film is exposed to hydrogen, which increases sensitivity.

In contrast with other spectroscopy techniques such as Wavelength Modulation Spectroscopy (WMS) (Li et al., 2013; Avetisov et al., 2019; Liu et al., 2020) and its variations, such as crystal tuning fork-enhanced spectroscopy (Xu et al., 2020; Angstenberger et al., 2025; Ma et al., 2024) and off-axis integrated cavity spectroscopy (Yu et al., 2023), based on light absorption by the target molecule, the proposed technique in this work consists in the absorption of gas by the grating itself and subsequent interrogation of its plasmonic resonance.Our approach also contrasts with previously suggested H_2 sensors that utilize periodic structures, such as Pd-coated Fiber Bragg Gratings (FBGs), which detect the presence of the gas by measuring the strain caused by hydrogen absorption and its effect on the internal grating periodicity. In this work, the material loaded with the gas serves as the periodic structure, leading to a more direct transducing mechanism (Sutapun, 1999; Trouillet et al., 2006; Silva et al., 2013). According to the author's knowledge, this is the first detailed analysis of optical and mechanical variations on plasmonic sensing properties of metallic hydrides.

It is shown that a system architecture compatible with a portable, embedded system can achieve high linearity and, depending on the choice of material, a sub-ppm limit of detection.

Optimized structures are employed, and the technique is investigated through analytical models that account for gas diffusion in the metals, the dielectric function of the hydride, and the elastic expansion of the films. Numerical simulations are employed to validate the technique and provide calculations of the diffracted fields.

Considering computational methods for obtaining optimal grating structures for different geometries, the Harmonic Minimization Method (HMM) (Fernandes et al., 2025) is proposed. The challenge of describing reflection and transmission in diffraction gratings dates to early 20th-century research by John William Strutt, better known as Lord Rayleigh (Rayleigh, 1907). His approach, known as Rayleigh's hypothesis, assumes that fields inside and outside the grating valleys are composed by a sum of plane waves. While this is an approximation disregarding field concentration in the valleys, it generally applies to low-amplitude sinusoidal gratings, following studies such as those by van den Berg et al. (van den Berg e Fokkema, 1979; van den Berg, 1981) that examined the hypothesis's validity, showing its accuracy when the grating amplitude-to-periodicity ratio remains below 0.142521 (Millar, 1969). Considering its simplicity, it is not costly in terms of computational resources to implement it.

Among other techniques to model the optical response of diffraction gratings, the Rigorous Coupled-Wave Analysis (RCWA) method is notable. RCWA divides the periodic region into sections, using a Fourier series field description within the grating and a Fresnel reflection approach outside of it. This approach requires solving an infinite linear system for each section and polarization state, adding significant computational complexity. However, RCWA involves no approximations in its calculations, making it a rigorous algorithm. Stability and energy conservation analyses has been conducted (Moharam e Gaylord, 1982). Extensions to RCWA have included general polarization and material loss effects (Moharam e Gaylord, 1983a), as well as 3D diffraction field calculations (Moharam e Gaylord, 1983b). The RCWA method is also suitable for simulating metallic diffraction gratings, as shown in previous studies (Moharam e Gaylord, 1986), and has been used in grating-based plasmonic device research (Lyaschuk et al., 2021).

An alternative method, developed in 1980 and known as the Chandezon or C method, models fields as plane wave expansions within a curvilinear coordinate system where the interface profile becomes flat (Chandezon et al., 1980). This ap-

proach is particularly effective for arbitrary profiles and can also deal with rectangular profiles with the benefit of requiring only a single infinite linear system solution. Compared to RCWA, which solves separate systems for each grating slice, the C method's single system allows faster convergence, as observed in studies (Vallius, 2002; Edee et al., 2013). Enhanced convergence techniques have also been developed, such as alternative variable transformations (Xu e Li, 2014), piecewise linear parametrization for deep gratings (Xu e Li, 2015), and preconditioning for efficient convergence (Xu e Li, 2017). Other refinements, such as adaptive spatial resolution (Granet et al., 2001) and Fourier factorization for handling sharp profile edges (Li e Chandezon, 1996), can further improve accuracy. This method has been applied in optical design across varied structures, including asymmetric, overhanging, and multicoated gratings (Plumey et al., 1997; Preist et al., 1997; Chandezon et al., 1982).

This thesis also investigates the feasibility of combining a design algorithm based on the Rayleigh method, due to its lower complexity, with a profile translation strategy (De Freitas Fernandes et al., 2024). This strategy would input purely geometric information about the grating without requiring additional electromagnetic calculations. An algorithm is developed to minimize the difference between the sinusoidal profile function and a desired grating profile, described by a Fourier series, as a function of the number of harmonics used in the desired profile's description while assuring that the new structure is the most sensitive one for the newly obtained grating profile. In this work the Harmonic Minimization Method (HMM) is developed to translate a pre-designed sinusoidal grating into diffraction gratings with rectangular and triangular profiles. The HMM can be instrumental in adapting grating profiles to different fabrication processes and technology. This can be particularly useful in a very practical situation considering that the Rayleigh description of diffraction consists in the lowest computationally complex one, but only produces trustworthy optimized plasmonic structures in sinusoidal profile. From a fabrication point of view, a sinusoidal grating can be fabricated with the relatively simple mask-

less procedure named Interference Lithography (Jang et al., 2007; Vala e Homola, 2014; Guo et al., 2006) but this technique is not widely used in clean room facilities since it is not adequate for fabricating different profiles or other optical and electronic structures and devices, like mask based optical or electron beam lithography. HMM can connect the formalism with lowest computational complexity with structures craftable by more widely employed semiconductor batch fabrication techniques, without adding significant computational cost to the design process. This approach permits the design of multiple structures with different profiles from one single sinusoidal structure, facilitating the sensitivity analysis of different profiles and fabrication adequacy of the designed device in a situation in which the employment of the other previously cited methods would require the execution of spectral calculations for each structure.

This work discusses the optimization strategy based on the Rayleigh and the C method, as well as the geometrical aspects of the diffraction integral that lead to the HMM. The method is applied to the design of five rectangular palladium (Pd) gratings and one triangular niobium (Nb) grating in the context of creating hydrogen gas (H_2) sensitive devices. The HMM is evaluated in terms of computational complexity, convergence, and the resulting gratings are compared with those designed using the C method under identical input parameters, particularly regarding their performance as transducer elements. It was observed that the HMM algorithm achieved execution times on the order of seconds, and the resulting gratings exhibited sensitivities comparable to those designed using the C method. One particular designed Pd structure in rectangular profile is fabricated and characterized in terms of its amplitude and periodicity. The rectangular profile is chosen to demonstrate a simple grating structure implemented using well known and highly accessible batch semiconductor fabrication processes, suitable for mass production. The spectrum and sensitivity of a grating with the nominal parameters are compared to that of a device with the characterized parameters in a computational environment.

Beyond grating-based architectures, this thesis also investigates Oxide/Metal/Hydride

(OMH) structures for D-shaped optical fibers(da Silva et al.,2021). Fiber-based optical sensors have the practical advantage of easier adaptability and mechanical integration to the environment to be measured when compared to the spectroscopy technique also suggested in this thesis. The D-shaped structure is a type of fiber structure in which part or the totality of the cladding is removed in a particular section of the fiber in order to permit the beam traveling in the fiber's core to interact with the external medium. Metals such as Pd and Nb can be used to ensure specificity to hydrogen gas, but they present poorer plasmonic properties compared to materials such as Au and Ag. Based on this fact, the structure proposed involves the use of a two-metal layer, one chosen to enhance the sensitivity of the device, in this case, Au is employed, and another metal to permit hydrogen specificity. Another layer between the cladding and the bi-metal structure is important, that is the oxide layer. In our work, TiO_2 is used considering its higher refractive index than typical values for fiber optic cladding materials to shift the Kretschmann plasmonic resonance, which usually is observed on the visible spectrum under incidence around 85° to the infrared. That layer is important to obtain the response of the sensor on the low-loss region of a commercial single-mode fiber optic, facilitating the fabrication of the device.

Computational experiments are conducted to explore the effect of each layer thickness on the sensitivity of the device and subsequently, an optimization strategy based on first principles and a recursive gradient procedure is proposed, with fabrication constraints being inputs for the designer to choose. With such a method, a particular structure is investigated numerically by the use of the FEM in which its response is obtained under the LEL. Harmonic detection is also proposed with this sensor and FFT-based and Lock-in amplifier-based detection schemes are simulated to obtain higher linearities between 0% and 4% hydrogen gas concentration. An analysis of the limit of detection of such a sensor is also conducted.

This thesis follows a slightly different order from the chronological one exposed in this section. Initially, a systematic literature review is presented to expose the cur-

rent state of the technologies already reported that are important to this work. The document follows with the development of the Harmonic Minimization method and fundamental aspects of diffraction theory. Subsequently, the Tunable Diode Laser Plasmonic Grating Spectroscopy (TDLPGS) technique is presented and computationally validated. Following this, the fiber-based devices are presented and their computational validation is explained. The thesis contains a conclusion chapter in which the overall conclusions of the thesis are presented, including future works where open questions are discussed.

Chapter 2

Systematic Literature Review

Surface plasmon resonance-based sensors have been widely explored by the scientific community, resulting in numerous applications and devices developed from an academic perspective. This topic has become a field of considerable scope, evidenced by the volume of published works, the emergence of conferences, and specialized journals. Surface plasmon resonance is observed in three different configurations, two of which involve coupling prisms, known as the Kretschmann and Otto configurations. A third method for achieving this coupling is through metallic diffraction gratings. In this case, due to the structure's geometry, which provides optical feedback through retroreflection of the surface-propagating mode, the resonance exhibits higher quality factors in both angular and wavelength domains.

2.1 Diffraction Grating-based Plasmonic Sensors

Historically, the Kretschmann configuration has been widely adopted for practical sensor construction and is characterized by a three-layer structure: Prism/Metal /Dielectric (Kretschmann, 1971). Several portable devices based on this configuration have been documented in the literature for both angle-resolved and wavelength-resolved measurements (Masson, 2020; Yesudasu et al., 2021). Notable examples include the *Biacore*, developed by the company of the same name and introduced

commercially in 1990, and SPREETA, developed by *Texas Instruments*. These devices require precise alignment, and measurement quality depends heavily on the opto-mechanical system used. Technologies based on this configuration tend to be bulky and challenging to integrate with other systems.

The Otto configuration (Otto, 1968a), characterized by a Prism/Dielectric/Metal structure, has been largely avoided, likely due to the challenge of manufacturing a sensing channel between the prism and metal medium that maintains effective coupling. This spacing must be on the order of the incident wavelength; considering that the absorption peak of noble metals, such as Au, lies in the near-infrared range, the channel must be on the scale of microns. To the author's knowledge, only one device based on this configuration has been fabricated and documented in the literature (Fontana et al., 2015; Maciel-Neto et al., 2022; Neto et al., 2016; Lee et al., 2018).

Diffraction grating coupling can be observed in both the angular and spectral domains. Focusing on the angular domain, several works have proposed biosensors using angular interrogation, including applications in protein detection (Unfricht et al., 2005), biomolecular interaction analysis (Dostálek e Homola, 2008), and tumor necrosis factor (TNF-α) detection (Hoa et al., 2009). Theoretical studies on the effect of azimuth angle in angular spectra (Kim, 2005) and comparisons of transducer performance between thin film structures and grating-based equivalents (Alleyne et al., 2007) have also been reported. Notably, grating structures are known to achieve narrower resonances compared to planar interfaces. Various modes of operation have been proposed, such as the double dip method (Cai et al., 2008), which uses the separation between different diffraction orders as a transducing mechanism. Aluminum (Al) gratings have been investigated in angular interrogation mode, including studies on the effects of oxide layers (Sun et al., 2015). Palladium (Pd) gratings have also been explored computationally for hydrogen gas sensing via angular interrogation (Lin et al., 2008).

Beyond single-metal structures, double-layer metal gratings have been suggested,

such as silver (Ag) gratings over gold (Au) substrates (Bijalwan e Rastogi, 2017) and Au/Al_2O_3 gratings for enhanced sensitivity (Bijalwan e Rastogi, 2018). Double-layer structures have also been investigated for hydrogen detection, with Pd over typical plasmonic metals like Au, Ag, and Al (Bijalwan e Rastogi, 2019). Au/Ag structures with angular interrogation were experimentally validated for ethanol concentration sensing (Chen et al., 2020).

In the context of wavelength interrogation in grating structures, periodic structures such as plasmonic nanoholes have been proposed and experimentally validated for extraordinary optical transmission (EOT) (Brolo et al., 2004; Srivastava e Abdulhalim, 2015). EOT has been applied for ethanol detection (Karabchevsky et al., 2009). Au nanocubes over an Au film have also been reported as a means to implement a 2D diffraction grating (Wang et al., 2019). All-metal gratings with optimized design have been suggested (Yoon et al., 2006), as well as narrow groove structures (Dhawan et al., 2011) and deep gratings based on magnetic polariton resonance (Xu et al., 2013; Zhu et al., 2018). Single metal gratings have been explored for dispersion engineering in the Kretschmann configuration (Arora et al., 2018), and double groove gratings were simulated for refractive index sensing (Li et al., 2017). Graphene-based diffraction gratings integrated with Fabry-Pérot cavities have also been researched (Yan et al., 2019).

Chiral nanoparticle grating structure over a metallic substrate was also proposed as a biosensor with mM (mili-Molar) detection limit for D-glucose(Kim et al.,2024). Wavelength interrogation was also used to monitor the peak transmittance of gratings fabricated on a flexible substrate in order to transduce strain signals(Bdour e Sabat,2024). Flexible substrates were also employed for a wearable grating device operating as a refractive index sensor with very narrow (6.9 nm) linewidth(Chai et al.,2025). Grating structures over D-shaped optical fibers were also computationally studied as refractive index sensors(Osamah et al.,2024;Seliem e Abdellatif,2024). Metal gratings embedded on a dielectric medium over a metallic plane structure were also computationally studied and suggested to obtain self-referenced refractive index

sensors(Rao et al.,2025).

Another interrogation method that can be employed with diffraction-based plasmonics is the phase interrogation method. This method consists of measuring the phase difference between the insensitive to plasmonic coupling s-polarized light and the p-polarized beam. The typical experimental setup involves a few complexities that are probably the reason such an interrogation method is not widely used, such as a rotational stage for azimuthal angle control and optical components such as quarter-wave plates, polarizers, and phase-sensitive detectors. This interrogation procedure is usually susceptible to mechanical vibrations and makes it difficult to develop portable systems. Nonetheless, there were works related to the use of this interrogation method for diffraction gratings, such as the real-time detection of living cells with a gold grating with 633 nm laser incidence(Borile et al.,2019), to perform a biorecognition assay using the effective avidin/biotin reaction (Ruffato et al.,2013) and the implementation of a lab-on-a-chip platform with the enhancement of Surface Acoustic Waves (SAW)(Sonato et al.,2016).

For hydrogen gas sensing, Pd-coated Au gratings have been proposed (Subramanian et al., 2020). Theoretical analyses of resonant waveguide gratings have been conducted to clarify the sensing properties of these structures (Lu et al., 2019). Gratings with a metal layer over a gain medium, such as GaN, were simulated for transducing behavior (Sharma e Pandey, 2019), and a pressure sensing device with a 0-1 kPa detection range was also developed (Mansouri et al., 2020). There were also investigation and proposal concerning the employment of Pd for subwavelength hole arrays for H_2 sensing [111, 115, 116].

Regarding mathematical models and computational analysis of plasmonic grating-based sensors, an analytical model for device sensitivity in wavelength interrogation was developed (Cao et al., 2019), along with a comparative study between sinusoidal and rectangular gratings (Iqbal et al., 2020). Additionally, a method based on coupled mode theory was proposed for plasmonic structures in the near-infrared spectrum (Jeddi Golfazani et al., 2020).

2.2 Distributed Feedback Lasers for Spectroscopy Applications

Within the scope of this thesis, it is important to highlight previous works employing Distributed Feedback (DFB) lasers in spectroscopy systems, using both thermal and current-controlled approaches. For current modulation, typical values for the current modulation coefficient are on the order of 10^{-2} nm/nA, though this method also causes variation in the emitted laser intensity. In thermal control, typical values for commercial devices are on the order of 10^{-1} nm/°C.

To achieve the necessary spectral sweep, other light sources could also be considered, such as MEMS-VCSEL lasers (Microelectromechanical Systems Vertical Cavity Surface Emitting Lasers). These devices, in their commercial form, offer a large wavelength range, exemplified by models like the SL101081 manufactured by Thorlabs® (Thorlabs, 2023). However, MEMS-VCSEL lasers tend to be bulkier and more expensive than DFB lasers, making them more challenging to integrate into practical and portable sensors and substantially increasing the overall cost. Commercial DFB lasers are also more commonly available at operating wavelengths that align with the absorption lines of many molecules of interest.

DFB lasers have been employed in wavelength-sweeping mode to investigate diffraction grating-based devices, such as FBG (Fiber Bragg Grating) sensors, where diffraction gratings are fabricated in the core of an optical fiber (Shlyagin et al., 2013; Carvalho et al., 2012; Bautista-Morales et al., 2018) and in microfabricated diffraction gratings on silicon (Grego et al., 2012). This type of device has also been used to investigate mechanical resonators (Kissinger et al., 2017).

A specific case of thermal control for DFB lasers in spectroscopy was demonstrated for studying the absorption spectra of deuterated water molecules HDO and D_2O using a 1.5 μm device (Ohshima e Sasada, 1989). In this case, a Peltier cooler was employed to achieve a temperature scan from -5°C to 80°C.

The majority of studies employing DFB lasers for infrared spectroscopy utilize

some form of wavelength modulation. Modulated wavelength incidence has been extensively explored to significantly enhance absorption sensitivity in these systems (Moses e Tang, 1977; Silver, 1992; Supplee et al., 1994). This technique typically involves current modulation at frequencies on the order of kHz, resulting in wavelength- and intensity-modulated emission that is more sensitive to the absorption lines of target molecules. Such methods have been explored in applications like combustion diagnostics and flammable gas detection (Bolshov et al., 2015; Kluczynski et al., 2012; Neethu et al., 2014), including in calibration-free systems (Sun et al., 2013; Upadhyay et al., 2017; Zhao et al., 2016). These techniques are also valuable in molecular spectroscopy, targeting molecules like HCN isotopes (Sasada, 1988), and can be enhanced with cavity-based optical feedback for increased sensitivity (Yang et al., 2022; Beaumont et al., 2024).

Designing and constructing DFB lasers specifically for spectroscopy applications is a topic of interest in the literature. Devices have been reported across a wide wavelength range (Zeller et al., 2010), with tunable lasers proposed in ranges such as 2.27-2.39 μm (Wang et al., 2019) and 2.28-2.43 μm (Wang et al., 2017). The development of Quantum Cascade DFB lasers enabled operations at wavelengths like 8.7 μm and 9.4 μm (Lee et al., 2007; Lee et al., 2009). DFB cascade lasers grown on Si were also suggested for methane spectroscopy applications with emission around 3.5 μm, this device was included in a quartz-enhanced spectroscopy setup with detection of 400 ppm of CH_4 concentration (Díaz-Thomas et al.,2025). DFB lasers based on organic materials have also been proposed for optical wavelength spectroscopy (Klinkhammer et al., 2010), their integration into compact spectroscopy systems (Woggon et al., 2010), and as excitation sources in Raman spectroscopy (Liu et al., 2013).

Notably, most works in the literature utilize injection current-based control. Thermal control, on the other hand, has been explored for agile switching in optical communications (Tabares et al., 2022; Ye et al., 2022; Polo et al., 2014), as well as for generating ultra-short pulses (Calvani et al., 1995). Consequently, the applica-

tion of thermal control for spectral sweeping of DFB lasers to investigate resonant devices represents a gap in the literature, especially for interrogating the RPS effect in any experimental configuration.

2.3 Diffraction Grating Modelling and Optimization

The challenge of describing reflection and transmission in diffraction gratings dates to early 20th-century research by John William Strutt, better known as Lord Rayleigh (Rayleigh, 1907). His approach, known as Rayleigh's hypothesis, assumes that fields inside and outside the grating valleys are composed of plane wave sums. While this is an approximation—disregarding field concentration in the valleys—it generally applies to low-amplitude gratings. Studies such as those by van den Berg et al. (van den Berg e Fokkema, 1979; van den Berg, 1981) examined the hypothesis's validity, showing its accuracy when the grating amplitude-to-periodicity ratio remains below 0.142521 (Millar, 1969). Sinusoidal plasmonic grating optimizers, like SPRinG, have been developed in UFPE's Sensors and Instrumentation Laboratory using a Lorentzian approximation paired with gradient optimization (de Melo, 2013), as well as metaheuristic algorithms like PSO (Particle Swarm Optimization) (de Araujo et al., 2023).

Among other techniques to model the optical response of diffraction gratings, the Rigorous Coupled-Wave Analysis (RCWA) method is notable. RCWA divides the periodic region into sections, using a Fourier series field description within the grating and a Fresnel reflection approach outside of it. This approach requires solving an infinite linear system for each section and polarization state, adding computational complexity. However, RCWA involves no approximations in its calculations, making it a rigorous algorithm; the field error between grating and external regions typically serves as the stopping criterion for RCWA algorithms (Moharam e Gaylord, 1981). RCWA has since been applied to various grating profiles—sinusoidal, triangular,

rectangular, and sawtooth—with stability and energy conservation analyses to validate the results (Moharam e Gaylord, 1982). Extensions to RCWA have included general polarization and material loss effects (Moharam e Gaylord, 1983a), as well as 3D diffraction field calculations (Moharam e Gaylord, 1983b). The RCWA method is also suitable for simulating metallic diffraction gratings, as shown in previous studies (Moharam e Gaylord, 1986), and has been used in grating-based plasmonic device research (Lyaschuk et al., 2021). Many commercial software packages implement RCWA, such as OmniSim by Photon Design, DiffractMOD by Synopsys, and Lumerical by Ansys, which includes an RCWA module for diffractive element simulation and design.

An alternative method, developed in 1980 and known as the Chandezon or C method, models fields as plane wave expansions within a curvilinear coordinate system where the interface profile becomes flat (Chandezon et al., 1980). This approach is particularly effective for arbitrary grid profiles, providing high accuracy for rectangular profiles and requiring only a single infinite linear system solution. Compared to RCWA, which solves separate systems for each grating slice, the C method's single system allows faster convergence, as observed in studies (Vallius, 2002; Edee et al., 2013). Enhanced convergence techniques have also been developed, such as alternative variable transformations (Xu e Li, 2014), piecewise linear parametrization for deep gratings (Xu e Li, 2015), and preconditioning for efficient convergence (Xu e Li, 2017). Other refinements, such as adaptive spatial resolution (Granet et al., 2001) and Fourier factorization for handling sharp profile edges (Li e Chandezon, 1996), further improve accuracy. This method has been applied in optical design across varied structures, including asymmetric, overhanging, and multicoated gratings (Plumey et al., 1997; Preist et al., 1997; Chandezon et al., 1982).

The Boundary Integral Method, also known as the Method of Moments, offers another approach by transforming differential equations into integral equations at the boundary, allowing precise Green's function computations (Harrington, 1993; Gibson, 2021). This rigorous method has been applied to calculating diffraction

efficiency in X-ray spectra (Goray et al., 2018) and includes GPU-optimized techniques for both direct and inverse diffraction problems (Goray e Dashkov, 2020).

For thin structures, an approximate method based on Green's functions is useful. This approach addresses Rayleigh anomalies, which occur at the transition between propagation and evanescence of diffraction orders, and Wood anomalies, associated with leaky mode excitation in the grating (Travo et al., 2017). This technique has been applied to describe molecular diffraction effects (Brand et al., 2015).

The Generalized Source method, proposed for diffraction grating modeling, iteratively calculates field distribution by generalizing the field source to simplify calculations, which are then primarily analytical (Tishchenko, 2000). This method enhances RCWA and C method precision, particularly when adapted to a curvilinear coordinate system, making it effective even for gratings with sharp edges (Shcherbakov e Tishchenko, 2013; Shcherbakov, 2019).

Legendre polynomial expansion is another approach, providing stable field equations without numerical instability issues (Khavasi et al., 2007; Chamanzar et al., 2006). This method was later adapted for complex grating shapes by subdividing the grating region into smaller, periodic subgratings, enabling effective field approximation with fewer Legendre functions (Khavasi et al., 2008).

Real devices often exhibit fabrication imperfections, requiring models that account for random roughness and periodicity deviations. Proposed methods to address these include the application of Heisenberg's uncertainty principle (Chandezon et al., 2019), analyses of curved profiles and amplitude variations (Torcal-Milla et al., 2010), and evaluations of slit randomness in near and far fields (Torcal-Milla e Sanchez-Brea, 2016) as well as random fill factors (Torcal-Milla e Sanchez-Brea, 2017).

For accurate reflection modeling in gratings, Finite Element Method (FEM) (Bathe, 2008; Bao et al., 2005) and Finite Difference Time Domain (FDTD) (Oskooi et al., 2010) can be used, though they demand significant computational power. FEM is particularly employed in topology optimization and has also been applied

to the design of dielectric metasurface networks (Ans et al.,2024). For grating design, associating these calculations with optimization routines may become impractical due to computational intensity. Nevertheless, FEM and FDTD provide valuable computational validation for proposed designs and experimental setups.

2.4 Hydrogen Sensors

The measurement of hydrogen gas concentration and the detection of leaks have been critical challenges across various industries. However, these concerns have become even more significant with ongoing efforts to develop production techniques and expand the use of hydrogen as an energy source (Le et al., 2023), particularly because it can be produced in an environmentally friendly manner and is considered a clean fuel. Despite its advantages, handling hydrogen gas presents several challenges. Notably, it has a low Lower Explosive Limit (LEL) of just 4% by volume, making it highly flammable. Additionally, hydrogen is a small molecule (PubChem, 2025) with a high diffusion potential, allowing it to escape through small openings, which poses risks during transportation and storage. Another hazardous characteristic of H_2 is that its flames are nearly invisible when combusted, making the visual identification of combustion particularly difficult.

An important aspect of hydrogen transportation through pipelines is the implementation of Leakage Detection Systems (LDS) (pip, 2016). Rather than relying on a direct hydrogen gas sensor, these systems use pressure measurements combined with computational calculations to estimate the amount of gas leaked. Such instruments can be installed in hydrogen pipelines, providing indirect leakage detection (Korlapati et al., 2022). Many devices of this category have already reached the commercial stage.

A key mechanism for hydrogen gas transduction involves chemiresistive and electrochemical sensors, which are notable for their simplicity and potential cost-effectiveness (Koo et al., 2020; Huang et al., 2024). Commercial devices of this type represent the state-of-the-art technology for practical hydrogen sensing systems.

Electrochemical sensors operate by utilizing materials that, upon contact with hydrogen gas, trigger a redox reaction. The resulting current is then measured to determine the gas concentration (Korotcenkov et al., 2009). However, these sensors have certain drawbacks, including susceptibility to measurement inaccuracies due to variations in relative humidity and cross-sensitivity to other gaseous molecules, such as oxygen.

Chemiresistive sensors, on the other hand, function by detecting changes in electrical resistance when a reaction with H_2 occurs. In this category, nanowire-based devices have been proposed in the literature, employing hydriding metals such as palladium (Pd) and platinum (Pt) (Penner, 2017; Yang et al., 2010; Weber et al., 2018). Additionally, Semiconductor Metal Oxide (SMO) sensors have emerged as a viable option for hydrogen detection (Luo et al., 2017; Luo et al., 2021). Among the most commonly used metal oxides in semiconductor-based hydrogen sensors are zinc oxide (ZnO), stannic oxide (SnO_2), tungsten trioxide (WO_3), niobium pentoxide (Nb_2O_5), and titanium dioxide (TiO_2) (Zhang et al., 2013; Zhao et al., 2011; Mondal et al., 2014; Wang et al., 2025a; Wang et al., 2025b).

Another interesting device is the Quartz Tuning Fork (QFT) based electromechanical hydrogen sensor. This device is based on the effect of the gas medium viscosity on the oscillation frequency of the QFT under electrical stimulus, it provides a full range (10%-100%) measurement range with low cost of fabrication and employing a very simple setup (Li et al., 2025).

Another important class of hydrogen sensors is optical sensors. A widely used approach for measuring H_2 concentration involves employing metals, with the vast majority of these sensors relying on the plasmonic properties of such materials. Various plasmonic structures have been investigated in the past.

For devices based on nanoparticles (NPs), several studies have explored direct H_2 absorption through metals such as palladium (Pd), magnesium (Mg), vanadium (V), zirconium (Zr), and titanium (Ti), particularly in nanodisk geometries (Palm et al., 2018). Additionally, gold (Au) nano-hemispheres have been investigated for

their ability to induce molecular dissociation through hot electron generation, leading to the formation of AuH_x hydrides (Sil et al., 2014). Pd NPs have also been combined with fluorine-based polymers to enhance H_2 diffusion (Östergren et al., 2021). Disordered Pd NPs over a Ag film were also proposed as a sensing platform capable of monitoring concentrations between 0%-4% (Yang et al., 2025).

Furthermore, yttrium (Y) nanorods have been studied as active plasmonic antennas, demonstrating significant reversibility (Strohfeldt et al., 2014). The thermodynamics and hysteresis of PdH_x formation have been analyzed concerning the shape and size of Pd NPs (Syrenova et al., 2015). To mitigate hysteresis effects, alloys of Pd with other metals such as Au, Ag, and Cu have been proposed (Nugroho et al., 2018; Matuschek et al., 2017; Wadell et al., 2015; Nugroho et al., 2016). Additionally, bi-metallic structures, such as nanodisks, have also been explored (Strohfeldt et al., 2015).

Optical fiber-based hydrogen sensors are among the most commonly used structures for practical hydrogen detection. The first sensor of this type was an interferometric sensor, proposed by Butler in 1984 at Sandia National Laboratories (Butler, 1984). This device utilized a titanium/palladium (Ti/Pd) coating on a single-mode fiber (SMF), where the metallization allowed the fiber to expand upon hydrogen absorption in the Pd layer, thereby increasing the optical path length of the signal arm. Since then, numerous optical fiber technologies have been developed, incorporating different sensing principles, materials, and sensor structures to enhance performance and reliability.

An interferometric sensor utilizing fiber tip reflection was proposed in 1987 (Farahi et al., 1987). The following year, Butler and Ginley published a more comprehensive investigation of the previously proposed interferometric sensor (Butler e Ginley, 1988). In their approach, two different optical fibers were exposed to hydrogen gas—one bare and the other coated with palladium (Pd). The resulting beams were then combined to form an interference fringe, whose position was measured as a function of gas concentration.

Several cavity-based interferometric structures have also been explored. For instance, a Fabry-Pérot cavity sensor was developed using a gap between a single-mode fiber (SMF) and a multi-mode fiber (MMF), with a Pd coating applied over a glass casing (Zeakes et al., 1994). Another variation employed a Fabry-Pérot cavity between two SMF sections (Yang et al., 2010).

Additionally, Mach-Zehnder interferometer (MZI)-based sensors have been implemented using Pd/Au nanowires in contact with the signal arm (Gu et al., 2015). A Sagnac interferometer-based device has also been proposed, incorporating a Pt-loaded WO_2/SiO_2 structure on a panda-type polarization-maintaining fiber (PMF).

The principle of coating optical fibers with expanding materials that induce strain under hydrogen exposure has also been applied to Fiber Bragg Gratings (FBG). This approach enables variations in the grating structure to change in response to gas concentration (Sutapun, 1999). Additionally, sensors based on Long Period Gratings (LPG) have been proposed (Trouillet et al., 2006).

Double-FBG structures have been investigated, where only one FBG region is metallized (Silva et al., 2013), as well as Pd-coated tapered structures (Yu et al., 2015). Tilted FBGs have also been explored for H_2 sensing, incorporating an Au/Pd bilayer coating on the grating region (Zhang et al., 2022a). Furthermore, polydimethylsiloxane (PDMS)/WO_3 coatings have been investigated for similar applications (Zhang et al., 2022b).

Hydrogen sensors have also been developed based on the exploitation of the Surface Plasmon Resonance (SPR) effect. Early investigations explored plasmonic coupling in the Kretschmann configuration using palladium (Pd) thin films (Chadwick e Gal, 1993). $Au/SiO_2/Pd$ structures were experimentally investigated with complete removal of the cladding of the fiber (Perrotton et al., 2013).

Fiber-based devices have been computationally analyzed, particularly polished D-type structures incorporating a Metal-Insulator-Metal (MIM) waveguide (Perrotton et al., 2011; Tabassum e Gupta, 2015). Metallized fiber tip sensors have also been investigated, initially focusing on Pd films deposited on the tip of a multi-mode

fiber (MMF) (Butler, 1991; Bévenot et al., 2000).

Additionally, various devices based on D-shaped fibers have been proposed, including Pd-infused porous TiO_2 structures (Poole et al., 2016) and Pd/Au nanocones fabricated on the polished region (Cao et al., 2020).

Chapter 3

Harmonic Minimization Method for Plasmonic Diffraction Grating Sensor Design

The design of diffraction gratings is a critical challenge in numerous fields of applied optics, including integrated optics, spectroscopy, and plasmonics. This work introduces a novel strategy for optimizing the design of diffraction-based plasmonic sensors. The proposed Harmonic Minimization Method bridges low-complexity diffraction formalisms with structures that are more feasible for fabrication using widely adopted manufacturing processes. This method is applied to the design of palladium (Pd) gratings for hydrogen gas sensing within the infrared spectrum. The performance of the designed structure is evaluated by comparing its reflectance spectrum and sensitivity to those of a fabricated device. It is shown that the proposed algorithm can obtain structures with similar sensitivity of those obtained by the Chandezon (C) method with low computational complexity for rectangular and triangular profiles. This chapter will introduce fundamental aspects of diffraction theory, the Harmonic Minimization Method (HMM), comparison between structures designed by HMM and the C method and the fabrication of HMM designed devices.

3.1 Fundamentals of Diffraction Theory

3.1.1 Kirchhoff Integral Theorem

There are at least two major theories for describing diffraction phenomena. The first to be mentioned is the Kirchhoff theory, which can be employed to explain experimental observations with precision. Later on, the Sommerfield theory of diffraction is proposed in order to correct inconsistencies within the Kirchhoff model.

Kirchhoff's description of diffraction is based on a theorem where the solution of the homogeneous wave equation in an arbitrary point in space is obtained in terms of values of the solution and its derivative in an arbitrary closed surface that contains this point, as shown in Fig. 3.1, with P_0 and S being the observation point and S the surface that contains P_0.

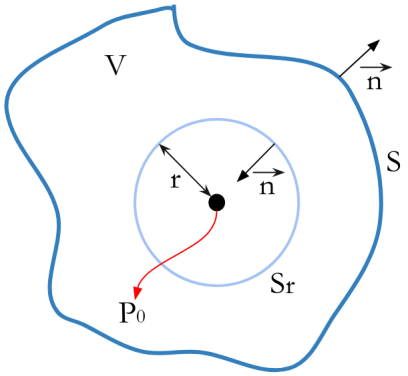

Figure 3.1: Graphical description for Kirchhoff integral theorem.

Considering a general solution $U(x)$ that satisfies a set of boundary values of a non-homogeneous linear differential equation of the form

$$a_2(x)\frac{\partial^2 U}{\partial x^2} + a_1(x)\frac{\partial U}{\partial x} + a_0(x)U = V(X) \tag{3.1}$$

we can write it as

$$U(x) = \int G(x - x')V(x')dx' \tag{3.2}$$

with $G(x)$ being the Green's function of the problem. Considering Eq. 3.2 is a convolution type integral in which the green's function is the system response to

the stimulus $\delta(x - x')$. So considering the situation in Fig. 3.1 we state that the Green function of the free space for delta-type perturbation is a unitary amplitude spherical wave of the form

$$G(r_p) = \frac{exp(jkr_p)}{r_p} \tag{3.3}$$

with r_p being the magnitude of the vector $\vec{r_p}$ pointing from P_0 to an observation point P. This consideration is important since the choice of a Green function is what separates the Kirchhoff and Sommerfeld theories, furthermore, alternative choices for this function are discussed.

To solve the problem in Fig. 3.1 one can apply the Green theorem by the use of an auxiliary surface to exclude the point P_0 where the value of $G(r_p)$ is infinite from the integration volume. Thus,

$$S' = S + S_r \tag{3.4}$$

with S_r being a spherical surface of radius r centered in P_0.

Since Eq.3.3 is an expansive spherical wave, inside the volume V, the Helmholtz equation must be satisfied

$$(\nabla^2 + k^2)G = 0, \tag{3.5}$$

and the same must be ensured for the observed field,

$$(\nabla^2 + k^2)U = 0. \tag{3.6}$$

Applying Green's theorem

$$\iiint_V (U\nabla^2 G - G\nabla^2 U)dV = \iint_V (U\frac{\partial G}{\partial n} - G\frac{\partial U}{\partial n})dS, \tag{3.7}$$

with $\partial/\partial n$ representing the derivative on the normal direction of the surface. Employing Eqs. 3.5 and 3.6 on the left side of Eq. 3.7,

$$\iiint_V (U\nabla^2 G - G\nabla^2 U)dV = -\iiint_V (UGk^2 - GUk^2)dV = 0, \tag{3.8}$$

and the theorem is reduced to

$$\iint_{S'} (U\frac{\partial G}{\partial n} - G\frac{\partial U}{\partial n})dS = 0, \tag{3.9}$$

$$\iint_S (U\frac{\partial G}{\partial n} - G\frac{\partial U}{\partial n})dS - \iint_{S_r} (U\frac{\partial G}{\partial n} - G\frac{\partial U}{\partial n})dS = 0 \tag{3.10}$$

.

Since, for an arbitrary point in S' the Green function is described by Eq.3.3, its normal derivative can be written as

$$\frac{\partial G(r_p)}{\partial n} = cos(\vec{n}, \vec{r_p})(jk - 1/r_p)\frac{exp(jkr_p)}{r_p} \tag{3.11}$$

with $cos(\vec{n}, \vec{r_p})$ being the cosine of the smaller angle between the mentioned vectors. For a particular case of a point P on S_r surface, $cos(\vec{n}, \vec{r}) = -1$. With these results Eqs. 3.3 and 3.11 become

$$G(r) = \frac{exp(jkr)}{r}, \tag{3.12}$$

$$\frac{\partial G(r)}{\partial n} = \frac{exp(jkr)}{r}(1/r - jk). \tag{3.13}$$

With the use of Eqs. 3.12 and 3.13 and considering the continuity of the observed field U and its derivatives, one can calculate the effect using Eq. 3.10 at the limit in which $r \to 0$. That means,

$$\lim_{r\to 0} \iint_{S_r} (U\frac{\partial G}{\partial n} - G\frac{\partial U}{\partial n})dS = 4\pi U(P). \tag{3.14}$$

With Eq. 3.14 in Eq. 3.10, one can write

$$U(P) = \frac{1}{4\pi} \cdot \iint_S \left[\frac{\partial U}{\partial n} \cdot \frac{exp(jkr_p)}{r_p} - U \cdot \frac{\partial}{\partial n} \left(\frac{exp(jkr_p)}{r_p} \right) \right] dS \tag{3.15}$$

which is known as the Kirchhoff integral theorem. This expression obtains the field for generic vector r_p pointing from the emission point P_0 to an observation point P inside of a closed surface S in terms of the field on the surface. Subsequently this result in employed on the description of the diffraction phenomena in order to obtain a scalar theory of diffraction.

3.1.2 Application of the Kirchhoff Integral Theorem to Diffraction Phenomena

Considering the situation in Fig. 3.2, in which a beam of light is diffracted by a slit. To find the field of point P one must apply the Kirchhoff integral theorem and choose an integration surface that conveniently allows the calculation. With surfaces S_1 and S_2 shown in Fig 3.2, Eq. 3.15 becomes

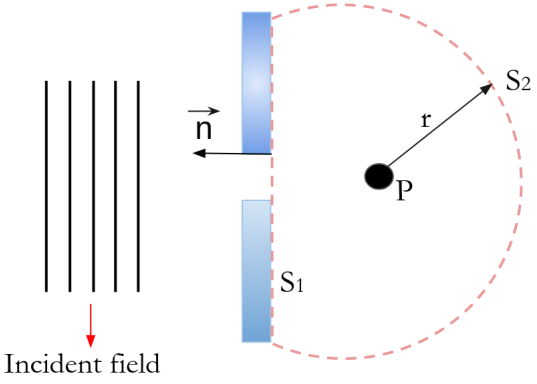

Figure 3.2: Source and observation point for diffraction over a slit.

$$U(P) = \frac{1}{4\pi} \cdot \iint_{S_1+S_2} (G\frac{\partial U}{\partial n} - U\frac{\partial G}{\partial n})dS. \tag{3.16}$$

Dealing initially with surface S_2, one must note that with the increase in r this surface is approximated by an spherical surface, from Eq. 3.11

$$\lim_{r\to\infty} \frac{\partial G}{\partial n} = (jk - 1/r)\frac{exp(jkr)}{r} = jkG. \tag{3.17}$$

The integral concerning S_2 in Eq. 3.16 becomes

$$\iint_{S_2}[G\frac{\partial U}{\partial n} - U(jkG)] = \int_{\Omega} G(\frac{\partial U}{\partial n} - jkU)r^2 d\omega, \tag{3.18}$$

with Ω being the solid angle referent to S_2 from P. It is important to notice that this integral must vanish to ensure that the field U decays as fast as the divergent spherical wave. For that, the following relation must hold

$$\lim_{r\to\infty}(\frac{\partial U}{\partial n} - jkU)r = 0, \tag{3.19}$$

which is known as the Sommerfeld radiation condition. This is a guarantee that there is only an outgoing wave in S_2 and there is no ingoing wave, which could result in a not null integral over this surface for $r \to \infty$.

For the S_1 surface, one should consider that the slit is made of an opaque material so the integration occurs over a surface Σ that concerns the orifice. To proceed with the model, Kirchhoff adopts two boundary conditions: On the surface Σ, the field U and $\partial U/\partial n$ are exactly the same as they would be in the absence of the slit; $U = \partial U/\partial n = 0$ on the part of the surface S_1 that does not coincide with Σ. The first condition permits specifying conveniently the field on Σ and the second allows to neglect of the part of the surface that does not coincide with the orifice. Eq. 3.16 then becomes,

$$U(P) = \frac{1}{4\pi} \cdot \iint_{\Sigma}(G\frac{\partial U}{\partial n} - U\frac{\partial G}{\partial n})dS. \tag{3.20}$$

On the approximation of the distance between the orifice and the observation point is much bigger than the wavelength, one can rewrite Eq. 3.11 as

$$\frac{\partial G(r)}{\partial n} = jk \cdot cos(\vec{n}, \vec{r})\frac{exp(jkr)}{r} \tag{3.21}$$

With Eq. 3.3 and 3.21 on Eq. 3.20, one obtains

$$U(P) = \frac{1}{4\pi} \cdot \iint_{\Sigma} \frac{exp(jkr)}{r} \left[\frac{\partial U}{\partial n} - jkUcos(\vec{n}, \vec{r}) \right] dS. \tag{3.22}$$

Considering that in the scheme of Fig. 3.3 the slit is illuminated by one single spherical wave,

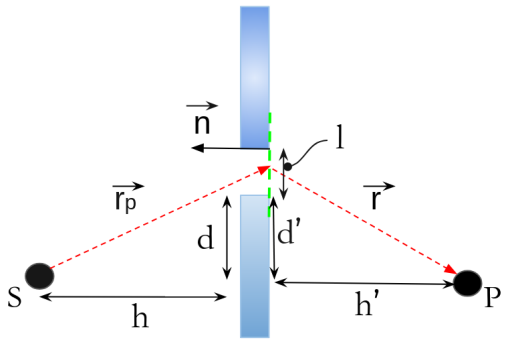

Figure 3.3: Source and observation point for diffraction over a slit.

$$U(P_0) = \frac{Aexp(jkr_p)}{r_p}, \tag{3.23}$$

one obtains

$$U(P) = \frac{A}{j\lambda} \iint_{\Sigma} \frac{exp[jk(r + r_p)]}{rr_p} \cdot \left[\frac{cos(\vec{n}, \vec{r}) - cos(\vec{n}, \vec{r_p})}{2} \right] dS. \tag{3.24}$$

The Eq. 3.24 is known as the Fresnel-Kirchhoff formula. Is important to notice the reciprocal nature of this model. If, under the same conditions, the point of emission becomes the point of observation and vice versa, the diffracted field would have the same distribution.

It is also clear that this model was built upon the supposition that the illumination consists of one single expanding spherical wave. A few limitations and inconsistencies of the Kirchhoff model are corrected in the Sommerfeld approach to diffraction. One particular problem is the adopted boundary conditions for the field and its normal derivative, which leads to the field vanishing on the whole volume of integration. This is problematic because it does not make physical sense, but can be corrected by alternative choice of Green functions that permit the construction of a theory without the previously considered boundary condition. Since the Kirch-

hoff theory provides an accurate description of diffraction phenomena a thorough description of Sommerfeld's theory is out of the scope of this work but is extensively discussed in the literature(Goodman,1969).

3.1.3 Fraunhofer Approximation and the Diffraction Grating Equation

While dealing with the mathematical description of diffraction phenomena there are two situations that can be considered to simplify the model by approximations. Fig. 3.4 shows a qualitative scheme for the Fraunhofer and the Fresnel approximations.

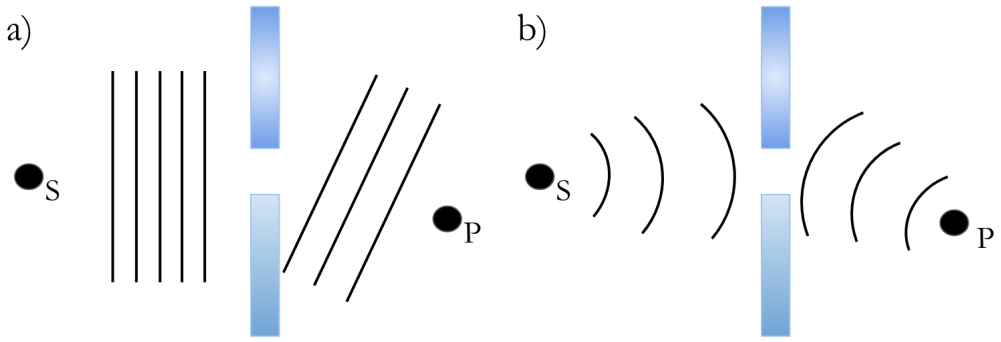

Figure 3.4: Approaches to Diffraction. a) Fraunhofer approximation and b) Fresnel approximation.

In the case of Fraunhofer approximation, the emission point is distant enough of the slit so the wavefront curvature can be neglected and the same can be stated about the distance between the slit and the observation point. For the Fresnel approximation, the curvature of the wavefront should be taken into account to provide accurate descriptions. Considering the situation in Fig. 3.4, one can define a quantitative separation between the two approximations.

Considering the geometry and variables in Fig. 3.3, one can calculate the variation of the optical path $\Delta(r + r_p)$,

$$\begin{aligned}\Delta(r+r_p) = &\sqrt{d^2+(h+l)^2}+\sqrt{d'^2+(h'+l)^2}\\ &-\sqrt{d^2+h^2}-\sqrt{d'^2+h'^2}\\ &=(\frac{h}{d}+\frac{h'}{d'})l+\frac{1}{2}(\frac{1}{d}+\frac{1}{d'})l^2+...\end{aligned} \tag{3.25}$$

The quadratic term in Eq. 3.25 is where the information about the wavefront of the beam is, so to ensure the fields can be described as plane waves, the following condition needs to be satisfied,

$$\frac{1}{2}(\frac{1}{d}+\frac{1}{d'})l^2 << \lambda. \tag{3.26}$$

which is known as the Fraunhofer diffraction criteria. Following this, a few considerations can be made about the application of the Fresnel-Kirchhoff formula to Fraunhofer diffraction. For example, considering a small enough beam divergence one can assume that the term $cos(\vec{n},\vec{r})-cos(\vec{n},\vec{r_p})$ is invariant in the surface of integration. The term $exp(jkr_p)/r_p$ can be considered constant since we are dealing with an optical source fixed in space, and the term $exp(jkr)/r$ is dominated by the exponential and the mean value of $1/r$ can be used. With such assumptions, Eq. 3.24 becomes

$$\begin{aligned}U(p) = \frac{A}{j\lambda}\cdot\frac{exp(jkr_p)}{r_p}\cdot\frac{cos(\vec{n},\vec{r})-cos(\vec{n},\vec{r_p})}{2}\\ \iint_\Sigma \exp(jkr)\,dS.\end{aligned} \tag{3.27}$$

One particular situation of great importance to this work, is the case of multiple slits, structures known as a diffraction grating and exposed schematically in Fig. 3.5.

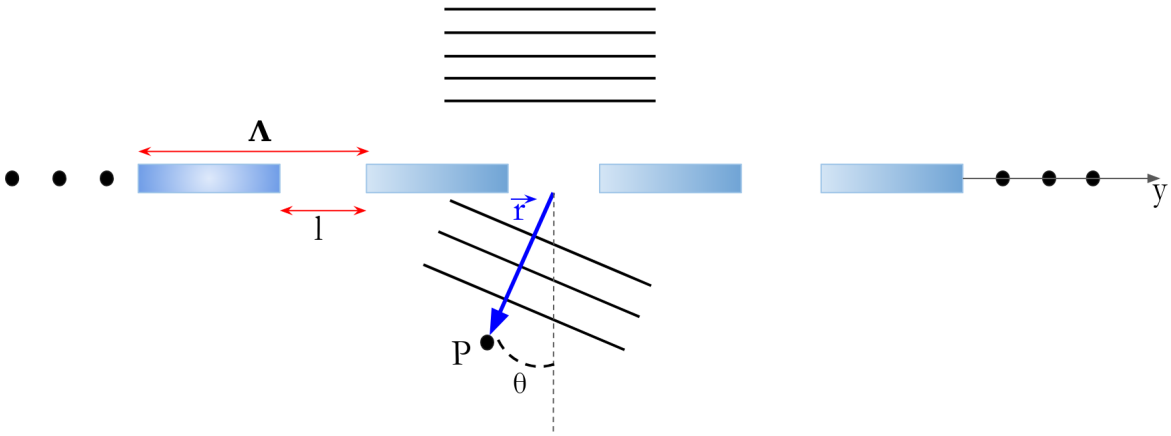

Figure 3.5: Diffraction over multiple slits, diffraction grating..

In this case, the integral in Eq. 3.27 becomes

$$\iint_{\Sigma} exp[jkysen(\theta)] = \int_0^l + \int_{\Lambda}^{\Lambda+l} + ... + \int_{(N-1)/\Lambda}^{(N-1)/\Lambda+l} exp[jkysen(\theta)]dy \tag{3.28}$$

$$= \frac{exp[jklsen(\theta)] - 1}{jksen(\theta)}[1 + exp[jk\Lambda sen(\theta)] + ... + exp[jk(N-1)\Lambda sen(\theta)] \tag{3.29}$$

$$= \frac{exp[jklsen(\theta)] - 1}{jksen(\theta)} \cdot \frac{1 - exp[jk\Lambda N sen(\theta)]}{1 - exp[jk\Lambda sen(\theta)]} \tag{3.30}$$

$$= l \cdot exp[\beta + (N-1)\gamma] \cdot \frac{sen(\beta)}{\beta} \cdot \frac{sen(N\gamma)}{sen(\gamma)} \tag{3.31}$$

with $\beta = \frac{1}{2}klsen(\theta)$ and $\gamma = \frac{1}{2}k\Lambda sen(\theta)$.

From Eq. 3.31, one can write for the diffracted field intensity profile

$$I = I_0 \left[\frac{sen(\beta)}{\beta}\right]^2 \left[\frac{sen(N\gamma)}{Nsen(\gamma)}\right]^2. \tag{3.32}$$

It is possible to note from Eq. 3.32 that the maximum occurs for $\gamma = n\pi$, that means

$$n\lambda = \Lambda sen(\theta), \tag{3.33}$$

which is known as the diffraction grating equation.

3.2 Rayleigh and C method based optimization strategies

3.2.1 Rayleigh and Chandezon (C) methods description

In the literature, many methods have been proposed to calculate the reflectance of diffraction grating structures. As previously mentioned, the first proposed method to describe the optical response was proposed by Rayleigh, in this case, it is assumed that under plane-wave illumination, the transmitted and reflected fields are described as a sum of plane waves, each one with a particular transmission or reflection coefficient. For the physical situation shown in Fig. 3.6, one can write (de Araujo et al.,2023)

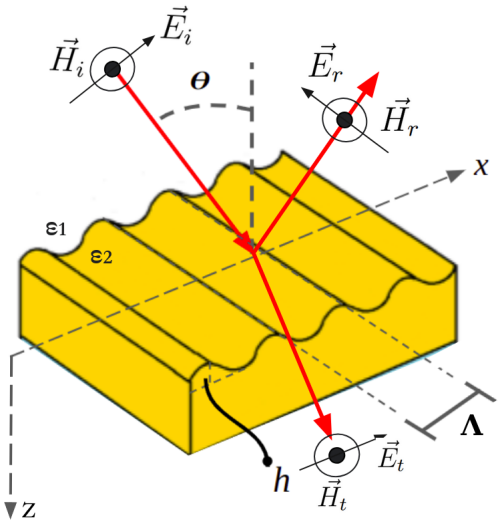

Figure 3.6: Incident, transmitted and reflected fields in a diffraction grating.

$$\vec{H}_1 = \vec{H}_i + \vec{H}_r, \tag{3.34}$$

and

$$\vec{E}_1 = \vec{E}_i + \vec{E}_r, \tag{3.35}$$

for the total magnetic and electric fields in medium 1. With

$$\vec{H}_i = (0,1,0)e^{-j(k_x x + k_z z)}, \tag{3.36}$$

$$\vec{H}_r = (0,1,0) \sum_{l=-\infty}^{l=\infty} r(l) e^{-j(k_l x - k_z^o z)}, \tag{3.37}$$

$$\vec{E}_i = \frac{\omega \mu_0}{k_0^2 \epsilon_1}(k_z, 0, -k_x)e^{-j(k_x x + k_z z)}, \tag{3.38}$$

$$\vec{E}_r = \frac{\omega \mu_0}{k_0^2 \epsilon_1} \sum_{l=-\infty}^{l=\infty} r(l)(-k_z^o, 0, -k_l)e^{-j(k_l x - k_z^o z)}, \tag{3.39}$$

and for the wave vectors

$$k_z = \sqrt{\epsilon_1 k_0^2 - k_x^2}, \tag{3.40}$$

$$k_z^o = \sqrt{\epsilon_1 k_0^2 - k_l^2}, \tag{3.41}$$

where superscript o representing the wave vector over the grating and k_n being determined by the diffraction grating equation (Loewen e Popov,2018)

$$k_n = k_x + n\frac{2\pi}{\Lambda}. \tag{3.42}$$

The field in medium 2, which is the metal grating, is transmitted only. Therefore, one can write

$$\vec{H}_t = (0,1,0)\sum_{l=-\infty}^{l=\infty} t(l)e^{-j(k_l x + k_z^u z)}, \tag{3.43}$$

$$\vec{E}_t = \frac{\omega\mu_0}{k_0^2\epsilon_2}\sum_{l=-\infty}^{l=\infty} t(l)(k_z^u, 0, -k_l)e^{-j(k_l x + k_z^u z)}, \tag{3.44}$$

with

$$k_z^u = \sqrt{\epsilon_2 k_0^2 - k_l^2}, \tag{3.45}$$

where superscript u representing the wavevector under the grating surface. In these equations, $r(l)$ and $t(l)$ are the reflection and transmission coefficients, which are needed to calculate reflectance and transmittance of the grating. For that, the boundary conditions for tangential fields are employed to obtain a two equation linear system

$$H_{1t}(x,z) = H_{2t}(x,z)|_{z=s(x)}, \tag{3.46}$$

$$E_{1t}(x,z) = E_{2t}(x,z)|_{z=s(x)}, \tag{3.47}$$

with the underscript t representing the tangential component of the vectors, and $s(x)$ being the function that describes the grating profile, in this case, $s(x) = h_s \cdot sin(2k_g x)$, in which $k_g = 2\pi/\Lambda$. To directly employ fields described by Eqs. 3.34 and 3.35 into the conditions 3.46 and 3.47 is to neglect the field concentration in the valleys of the grating. That assumption is the Rayleigh hypothesis, and that is why it works only for sufficiently shallow structures. For convenience of description, the plane waves are expanded into first kind Bessel functions

$$e^{-j\beta h \sin(k_g x)} = \sum_{a=-\infty}^{a=\infty} J_n(\beta h)e^{(-jak_g x)}, \tag{3.48}$$

with a being the order of the Bessel function. Then applying the previously mentioned boundary conditions, one can write

$$J_m(k_z h) = \sum_{l=-\infty}^{l=\infty} \left(t(k_l) J_{m-l}(k_z^u h) - r(k_l) J_{m-l}(-k_z^o h)\right), \tag{3.49}$$

$$\left(\frac{m k_g k_x - k_z^2}{\epsilon_1 k_z}\right) J_m(k_z h) = \sum_{l=-\infty}^{l=\infty} \left(\left(\frac{(m-l) k_g k_n - (k_z^u)^2}{\epsilon_2 k_z^u} \right) t(k_l) J_{m-l}(k_z^u h) - \left(\frac{(m-l) k_g k_n - (k_z^o)^2}{\epsilon_1 k_z^o} \right) r(k_l) J_{m-l}(-k_z^o h) \right). \tag{3.50}$$

To solve the linear systems formed by Eqs. 3.49 and 3.50 it is mandatory that the indices l and m are truncated to a maximum value V, then a $2(2V+1) \times 2(2V+1)$ system can be solved. In this work the truncated system is solved with a truncation value V = 4, leading to a 18 x 18 system to be solved for each iteration step.

In the Chandezon model(Chandezon et al.,1980), the fields are represented as plane wave expansions, similar to the Rayleigh method, but within a curvilinear coordinate system in which the profile of the interface between the media becomes a flat surface. This method yields superior results for gratings with arbitrary profiles compared to the Rayleigh method and provides accurate descriptions even for rectangular profiles. That means employing the following variable change

$$z' = z - s(x) \tag{3.51}$$

in fields 3.34 and 3.35 with boundary conditions 3.46 and 3.47. In this new coordinate system, an analogous mathematical procedure can be executed to obtain a truncated linear system in which the reflection and transmitted coefficients will be determined.

3.2.2 Optimization Strategy for Diffraction Grating Sensor Design

The structures obtained using the Rayleigh and the C method approach are all optimized following the same strategy. Since it is expected that higher sensitivities are observed in specular reflection governed by the coefficient $r(k_0)$, the objective function to be maximized is the sensitivity defined by the derivative of the specular reflectance function relative to the refractive index of the sensing medium, that is

$$S = \frac{d(|r(k_0)|^2)}{dn_1}. \tag{3.52}$$

Since reasonable initial guesses for grating amplitude and periodicity can be obtained, a gradient descendant optimization routine is employed. For plasmonic coupling the amplitude is typically in the order of tens of nanometers, so an initial guess $h_o = 10$ nm is used. For a good estimate of the grating periodicity for a particular order of diffraction, the diffraction grating equation should be used (Loewen e Popov,2018)

$$k_l = k_x + l\frac{2\pi}{\Lambda}, \tag{3.53}$$

and since the surface plasmon propagates with a wave vector

$$k_{sp} = k'_{sp} + jk''_{sp}, \tag{3.54}$$

with (Fontana,2004)

$$k'_{sp} = k_0\sqrt{\frac{\epsilon'\epsilon_1}{\epsilon' + \epsilon_1}}, \tag{3.55}$$

$$k''_{sp} = k'_{sp}\frac{\epsilon''\epsilon_1}{2\epsilon'\left(\epsilon' + \epsilon_1\right)}, \tag{3.56}$$

one can obtain, considering normal incidence on the grating and satisfying the condition of coupling $k_l = k_{sp}$, the following expression for the grating periodicity initial guess is used

$$\Lambda \approx \pm l\lambda \left(\frac{\epsilon' n_1^2}{\epsilon' + n_1^2} \right)^{-1/2}. \tag{3.57}$$

3.3 Geometrical Considerations of Diffraction Integral and the Harmonic Minimization Method

From this description we can assure that for a fixed point of observation the field depends on the surface of integration. That means if a new geometry for the surface is considered, the new field will resemble the previous one if the new surface resembles the previous one, independent on its geometry. It is based on this perception that the HMM is developed, that means if a particular refracted fields spectrum is calculated for a sinusoidal surface for example, we can obtain similar field distribution for a generic profile function if we can adjust the new profile to the sinusoidal one.

The HMM is not a procedure for describing the optical response of gratings, nor is it an optimization method. Instead, it is a profile translation algorithm. Its purpose is to be used in conjunction with an optimization algorithm based on the Rayleigh method, selected for its low computational complexity. After an optimized sinusoidal grating is obtained, the HMM algorithm determines the structural parameters of a generic profile grating, in this work considered to be rectangular, to approximate the sinusoidal profile as closely as possible. This algorithm considers only the geometric characteristics of the structure and does not rely on a description of the grating's reflectance or its sensitivity curve, that means no electromagnetic calculation is conducted throughout its execution, in favor of smaller computational complexity. The sinusoidal grating parameters are defined by:

$$G_s \equiv [\Lambda_s, h_s], \tag{3.58}$$

with the following profile function,

$$s(x) = h_s \cdot sen\left(\frac{2\pi x}{\Lambda_s}\right), \tag{3.59}$$

and we wish to obtain a grating with rectangular profile,

$$G_r \equiv [\Lambda_r, h_r], \tag{3.60}$$

with a profile function described by the Fourier series of a square wave

$$g(x) = h_r \cdot \frac{4}{\pi} \sum_{i=1}^{m} sen\left[\frac{2\pi(2n-1)x}{\Lambda_r}\right] \frac{1}{(2n-1)}. \tag{3.61}$$

The strategy involves minimizing the quadratic error between $s(x)$ and $g(x)$ by adjusting the structural parameters Λ_r and h_r to ensure $g(x)$ closely resembles the model. A first-harmonic approximation is used as an initial guess for the minimization algorithm, resulting in a grating of the type:

$$G_{1\check{r}H} \equiv \left[\Lambda_s, \frac{\pi}{4} \cdot h_s\right]. \tag{3.62}$$

Algorithm 1 shows the procedure based on Rayleigh optimization and profile translation using the MMH method. In this algorithm, x represents the linear vector of abscissas defined from 0 to $6\Lambda_s$ with α samples. The algorithm performs multiple minimizations depending on the user-defined parameter $m_{\max}$, producing a pair of structural parameters for each harmonic. The procedure begins with the manual input of parameters by the user, including θ (the angle of incidence of the light beam on the grating), the real and imaginary parts of the dielectric function (ϵ' and ϵ''), the diffraction mode l, the wavelength of incidence λ_i, and the refractive index of the sensed medium n_s. Subsequently, the necessary assignments are made, and the nonlinear regression procedure is executed $m_{\max}$ times, generating a results document for each iteration.

This strategy allows the designer to obtain an optimized design using a computationally efficient method and then, during the manufacturing stage, the sinusoidal

Algorithm 1 Pseudocode for design optimization of plasmonic diffraction grating with HMM.

input $\theta, \epsilon', \epsilon'', l, \lambda_i, n_s$

$h_0 \leftarrow 10$ nm
$\Lambda_0 \leftarrow$ Eq. (23)
$h_s, \Lambda_s \leftarrow$ RayleighOptimization; (Conducts optimization on structural parameters to maximize sensitivity based on a Rayleigh description)
$\alpha \leftarrow 2000$;
$x \leftarrow$ LinearVec[0,6Λ_s,α]; (Creates a linear vector from 0 to 6Λ_s with α points)
$g(x) \leftarrow$ Eq. (31);
$model \leftarrow$ Eq. (29);
$InitialGuess \leftarrow$ Eq. (32);
$m \leftarrow 1$; (Sets number of harmonics equal to 1)
while $m \neq m_{max}$ **do**
    $h_r, \Lambda_r \leftarrow$ NonLinearRegression$(g(x), model, InitialGuess, m)$;
    Generates document with h_r and Λ_r for each harmonic;
    $m \leftarrow m + 1$
end while
Generate plots

grating design can be translated into the most suitable profile based on the available manufacturing method. Also, multiple gratings with different profiles can be generated and its sensitivity computationally studied before fabrication in order to decide which one is more suited to the particular application.

It is important to mention that the applicability of the optimization strategy suggested in this work is the same as the Rayleigh method, that is the ratio of the sinusoidal grating amplitude to its periodicity has to be below 0.142521. For the application in plasmonic gratings, this limit of applicability does not impose any impracticalities since the observation of the SPR in gratings occurs with amplitudes of the order of tens of nanometers while the periodicity is at least of the order of the incident wavelength. Considering that better sensitivities are generally observed in the infrared, this condition is always satisfied.

Another important consideration about the HMM and the associated optimization strategy is how it can handle fabrication constraints such as minimum feature sizes for etching and lithography processes. The limits of the etching procedures could be implemented in our strategy as constraints to reduce the algorithm search

space, but considering the typical values of the grating amplitude are of the order of tens of nanometers, the optimal values usually do not represent a fabrication challenge. Our strategy can handle the lithography limitations by choosing the appropriate order of diffraction. From Equation 3.58 one can state that the order of diffraction can heavily affect the periodicity of the optimal design. So, in a practical situation, the fundamental mode of diffraction is preferred since it leads to higher sensitivities, but depending on material and incident wavelength the optimal periodicity can be under the minimum feature size for a particular lithography procedure to be employed. In that case, a new design can be made to optimize a device for the second order of diffraction, and the optimal periodicity would be around twice the previously obtained and likely to be above the minimum feature size. The trade-off faced in this situation is that employing higher orders of diffraction would diminish the sensitivity of the device compared to the fundamental mode, but harmonic detection systems could still be employed in an experimental implementation to obtain good sensitivities.

3.4 Algorithm results, convergence and computation time

The algorithm described was implemented in the Julia programming language (Project,2025) due to its suitability for scientific computation and typically fast execution times. This work was carried out using version 1.11.2 of the aforementioned language on a personal computer equipped with an Intel® Core™ i7-1065G7 processor and 8 GB of RAM. The initial investigation focused on the convergence of the structural parameters of the grating obtained through the algorithm. Specifically, the variations in amplitude and periodicity as a function of the number of harmonics were analyzed for a particular set of input parameters in the optimization process. Fig. 3.7 presents the results up to 80 harmonics, demonstrating reasonable convergence of the amplitude parameter around 20 harmonics. The periodicity parameter

appears to converge more gradually; however, the difference between the values obtained for 20 and 80 harmonics is less than 3 nm. This slight variation does not result in a significant loss of sensitivity, as the sensitivity is not heavily dependent on the periodicity. Furthermore, the design can be tuned to resonate at the central wavelength of the laser used in the interrogation system, considering that the periodicity primarily influences the resonant wavelength. Based on these findings, the nominal values for the designed gratings were determined using the HMM with 20 harmonics. A detailed analysis of the spectra and its effect on sensitivity is provided in Section 3.5.

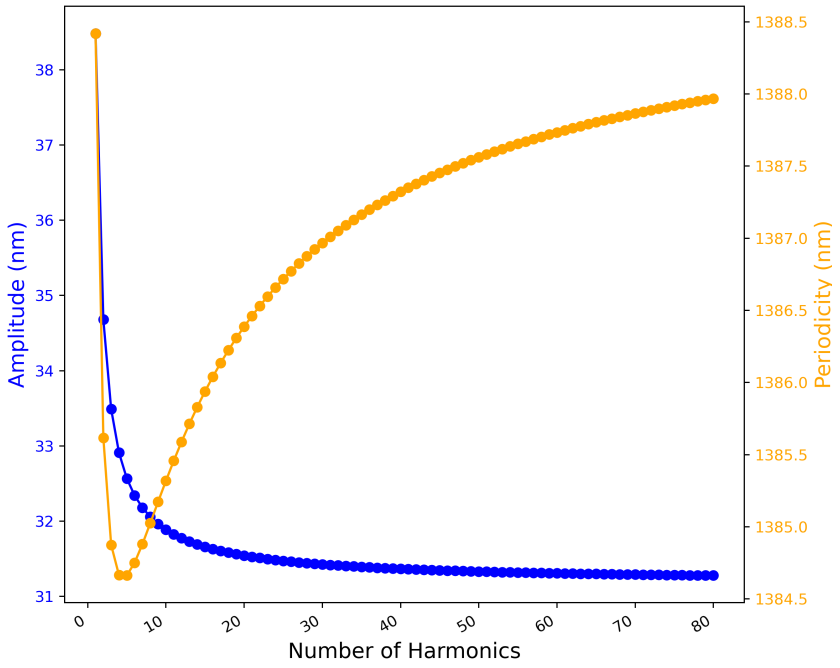

Figure 3.7: Convergence of structural parameters.

Another important metric supporting the usability of the design strategy proposed in this work is the computation time. For the HMM to be a reasonable alternative to the C method, it must not impose significant computational complexity compared to the Rayleigh-based optimization. This aspect was evaluated by running the algorithm 20 times using the same set of sinusoidal grating parameters. For each iteration, the total computation time and the percentage of this time

attributed exclusively to the compilation process were recorded. Fig. 3.8 presents the results for these metrics, showing an average computation time of 8.22 seconds, with 89.23% of this time, on average, associated with the compilation process.

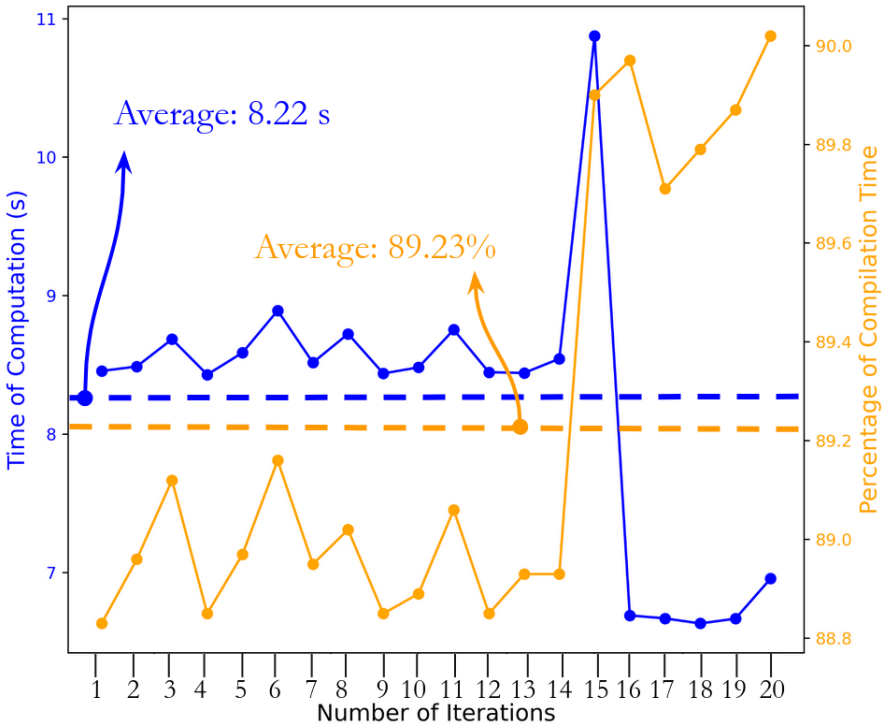

Figure 3.8: HMM computation time.

Following the investigations of convergence and computation time, ten structures were designed using the HMM for five different incident wavelengths in the infrared spectrum. These designs were generated under the first harmonic approximation and with twenty harmonics, allowing for comparison with a C method-based optimization strategy. All designs were conducted using the optical constants of palladium (Pd) obtained from an experimental database (Johnson e Christy,1972) and were developed in accordance with Algorithm 1. The results are shown in Table 3.1.

Table 3.1: Gratings obtained by C method and HMM strategies.

$\lambda_i(nm)$	$\Lambda(nm)$	$h(nm)$	m	Method
1392	1388.42	38.48	1	HMM
1392	1386.39	31.54	20	HMM
1392	1385.01	32.95	-	C
1531	1527.88	38.72	1	HMM
1531	1525.64	31.74	20	HMM
1531	1524.72	34.62	-	C
1568	1564.26	39.54	1	HMM
1568	1561.97	32.41	20	HMM
1568	1561.16	35.05	-	C
1571	1568.55	40.33	1	HMM
1571	1566.25	33.06	20	HMM
1571	1565.47	35.10	-	C
1654	1649.94	41.21	1	HMM
1654	1647.52	33.78	20	HMM
1654	1647.00	36.04	-	C

3.5 Spectral comparison between the C method and HMM obtained gratings

Based on the results presented in Table 3.1, it is important to compare the reflectance spectra of the designed structures and the corresponding sensitivity values. All reflectance spectra, $R(\lambda)$, were computed using the finite element method [11], implemented in the commercial tool COMSOL, to solve the electric field through continuity conditions at the interfaces. Fig. 3.9 shows the modeled structure.

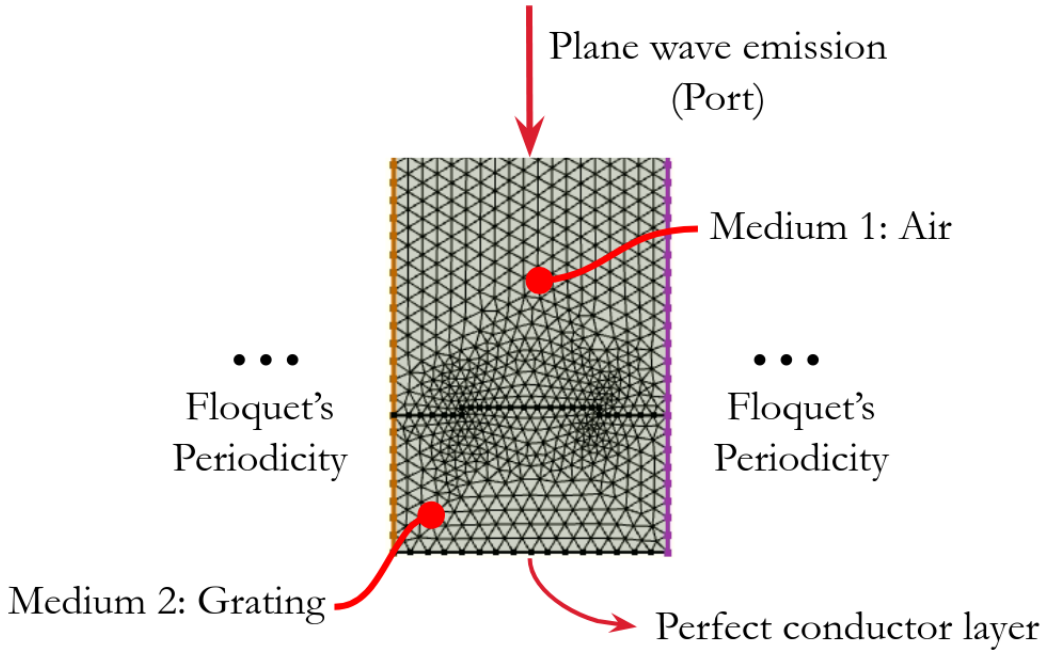

Figure 3.9: Geometry and mesh of the FEM model. The Figure indicates the port and the perfect electric conductor.

The fields are calculated with the use of the Electromagnetic Waves, Frequency Domain (*ewfd*) interface. This interface solves the time-harmonic wave equation for the electric field. Such interface is configured to solve the the harmonic wave equation for the in-plane electric field vector, employing a quadratic field discretization.

As a feature of the *ewfd* interface the Port is a platform that must be configured to emit the incident field. In this work it is configured an input power of $1W/m$ and the input quantity as the magnetic field $H_0 = (0, 0, -1)$ A/m. The feature of automatic diffraction order calculation is also employed with the sensing medium refractive index $n_s = 1$. It also used the Diffraction Order functionality to absorb orders ± 1 and ± 2, in order to take into consideration only the fundamental mode of diffraction.

The *Wave Equation* modules are configured for each medium in terms of its refractive indexes.

The computation used a triangular mesh with element sizes ranging from 295 nm to 0.59 nm. Beyond the ruled region, the metal has extra 90 nm thickness. The emission is modeled with $10\lambda_i$ distance of the grating surface, ensuring criteria 3.26 is satisfied. Additionally, the sensitivity was calculated and compared. Figs. 3.10

to 3.14 show the results.

The numerical results demonstrate that the first harmonic approximation provides resonance values reasonably close to the optimal ones. A minimization routine was subsequently employed to determine the parameters yielding the structure with optimal sensitivity. The analysis indicates no significant difference in the wavelength of maximum coupling between the C method-based optimization and the 20-harmonic HMM. Comparable sensitivity results were observed in all cases and the HMM produced marginally higher sensitivity values. Considering that there is only one optimal set of amplitude and periodicity parameters, the small difference between obtained sensitivities shows that the HMM and the C-method both converge to the same solution. This results demonstrate that our approach can obtain the optimal solution in short periods of time. This strategy could be employed to investigate the performance of unconventional grating profiles without conducting new electromagnetic calculations and possible adaptations to the previously cited algorithm to deal with new geometries.

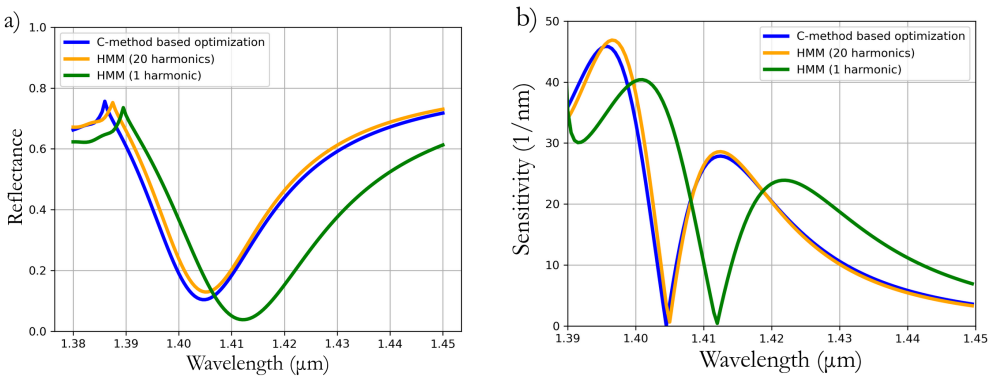

Figure 3.10: Grating spectral properties comparison for $\lambda_i = 1392$ nm. a) Reflectance for gratings according to Table 3.1. b) Calculated sensitivity curve.

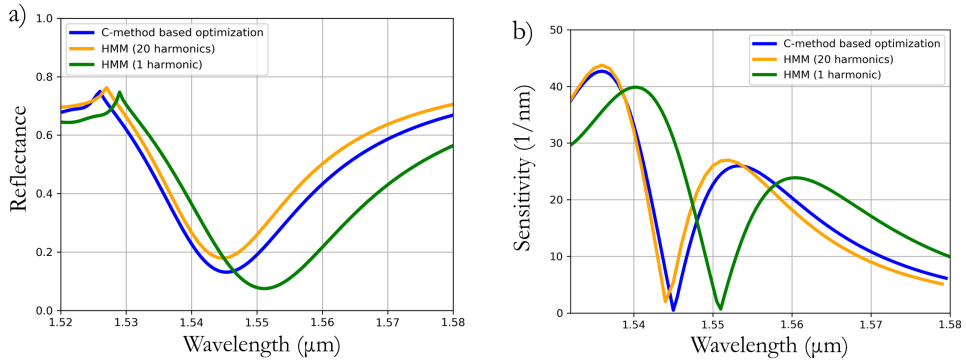

Figure 3.11: Grating spectral properties comparison for $\lambda_i = 1531$ nm. a) Reflectance for gratings according to Table 3.1. b) Calculated sensitivity curve.

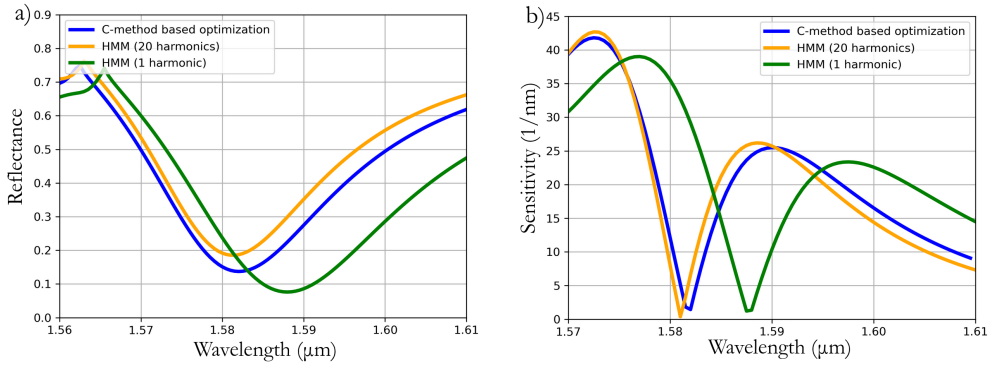

Figure 3.12: Grating spectral properties comparison for $\lambda_i = 1568$ nm. a) Reflectance for gratings according to Table 3.1. b) Calculated sensitivity curve.

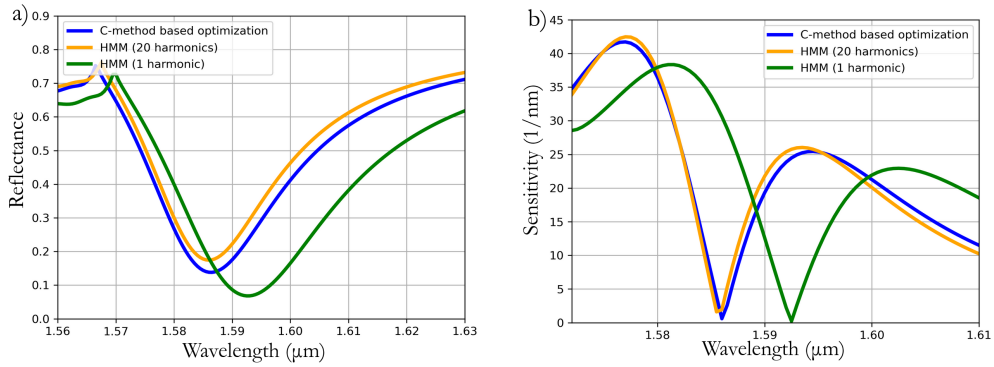

Figure 3.13: Grating spectral properties comparison for $\lambda_i = 1571$ nm. a) Reflectance for gratings according to Table 3.1. b) Calculated sensitivity curve.

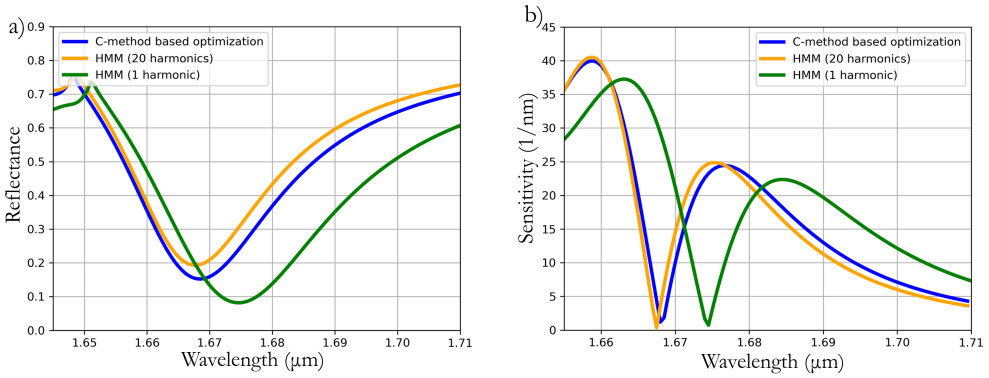

Figure 3.14: Grating spectral properties comparison for $\lambda_i = 1654$ nm. a) Reflectance for gratings according to Table 3.1. b) Calculated sensitivity curve.

3.5.1 Triangular diffraction grating design

Initially, the rectangular profile was investigated considering that it consists of two discontinuities and it was expected that a greater number of harmonics would be necessary to obtain convergence. Now, an alternative profile and material are investigated to provide practical results about the HMM applicability to different structures. The method is then conducted based on Nb as the metal, with optical constants obtained from Ref (Golovashkin et al.,1969a), $\lambda_i = 958$ nm, and the profile of the triangular grating being modeled by

$$t(x) = h_t \frac{8}{\pi^2} \sum_{i=1}^{m} \frac{(-1)^i}{(2i-1)^2} sin\left[\frac{2\pi(2i-1)x}{\Lambda_t}\right]. \tag{3.63}$$

Similarly as the results exposed in Fig 3.7, a convergence investigation was conducted with the same criteria of convergence being adopted. Table 3.2 shows the result.

According to the results in Table 3.2, the design can then be conducted with 4 harmonics. It is expected that such a profile would require less harmonics for convergence than the rectangular one since the triangular wave shape is more easily described by a sinusoidal model and Gibbs overshooting is not a concern compared to the sharp edges of the rectangular profile. It shows that the number of harmonics for convergence is dependent on the desired profile and for structures other than rectangular and triangular explored here, it is recommended to run a convergence

test before conducting new designs.

Table 3.2: Triangular Nb gratings designed by HMM.

m	$\Lambda_t(nm)$	$h_t(nm)$
1	951.78	29.61
2	952.45	29.24
3	952.31	29.19
4	952.36	29.18

3.6 Fabrication of HMM designed devices

3.6.1 Diffraction Grating Fabrication

In order to validate the proposed design method, one particular design was chosen for fabrication. Based on the nominal values for 20 harmonics and an incident wavelength of 1531 nm, as specified in Table 3.1, the device shown in Fig. 3.15 was considered for fabrication. The layout considers a squared $25mm^2$ chip with a squared $4mm^2$ grating area. For adhesion a 10 nm Ti layer is employed followed by the Pd grating itself. Fig. 3.16 shows a detail of the .gds file that is read by the lithography equipment.

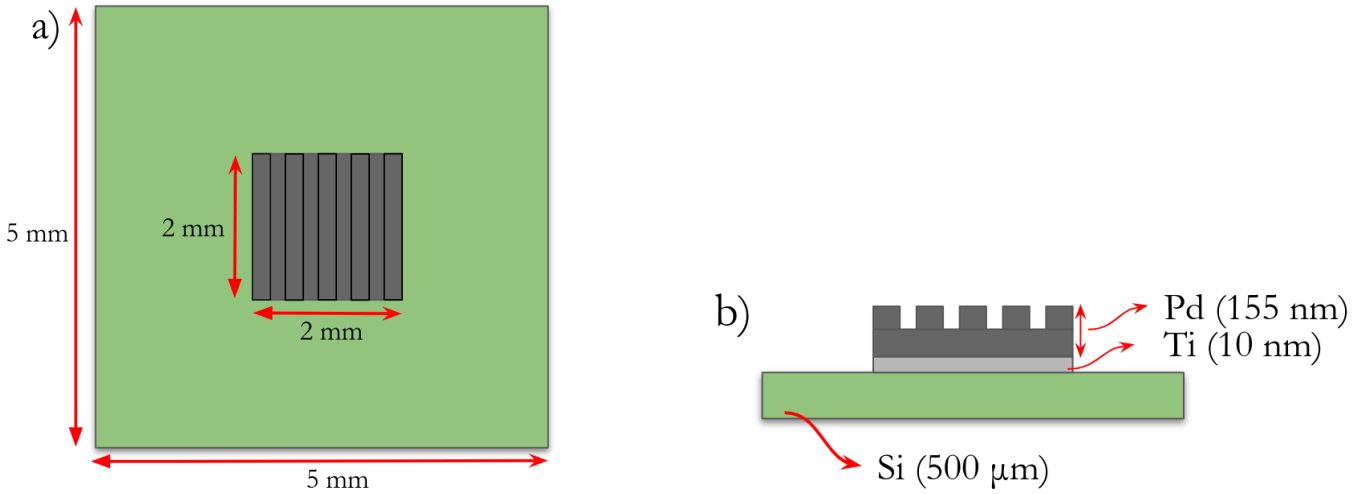

Figure 3.15: Dimensions of diffraction grating chip. a) Chip area and grating. b) Thickness of each layer of the structure.

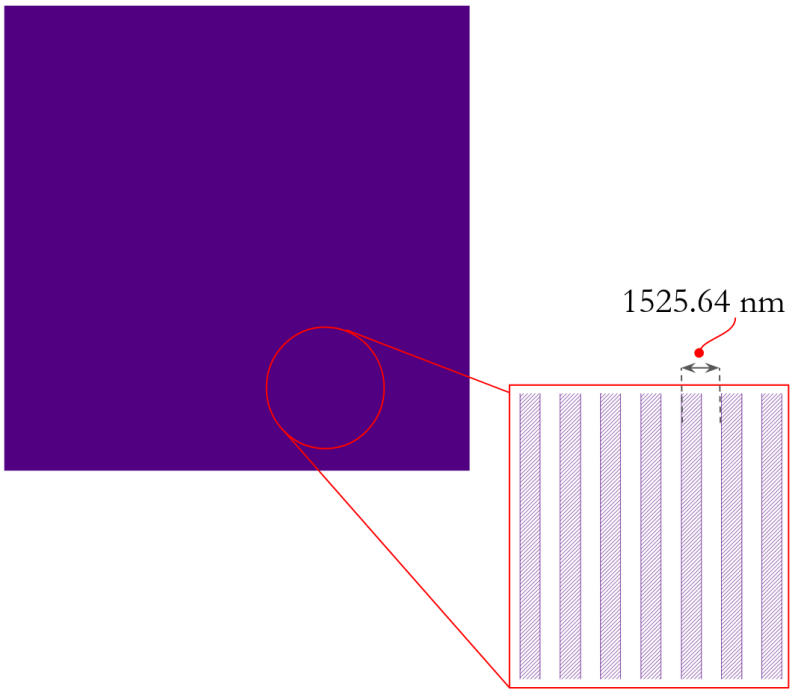

Figure 3.16: Details of the .gds file.

The fabrication process began with a 500 ± 50 μm Si substrate, onto which a 10 nm Ti film was evaporated, followed by the deposition of a 155 nm Pd film. This process was conducted with a Lesker PVD 200 evaporator. A temperature controlled resist coating was then conducted at 90 °C. The process continued with the optical lithography procedure with the use of a Heidelberg MLA 500 and the samples were exposed to an optical dose of 110 mJ/cm^2.

The process continued with reactive ion etching (RIE) of the Pd layer, performed at a pressure of 50 mTorr and an Ar flow rate of 50 standard cubic centimeter per minute. This process lasted for approximately 3 minutes. Following this step, the resist was removed, and the samples were inspected using an optical profilometer and a Scanning Electron Microscope (SEM). The Fig. 3.17 shows the batch of fabricated diffraction grating devices.

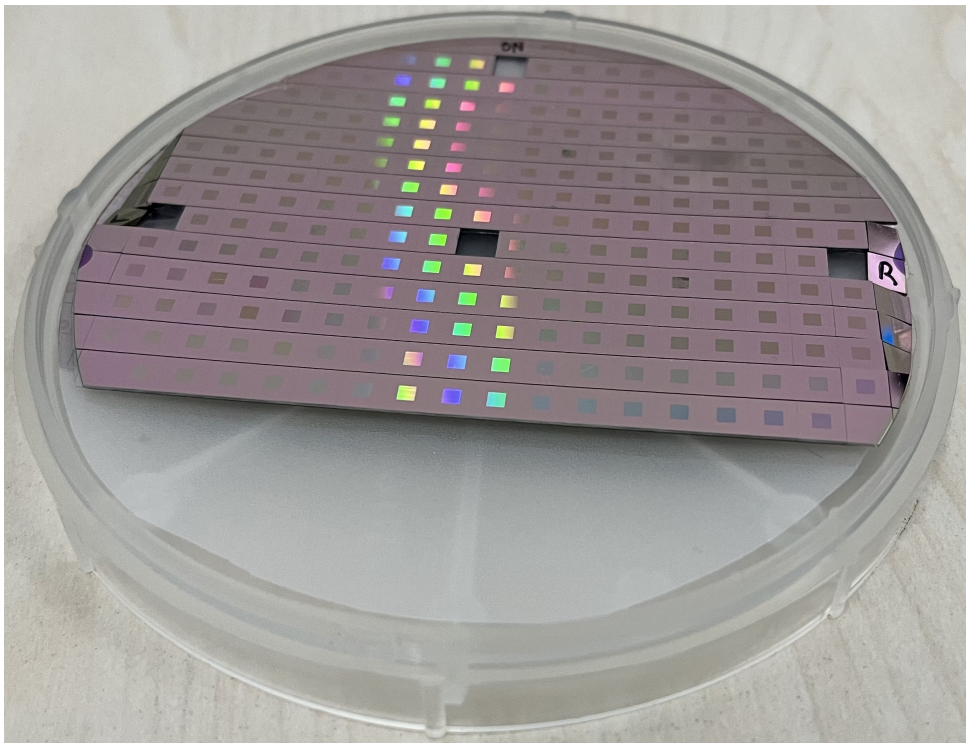

Figure 3.17: Silicon wafer with fabricated devices.

3.6.2 Profile and periodicity characterization

To inspect and provide structural characterization of a sample, a S neox profilometer, commercialized by SENSOFAR, was employed to analyze the profile of the Pd surface. Fig. 3.18 presents the profilometry results for a specific sample. SEM imaging was performed using an Inspect F electron microscope, which facilitated both visual inspection of the grating and the measurement of its periodicity. Fig.3.19 displays the SEM images of the sample.

The results of this characterization enable the evaluation of structural parameters, underscoring that the HMM generates a design that is fabricable. Additionally, the real grating can be computationally compared to the nominal design in terms of its spectral properties.

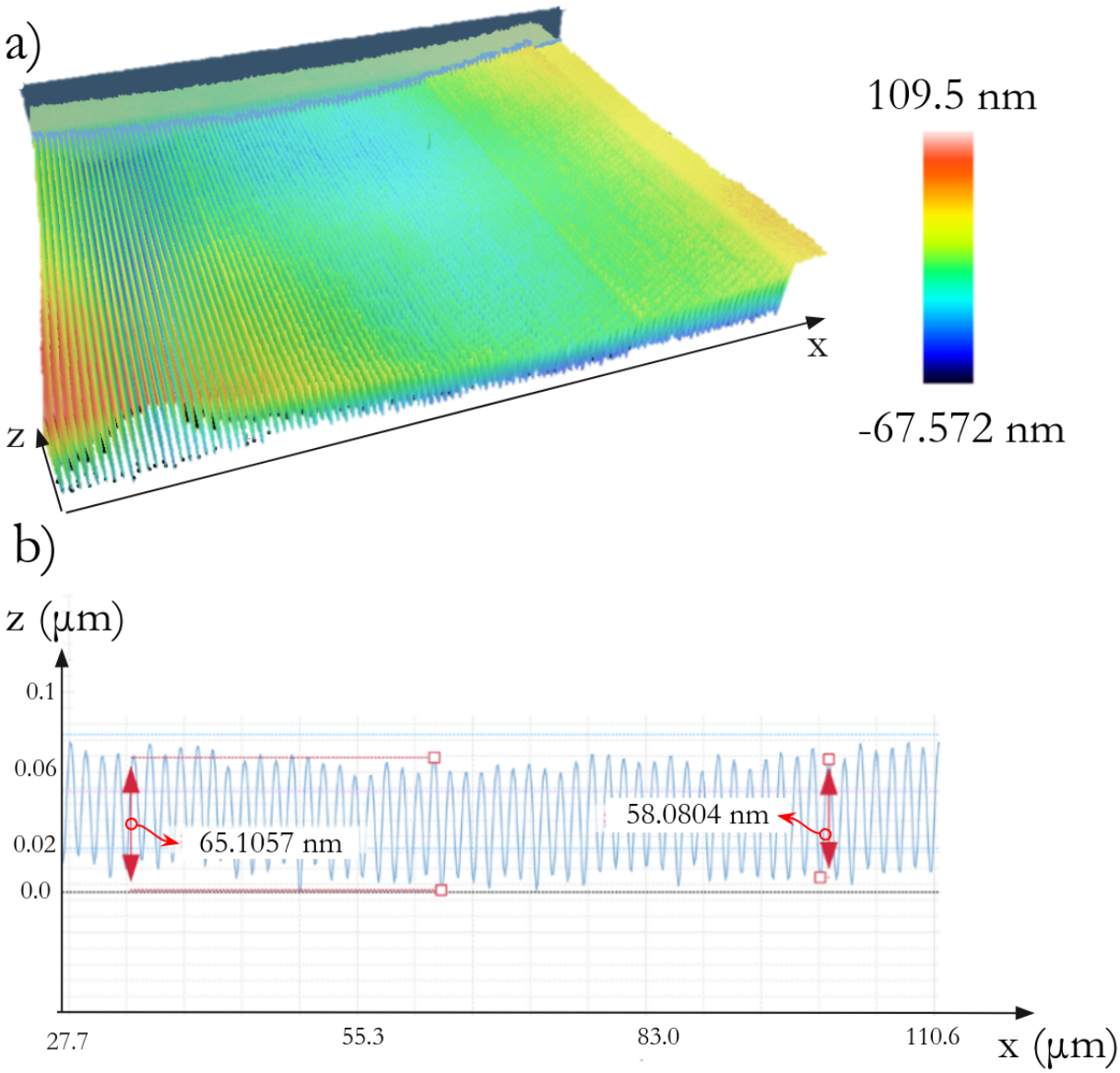

Figure 3.18: Optical profilometer data. a) Metallized measured area. b) Cross section of surface profile and measurement points.

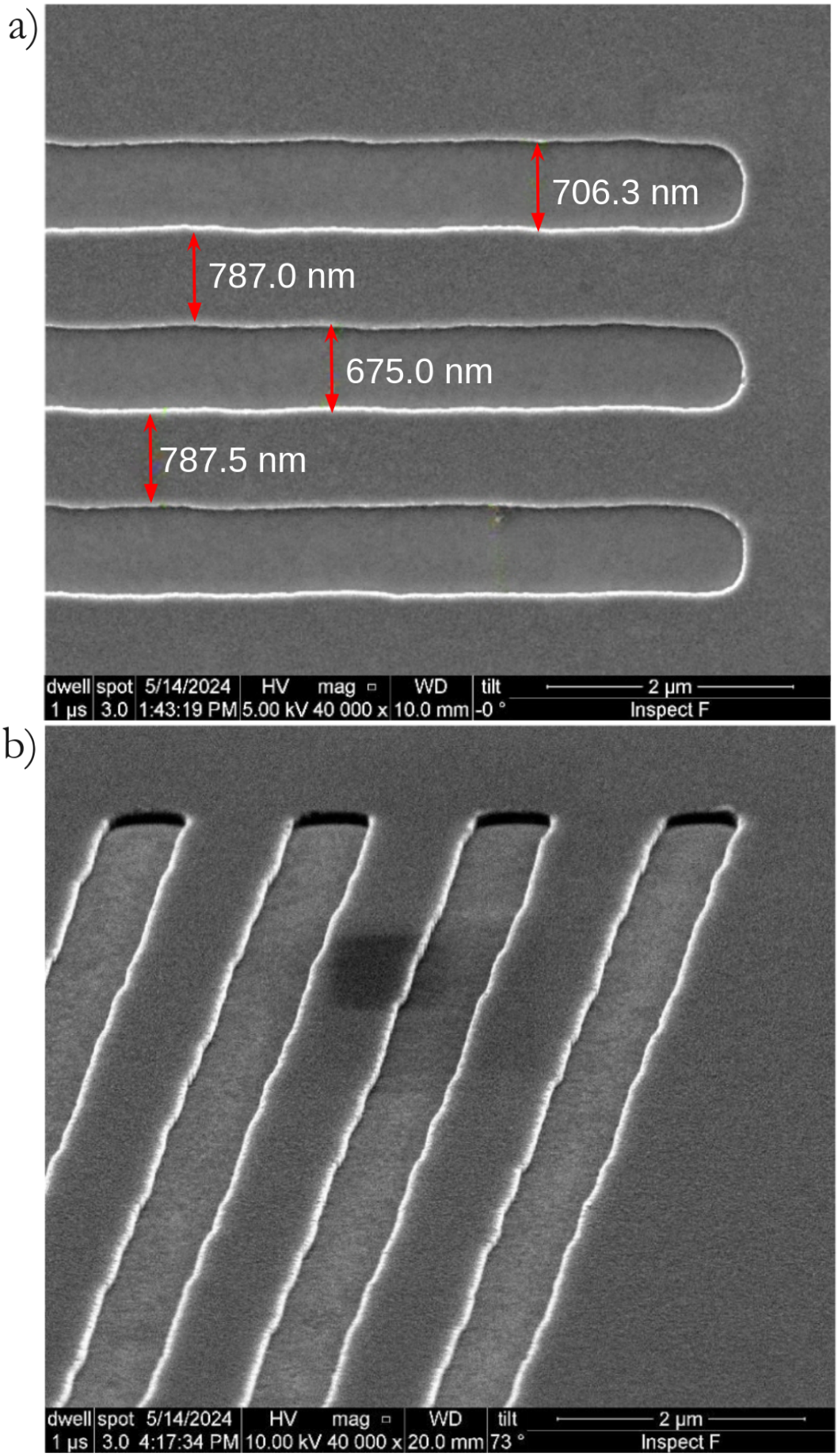

Figure 3.19: Scanning Electronic Microscopy images. a) Periodicity measurement. b) 73° image.

3.7 Spectral Comparison Between Fabricated and Nominal Grating

To estimate the impact of fabrication variations in structural parameters on the spectrum and sensitivity of the grating, a numerical comparison was conducted in the plane wave regime. Under identical conditions, the numerically calculated spectrum for the nominal parameters of the designed grating was compared with that of the fabricated device. For the real device parameters, a variant periodicity model was employed, based on the measurements shown in Fig. 3.19a. For the amplitude, the mean value of the measured points in Fig.3.18b was used, resulting in a characterized parameter of $h_{ch} = 30.8\,\text{nm}$. This approach approximates the experimental spectra of the device by considering periodicity variations measured over two grating periods and an average amplitude value. Optical constants for Pd were adopted in accordance with (Johnson e Christy,1972).

Fig.3.20a illustrates a clear and expected resonance shift, as the resonance position is highly sensitive to periodicity variations. Fig.3.20b presents a comparison of sensitivity and the corresponding wavelength that maximizes it. From this comparison, three sensitivity peaks can be identified. The first peak occurs in the region immediately before plasmonic coupling, representing the highest theoretical sensitivity. However, this peak is unrealistic because it corresponds to the transition from a propagating diffracted wave to an evanescent wave, which does not exist in practice. This discrepancy arises because, in an experimental environment, the incident field is not a pure plane wave but a beam with a degree of divergence. Consequently, this peak is drastically reduced in real scenarios.

The second highest sensitivity peak and its location on the spectrum are more relevant for practical applications, in the image the coordinates are shown to indicate the spectral position of the maximum sensitivity point. A 46 nm shift was observed between the nominal and characterized grating points of maximum observable sensitivity. This highlights that, depending on fabrication precision, some

optical sources initially considered may not be suitable for interrogating the real device. This result, although approximate since it only considers two periods of the real device, indicates that devices designed with the HHM can be produced by widely adopted fabrication procedures with similar sensitivity to the theoretical one.

It is also important to note that the variable periodicity allows coupling at nearby wavelengths, leading to additional resonances due to the splitting effect. Since the focus here is on the position and sensitivity of the resonance closest to the wavelength of incidence, these secondary and split resonances are not shown in Fig. 13b. The selection of the spectral region to be employed in a measurement system based on these devices should be determined following a thorough far-field reflectance spectrum measurement. The proximity of the coupled wavelengths could, potentially, reduce the sensitivity if they are close enough and lead to a widening of the final resonance obtained.

The amplitude variation has a stronger effect on the sensitivity and its variations due to fabrication error can affect the sensitivity of the real device. From a fabrication perspective, it is expected that the periodicity variation is the dominant error compared to amplitude variation since the depth of the etching process can be more easily controlled compared to the lithography defined pattern of the periodic surface, in which fabrication tolerances can affect the periodicity variation due to edge roughness.

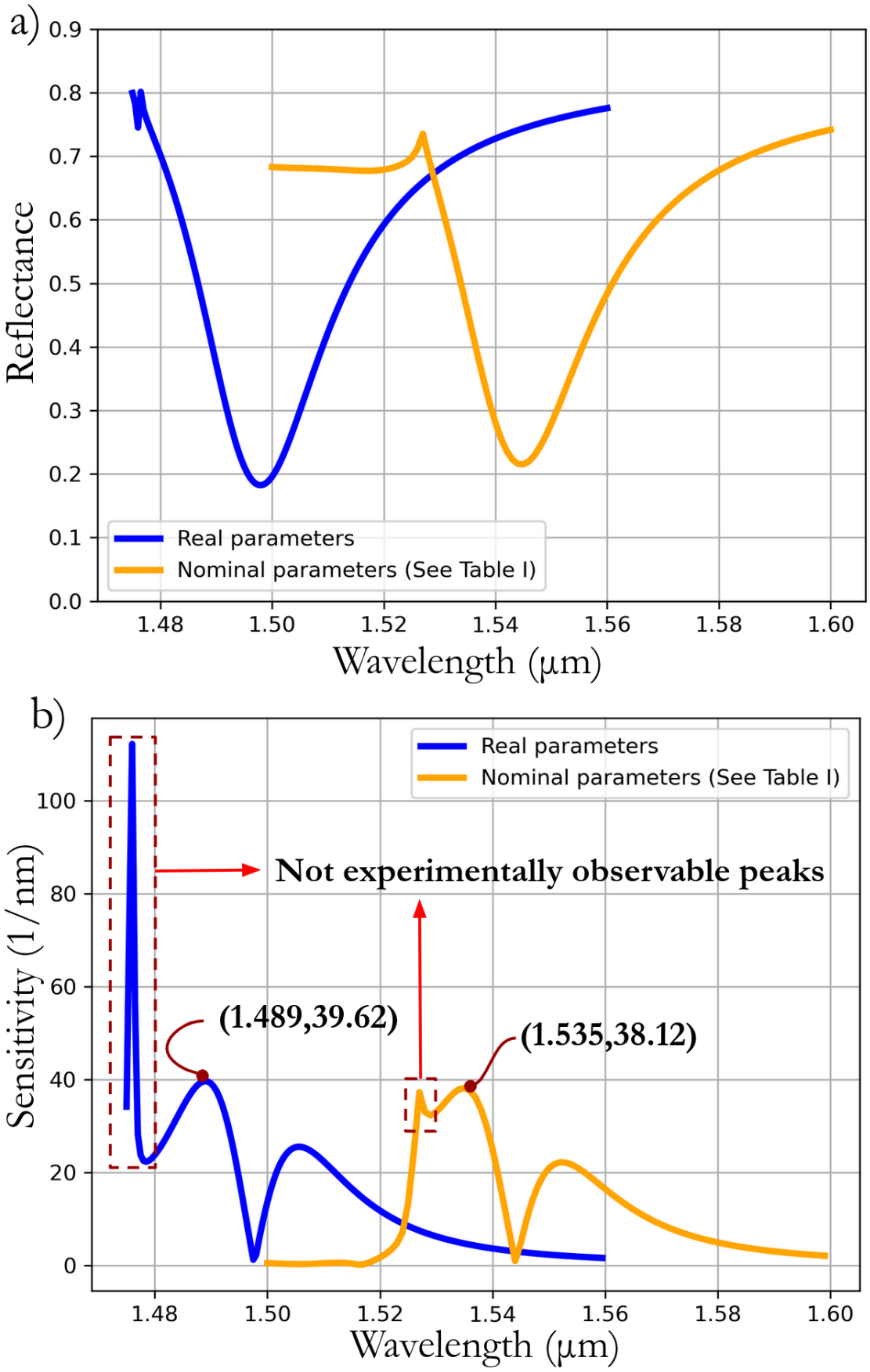

Figure 3.20: Numerical calculation for nominal and characterized grating parameters reflectance. a) Resonance curves. b) Sensitivity curves alongside coordinates of experimentally observable peaks.

Chapter 4

Tunable Diode Laser Plasmonic Grating Spectroscopy

The design and development of portable plasmonic embedded measurement systems represent a significant engineering challenge, aimed at delivering the high sensitivities observed in devices based on such physical phenomena to field applications. This chapter proposes the Tunable Diode Laser Plasmonic Grating Spectroscopy technique to achieve a system architecture in which narrower resonances observed in metallic diffraction gratings enable the spectral detection of analytes. The primary application investigated is hydrogen sensing using Palladium (Pd) and Niobium (Nb) hydride-forming structures. Analytical and numerical simulations are employed to assess the influence of hydrogen gas presence on the metal dielectric function and structural parameters. It is demonstrated that highly linear detection can be achieved using spectral detection systems, and in the case of an Nb grating on a flexible substrate, a theoretical ppm limit of detection is attainable.

4.1 Portable Plasmonic Measurement Systems and the Hydrogen Sensing Problem

The Surface Plasmon Resonance (SPR) effect is typically observed in prism-based coupling schemes (Kretschmann,1971; Otto,1968b), and most proposed sensing devices and systems operating based on this effect are configured accordingly (Liedberg et al.,1983). Several portable devices utilizing the Kretschmann configuration have already been reported in the literature, including those designed for both angle-resolved and wavelength-resolved measurements (Masson,2020; Yesudasu et al.,2021). Notable examples include the *Biacore* (Karlsson et al.,2012), developed by the company of the same name and commercialized in 1990, as well as the *SPREETA* (Melendez et al.,1997), developed by Texas Instruments. These devices require precise alignment, and the quality of their measurements is highly dependent on the opto-mechanical system employed. Moreover, technologies based on this configuration tend to be bulky and challenging to integrate with other systems, as angle-based interrogation requires mechanical rotation of the device for resonant angle measurements, where greater linearity is observed.

Diffraction grating coupling is another configuration that enables the observation of the SPR effect, which can be analyzed in both the angular and spectral domains. This configuration facilitates the narrowing of the resonance curve (Arora et al.,2018), opening up the possibility of exploring alternative methods for interrogating the SPR effect in gratings through spectral variation, without the need for broadband light sources. This capability is of significant practical importance, as prism-coupled devices face two major impracticalities. The first is the necessity for angular variation of the sample to observe the effect, which becomes problematic in field implementations, particularly when developing portable and/or embedded systems. While broadband sources and spectrometers can be employed to address this issue, these components are bulky and difficult to integrate into practical field measurement systems, limiting their use primarily to laboratory-based technologies.

Given the resonance narrowing in diffraction gratings, it is worth exploring methods to achieve the required spectral variation for grating resonance observation at a fixed angle—without relying on broadband sources—to develop an interrogation configuration for the SPR phenomenon that overcomes the aforementioned impracticalities (De Freitas Fernandes et al.,2022). In this context, the Tunable Diode Laser Plasmonic Grating Spectroscopy (TDLPGS) technique is proposed.

This chapter presents a system architecture for a practical and portable device that employs a Distributed Feedback (DFB) laser capable of operating under two regimes. First, thermal control is proposed to achieve linear spectral variation, enabling the identification of the most sensitive part of the spectrum. This approach could be employed with gratings in gold (Au) or silver (Ag), materials for which narrower resonances are expected. Additionally, a sinusoidal wavelength modulation scheme is introduced through modulation of the injection current. While thermal control has been previously suggested for fast switching in a communication context (Ueno et al.,2015), to the best of the author's knowledge, its use for interrogating plasmonic devices has not been yet explored and it consists in a novel proposal of this work.

The proposed technique is then applied to the sensing of hydrogen gas (H_2) using palladium (Pd) and niobium (Nb) optimized gratings, metals known to form hydrides in the presence of this gas, resulting in optical and structural variations. This application is selected due to the critical need for monitoring H_2 in various industries (Le et al.,2023), as well as the challenges associated with handling the gas. Hydrogen has a Lower Explosive Limit (LEL) of only 4% volume concentration, is a small molecule with a high risk of leakage, and poses significant safety concerns in its storage and transportation. Additionally, when ignited, its flame is invisible (PubChem,2025; Yang et al.,2021). Another motivation is the exploration of periodicity changes in the grating when the film is exposed to hydrogen, which increases sensitivity. This approach contrasts with previously suggested H_2 sensors that utilize periodic structures, such as Pd-coated Fiber Bragg Gratings (FBGs),

which detect the presence of the gas by measuring the strain caused by hydrogen absorption and its effect on the internal grating periodicity. In this work, the material loaded with the gas serves as the periodic structure, leading to a more direct transducing mechanism (Sutapun,1999; Trouillet et al.,2006; Silva et al.,2013). it is also, according to the author's knowledge, the first detailed analysis of optical and mechanical variations on plasmonic properties of metallic hydrides.

Optimized structures are obtained using the Harmonic Minimization Method (HMM) (Fernandes et al.,2025), and the technique is investigated through analytical models that account for gas diffusion in the metals, the dielectric function of the hydride, and the elastic expansion of the films. Numerical simulations are employed to validate the technique and provide calculations of the diffracted fields.

It is shown that a system architecture compatible with a portable, embedded system can achieve high linearity and, depending on the choice of material, a ppm limit of detection.

4.2 Diffraction Grating Design and Physical Aspects of Hydrogen Adsorption

4.2.1 Diffraction Grating Design by Harmonic Minimization Method

To simulate the proposed technique with maximum sensitivity, a design optimization technique should be employed to obtain values for the periodicity and amplitude of the grating that maximize the sensitivity S, defined as the absolute value of the first derivative of the reflectance with respect to wavelength: $S = \left|\frac{dR}{d\lambda}\right|$. In this work, the diffraction gratings are designed in a rectangular shape, as their fabrication is achievable through widely adopted processes such as optical or electron-beam lithography. The optimized structures are obtained using the Harmonic Minimization Method (HMM), considering 20 harmonics (Fernandes et al.,2025). This approach

allows for the determination of optimal grating parameters by first optimizing a sinusoidal grating using a Rayleigh-based description of its reflectance (Rayleigh,1907). From the resulting profile function, a rectangular grating with similar sensitivity is calculated. This method provides good initial guesses for both parameters, enabling the use of gradient-based optimization. For the amplitude, it is known that observing the Surface Plasmon Resonance (SPR) effect typically requires grating amplitudes on the order of tens of nanometers. Consequently, values between 10 nm and 100 nm are explored, with a resolution of 0.01 nm. For the periodicity, an initial estimation can be derived from the grating equation using the wavevectors illustrated in Fig. 4.1.

$$k_l = k_x + l\frac{2\pi}{\Lambda}, \tag{4.1}$$

employing the expression for the surface plasmon wavevector,

$$k_{sp} = k'_{sp} + jk''_{sp}, \tag{4.2}$$

with (Fontana2004,2004)

$$k'_{sp} = k_0\sqrt{\frac{\epsilon'\epsilon_1}{\epsilon' + \epsilon_1}}, \tag{4.3}$$

$$k''_{sp} = k'_{sp}\frac{\epsilon''\epsilon_s}{2\epsilon'\left(\epsilon' + \epsilon_s\right)}, \tag{4.4}$$

with $\epsilon_m = \epsilon' - j\epsilon''$ being the metal dielectric function and $\epsilon_s = \eta_s^2$ being the dielectric function of the sensing medium. Then, under normal incidence regime and satisfying the coupling condition $k_l = k_{sp}$, the expression for the grating periodicity initial guess

$$\Lambda \approx \pm l\lambda\left(\frac{\epsilon'\eta_s^2}{\epsilon' + \eta_s^2}\right)^{-1/2}. \tag{4.5}$$

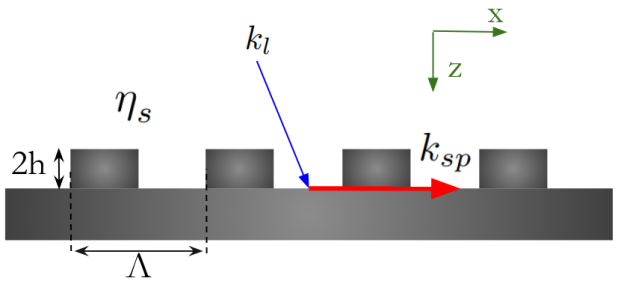

Figure 4.1: Wavevector of excited surface plasmon on a diffraction grating.

4.2.2 Diffusion of Hydrogen in Metal Gratings

It is important to propose a model for the diffusion of hydrogen in the metallic grating to justify the approach for effective dielectric function calculations and to derive an equation for the response time of the sensing system. Given that the grating amplitude is on the nanometric scale, the diffusion is modeled as diffusion across a planar surface. This simplification is justified by the goal of obtaining an estimation of the sensor response time and the concentration distribution, as a thorough analysis of the diffusive behavior over the periodic geometry is beyond the scope of this work. Therefore, by considering an interface between a solution of H_2 in air and a metal at $z = 0$, and applying Fick's second law, the diffusion process can be described.

$$\frac{\partial n(z,t)}{\partial t} = D\frac{\partial^2 n(z,t)}{\partial z^2}, \tag{4.6}$$

for the conditions

$$\lim_{z\to\infty} n(z,t) = 0, \tag{4.7}$$

$$n(z \neq 0, t = 0) = 0, \tag{4.8}$$

one can obtain the following profile for the gas concentration n

$$n(z,t) = n_0 exp\left(-\frac{z^2}{4Dt}\right). \tag{4.9}$$

with n_0 being the fixed concentration on the surface. The response time t_r is then proposed as the time necessary for the optical power to decay by a factor of $exp(-1)$ at $z = \delta(n, \lambda)$ with $\delta(n, \lambda)$ denoting the concentration-dependent penetration depth

$$\delta(n, \lambda) = \frac{1}{2k_0 Im[\eta_{ef}(n, \lambda)]}, \tag{4.10}$$

leading to

$$t_r(n, \lambda) = \frac{1}{16D\{k_0 Im[\eta_{ef}(n, \lambda)])\}^2}. \tag{4.11}$$

The equation above is used to calculate the response time for both materials in the concentration range investigated in this work.

4.2.3 Effective Dielectric Function Modeling

Considering the diffusive behavior of hydrogen (H) atoms in palladium (Pd) due to gas molecule dissociation, a model for the effective dielectric function must be employed. For this purpose, a specific consideration regarding the concentration distribution in Eq. 4.9 is necessary. The equation predicts a concentration that varies with depth into the metal, meaning that the intruder (H) is not uniformly distributed within the grating. In this work, we adopt the approximation that such variations have a negligible effect on the effective refractive index of the hydride, η_{ef}. This assumption is reasonable in the limit of low gas concentrations, leading to an approach in which the optical properties of the hydride are treated as isotropic.

In light of this argument, two main approaches for modeling η_{ef} are found in the literature: the Bruggeman (Bruggeman,1935) and Maxwell-Garnett (Garnett,1904) models. The Bruggeman model presents certain limitations, such as symmetry (i.e., switching the host and intruder materials yields the same result), which is undesirable in this case, where the host is a metal. Clearly, if the roles are reversed—making H the host and Pd the intruder—the dielectric function should differ from the original case. Additionally, a comparison between these models for a metal-

lic host and a spherical intruder molecule, both with spherical geometry, has been reported (Markel,2016a). This comparison demonstrates that the Maxwell-Garnett approach more effectively describes the dielectric function of the composite, as supported by numerical data. Therefore, in this work, the effective dielectric functions of both PdH_n and NbH_n are modeled using the Maxwell-Garnett approximation (Markel,2016b), expressed in terms of the refractive index of the hydride.

To obtain the effective refractive index of the metal under hydrogen load, one needs to consider a particular volume V with the macroscopic electric field constant within it containing a number N of particles of linear polarizability α. The considered scheme is shown in Fig. 4.2.

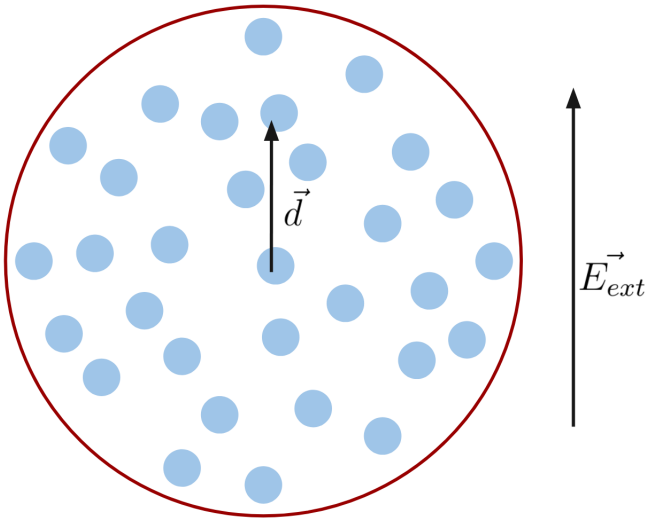

Figure 4.2: Collection of dipoles subjected to an external field.

Considering that this volume is subjected to an external electric field $\vec{E_{ext}}$, one must state that the interaction between the dipoles contribute to a net zero electric field and is considered that each dipole acquires dipole moment $\vec{d} = \alpha\vec{E_{ext}}$. That leads to a total dipole moment of the volume V,

$$\vec{d_{tot}} = N\alpha\vec{E_{ext}} \tag{4.12}$$

Considering that the our composite sample will have an effective dielectric function ϵ_{ef} in a host medium of dielectric function ϵ_h, one can state that the polarization vector of the sample is

$$\vec{P} = \frac{\epsilon_{ef} - \epsilon_h}{4\pi}\vec{E} \tag{4.13}$$

with $\vec{E}$ being the field inside the volume V. The total dipole moment is then

$$\vec{d_{tot}} = V\vec{P} = V\frac{\epsilon_{ef} - \epsilon_h}{4\pi}\vec{E}. \tag{4.14}$$

At this point is important to obtain an expression for the electric field of the dipole inserted in the host medium. Employing Gauss's law

$$\nabla \cdot \vec{D} = \epsilon_h \nabla \cdot \vec{E} = 4\pi c \tag{4.15}$$

where c is the electrical charge density, one can obtain for the field of the dipole,

$$\vec{E_d} = \frac{1}{\epsilon_h}\left[\frac{3\vec{r}(\vec{r}\cdot\vec{d}) - \vec{d}}{r^3} - \frac{4\pi}{3}\delta(\vec{r}\vec{d})\right]. \tag{4.16}$$

Defining the total field as

$$\vec{E}(\vec{r}) = \vec{E}_{ext}(\vec{r}) + \sum_{n=0}^{N}\langle\vec{E}_d^n(\vec{r})\rangle\,, \tag{4.17}$$

with $\vec{E}_d^n(\vec{r})$ being the field of n -th dipole. Calculating the average term with the use of Eq. 4.16 , one can write

$$\langle\vec{E}_d\rangle = \frac{1}{V}\int_{r<R}\vec{E}_d(\vec{r} - \vec{r^n})d^3r = -\frac{4\pi}{3\epsilon_h}\vec{d}, \tag{4.18}$$

and for the total field 4.17

$$\vec{E}(\vec{r}) = \vec{E}_{ext}(\vec{r}) + N(-\frac{4\pi}{3\epsilon_h}\vec{d}), \tag{4.19}$$

using the relation $\vec{d} = \alpha\vec{E}$,

$$\vec{E}(\vec{r}) = (1 - \frac{4\pi N}{3\epsilon_h V}\alpha)\vec{E}_{ext}(\vec{r}). \tag{4.20}$$

Equating Eqs. 4.12 and 4.14, and with the use of Eq. 4.20,

$$\epsilon_{ef} = \epsilon_h + \frac{4\pi(\alpha N/V)}{1 - (4\pi/3\epsilon_h)(\alpha N/V)} \tag{4.21}$$

which is the Maxwell-Garnett equation for the effective medium. Writing in terms of the molar concentration and emplying the constitutive relation $\epsilon = \eta^2$, one can re-write Eq. 4.21 as

$$\eta_{ef} = \sqrt{n_h^2 + \frac{4\pi\alpha N a\rho}{1 + (4\pi/3n_h^2)(\alpha N a\rho)}}, \tag{4.22}$$

in which the polarizability α can be obtained by solving the Laplace equation for the sphere considered in Fig. 4.2 and choosing appropriate boundary conditions at the surface and at the infinity. This results in a polarizability,

$$\alpha = R_H^3 n_h^3 \cdot \frac{\eta_i^2 - \eta_h^2}{\eta_i^2 + \eta_h^2}, \tag{4.23}$$

with R_H as the van der Walls radius of H according to (Bondi,1964), N_a is the number of Avogadro, ρ the concentration of intrusive agents in mol/m^3 and η_i and η_h are the refractive indexes of the intruder and the host, respectively. To obtain a relation between ρ and the atomic concentration n one can write

$$\rho = n \cdot \frac{N_{mol}^m}{V} = n \cdot \frac{V/V_m^m}{V} = \frac{n}{V_m^m}, \tag{4.24}$$

with N_{mol}^m being the mole number of metal in the sample, V the volume sample and V_m^m the molar volume of the metal. With these equations, one can calculate the optical effect of hydrogen presence on the metallic grating resonance.

4.2.4 Elastic expansion in Metal Films Under Hydrogen Load

To model the expansion of the grating under hydrogen loading and its effects on the structural parameters, several considerations are necessary. In this work, we assume an elastic model for the metal expansion. It is known that under heavy

hydrogen loading, the metal can exhibit plastic deformation; however, for the sake of simplicity, the effect of the plastic region on the grating resonance will be investigated in future works. An important detail of the metal layer behavior is the nature of the substrate. Rigid substrates, such as metals deposited over titanium (Ti) or chromium (Cr) adhesion layers, can suppress the lateral expansion of the film, leaving only the vertical expansion as observable. In the case of a flexible substrate, the film is free to expand laterally, and for a diffraction grating, this results in periodicity variation, which can significantly influence the sensitivity of the final system. It is also expected that, depending on the film thickness, some periodicity variation may occur even with rigid substrates.

With these arguments in mind, two scenarios are explored in this work. The first is a rigid substrate scenario, where no lateral expansion occurs, and the second is an ideally flexible substrate scenario, where the metal grating is free to expand laterally. Fig. 4.3 illustrates the vertical and lateral expansions, along with the associated proportional deformations ϵ_z and ϵ_x.

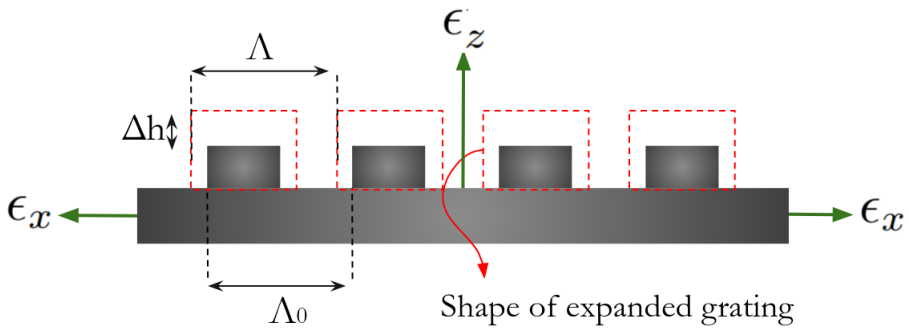

Figure 4.3: Expansion effect of the hydrogen absorption on the grating structure. On the case of rigid substrate the variation on Λ is non-existent.

Considering that the proportional deformation associated with isotropic lattice expansion can be written as(Wagner et al.,2016)

$$\epsilon_0 = \frac{\Delta L}{L} = \alpha_H^{Pd/Nb} \cdot n, \tag{4.25}$$

with $\alpha_H^{Pd/Nb}$ being the expansion factor with its value being adopted from (Peisl,1978) as $\alpha_H^{Pd} = 0.063$ and $\alpha_H^{Nb} = 0.058$. In the case of rigid substrates the expansion as-

sociated with ϵ_x is suppressed, but in the case of a flexible substrate one can state that $\epsilon_x = \epsilon_0$. For the case of vertical expansion the contribution of the Poisson effect must be considered and for Pd the one can write (Wagner et al.,2016)

$$\epsilon_z^{Pd} = \frac{3C_{44^{Pd}}}{4C_{11^{Pd}} + 8C_{12^{Pd}} + C_{44^{Pd}}} \cdot \epsilon_0 \tag{4.26}$$

and for Nb(Laudahn et al.1999)

$$\epsilon_z^{Nb} = (1 + \frac{C_{11}^{Nb} + 3C_{12}^{Nb} - 2C_{44}^{Nb}}{C_{11}^{Nb} + C_{12}^{Nb} + 2C_{44}^{Nb}}) \cdot \epsilon_0 \tag{4.27}$$

with C_{ij}^{Pd} and C_{ij}^{Nb} being the elastic stiffness of Pd and Nb, respectively, which are obtained from the literature (Klein, 1968; Wagner et al., 2016; Bolef, 1961). With the Eqs. 4.25 to 4.27 it is possible to calculate the effect of a gas concentration n on both amplitude and periodicity of the grating as

$$\Delta\Lambda = \lambda \cdot \epsilon_x \tag{4.28}$$

and

$$\Delta h = h \cdot \epsilon_z^{Pd/Nb}. \tag{4.29}$$

4.3 Tunable Diode Laser Plasmonic Grating Spectroscopy Technique and Simulator Algorithm

4.3.1 Proposed System Architecture

The models proposed in Section II are now employed to validate the Tunable Diode Laser Plasmonic Grating Spectroscopy (TDLPGS) technique proposed in this work. To achieve fixed-angle operation, a setup based on the observation of the fundamental mode of diffraction of the grating under normal incidence is ideal, as this mode exhibits higher sensitivity and narrower resonances. Additionally, the

alignment process is simplified under normal incidence conditions. The proposed system architecture is fiber-based, featuring decoupling from the fiber to the sensing medium, reflection at the grating, and recoupling into the fiber, as illustrated in Fig. 4.4.

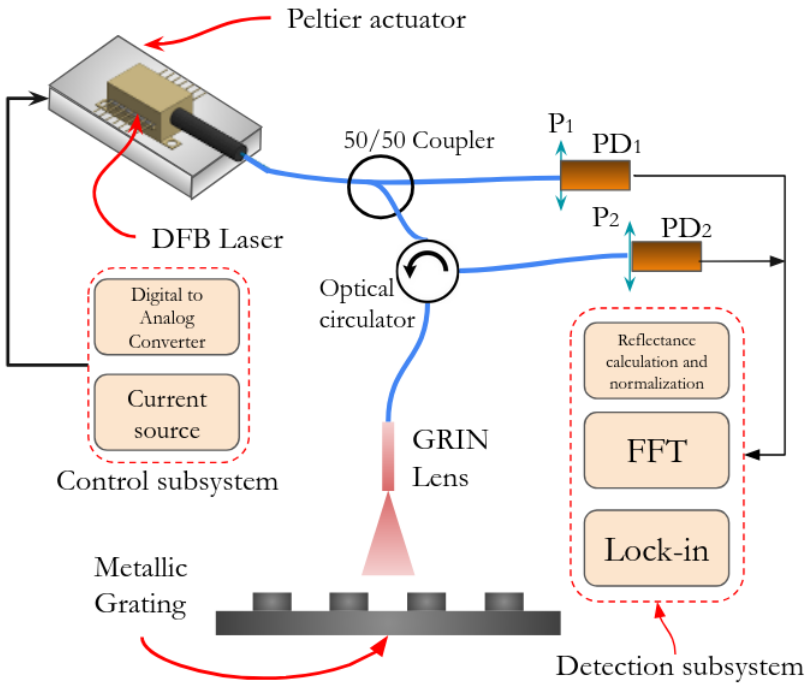

Figure 4.4: Proposed system architecture.

The setup incorporates a Distributed Feedback (DFB) laser, where both thermal and current variations can be utilized to modulate its emission wavelength. Given that the resonance widths for the materials investigated here are expected to be on the order of 10 nm, it is preferable to modulate the emission wavelength through current variation in a Wavelength Modulation Spectroscopy (WMS) scenario. This approach is complemented by spectral detection systems such as Fast Fourier Transform (FFT)-based detection and lock-in amplifiers. The beam emitted by the laser is split by a 50/50 coupler, with half of the optical power directed to the system and the other half detected by photodetector PD_1. The transmitted beam then passes through another optical coupler, where half of the input power is directed to a Gradient Refractive Index (GRIN) lens for efficient coupling and decoupling from the fiber. After decoupling, the beam is reflected by the grating and then coupled back into the fiber, where it is detected by photodetector PD_2. Each photodetector

is paired with a polarizing film to ensure that only the intensities associated with p-polarization are measured. The reflectance is calculated as the ratio of the measured intensities from PD_2 and PD_1. The reflectance curve is then normalized and analyzed using the FFT and lock-in subsystems.

A practical consideration involves the distance between the tip of the fiber and the grating. It is crucial to ensure that the area associated with the beam diameter of the same order as the grating area, otherwise, the grating will reflect the beam as if it were a flat surface.

4.3.2 Simulation Algorithm

To simulate the effect of hydrogen presence on the fundamental mode plasmonic resonance of the grating under normal incidence and to obtain results considering both detection techniques, an algorithm was developed to implement analytical calculations for the effective dielectric function of the metal and the elastic expansion effects on the structural parameters of periodicity and amplitude. The results of optical and mechanical variations for a specific concentration nn are then used in a numerical simulation based on the Finite Element Method (FEM) to calculate the reflectance of the grating. The numerical computation employs a model of a horizontally infinite grating implemented through a Floquet-type periodic boundary condition. The distance from the grating to the emission port is fixed at $10\lambda_i$, where λ_i is the design incident wavelength, and a spectral range from 1520 nm to 1580 nm is used. The mesh is generated with triangular elements, with the largest and smallest sizes set to 300 nm and 0.59 nm, respectively.

The data obtained from the numerical simulation is then processed by the detection routine, which includes a detection method based on the maximum value of the magnitude of the Fast Fourier Transform (FFT), implemented using the Cooley-Tukey algorithm (Cooley e Tukey, 1965), as well as a digital lock-in amplifier (Michels e Curtis, 1941; Kishore e Akbar, 2020) to analyze the signals. The overall algorithm used to obtain the results of this work is presented in Algorithm

2.

Algorithm 2 Pseudocode for simulation of TDLPGS.

input $\theta_i, Re(\eta_m), Im(\eta_m), l, \lambda_i, \eta_s, n_{max}$
$[h, \Lambda] \leftarrow$ HHMoptimization$[\theta_i, Re(\eta_m), Im(\eta_m), l, \lambda_i, \eta_s]$;
$n \leftarrow$ LinearVec[0,n_{max}];
$\eta_{ef} \leftarrow$ Eq. (12);
$\Delta h \leftarrow$ Eq. (19);
if $substrate == flexible$ **then**
    $\Delta\Lambda \leftarrow$ Eq. (18);
else$\Delta\Lambda = 0$;
end if
$t_r \leftarrow$ Eq. (11);
R = CalculateReflectance$(\theta_i, \eta_{ef}, l, \lambda_i, \eta_s.\Delta h, \Delta\Lambda)$;
FFTsignal = FFTanalysis[R];
LockInsignal = LockInAnalysis[R];
Generate plots

Initially, the angle of incidence θ_i, the metal refractive index η_m, the diffraction order l, the design wavelength of incidence λ_i, the sensing medium refractive index η_s, and the maximum concentration n_{max} are input. The optimal rectangular grating is then obtained, consisting of the pair of structural parameters $[h, \Lambda]$. Subsequently, an equally spaced linear vector n, representing the concentration range to be explored, is created. Eq. 4.22 is employed with n to calculate the refractive index of the hydride η_{ef}, while Eq. 4.29 is used to determine the amplitude variation. In the case of a flexible substrate, Eq. 4.28 is applied to compute the periodicity variation. With this information, the response time t_r is calculated. The numerical model is then employed to compute the reflectance associated with the desired diffraction order. Finally, R is a three-dimensional matrix that stores the reflectance over wavelength for each combination of elements from the η_{ef}, Δh, and $\Delta\Lambda$ vectors.

4.4 Results

4.4.1 Study of Optical and Mechanical Variations on Plasmonic Resonance

Considering the previously proposed models, each transducing mechanism is initially analyzed separately to understand the effects of dielectric function, amplitude, and periodicity variations on the sensor response. Subsequently, the combined effects are evaluated for both rigid and ideally flexible substrates.

According to the literature, hydrogen at ambient pressure and temperature forms the hydride PdH_n with an atomic concentration of $n \leq 0.7$(Kawae et al..2020). Therefore, this concentration range will be examined.

For the Pd grating presented in Table 4.1, the effect of optical variations on resonance, as indicated in Table 4.2, is illustrated in Fig. 4.5.

Table 4.1: Gratings obtained by HMM for $\lambda_i = 1531$ nm. Optical constants according to (Johnson e Christy,1972) for Pd and according to(Golovashkin et al.,1969b) for Nb

$Material$	$h(nm)$	$\Lambda(nm)$
Pd	31.74	1525.64
Nb	34.12	1526.38

Table 4.2: Optical and mechanical variations for Pd grating.

n	$Re(n_{ef})$	$Im(n_{ef})$	$h(nm)$	Λ (nm)
0	2.93	8.25	-	-
0.1	8.21	8.42	32.14	1535.25
0.2	10.01	11.50	32.53	1544.86
0.3	9.82	13.57	32.94	1554.47
0.4	9.26	14.69	33.33	1564.09
0.5	8.75	15.30	33.73	1573.70
0.6	8.34	15.65	34.13	1583.31
0.7	8.01	15.87	34.53	1592.92

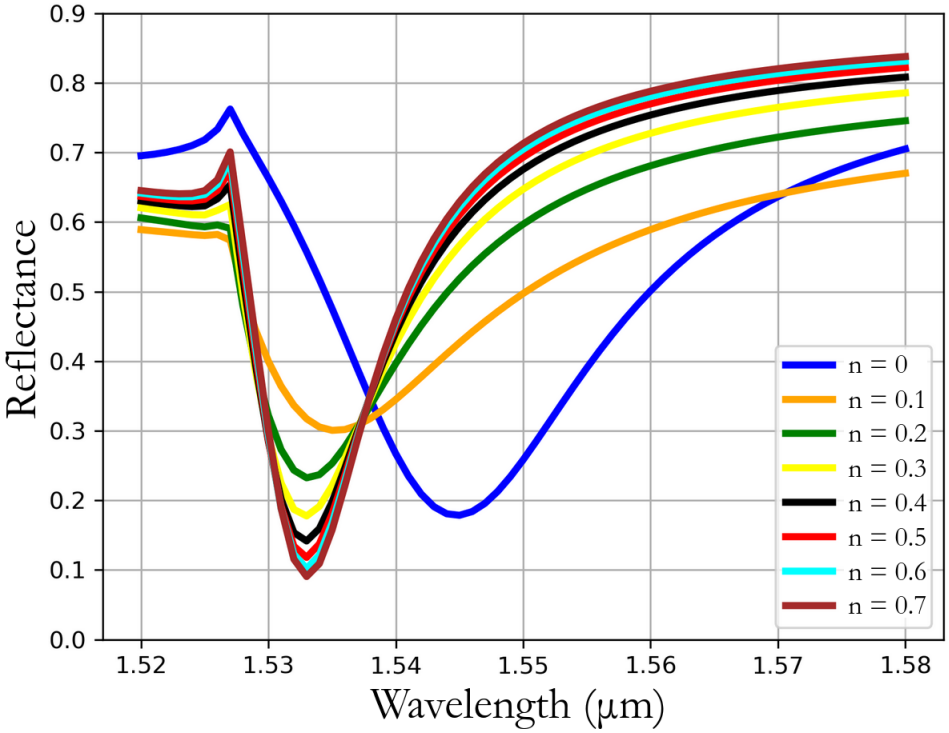

Figure 4.5: Effect of dielectric function variation on Pd grating's resonance curve for different concentrations n.

It can be stated that concentrations below 0.1 have a greater influence on the real part of the effective refractive index, shifting the resonance to significantly lower wavelengths. For higher concentrations, the effect of the imaginary part becomes dominant, with its increase leading to deeper resonances. This result suggests that, even for a non-modulated incident beam, it would be possible to detect low concentrations.

Next, the effect of mechanical variations on resonance is examined. Initially, only the elastic expansion in amplitude is considered. Fig. 4.6 presents the results corresponding to the variations outlined in Table 4.2.

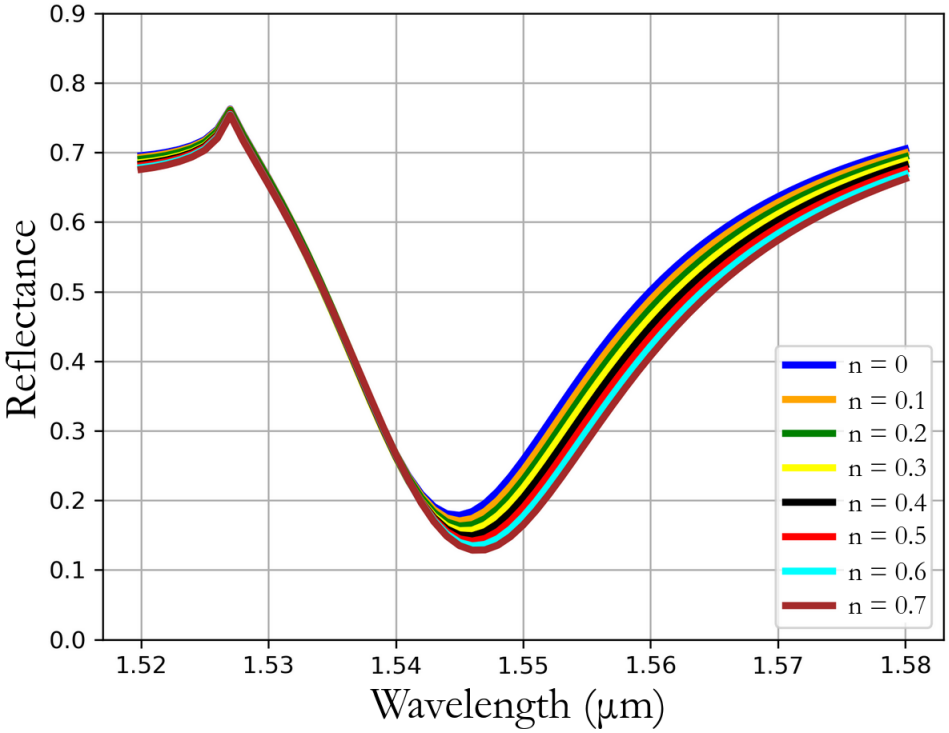

Figure 4.6: Effect of amplitude variation on Pd grating's resonance curve for different concentrations n.

From these results, we observe that as the amplitude deviates from the optimized value, higher quality factors are obtained, accompanied by deeper resonances. This mechanism can also contribute to the overall sensitivity of the device.

The variation in periodicity is constrained by the stiffness of the substrate, as previously mentioned. Here, we analyze the effect of this variation by considering an ideally flexible substrate, where the metal film is free to expand laterally. Under this assumption, Figure 4.7 presents the results for periodicity expansion alone.

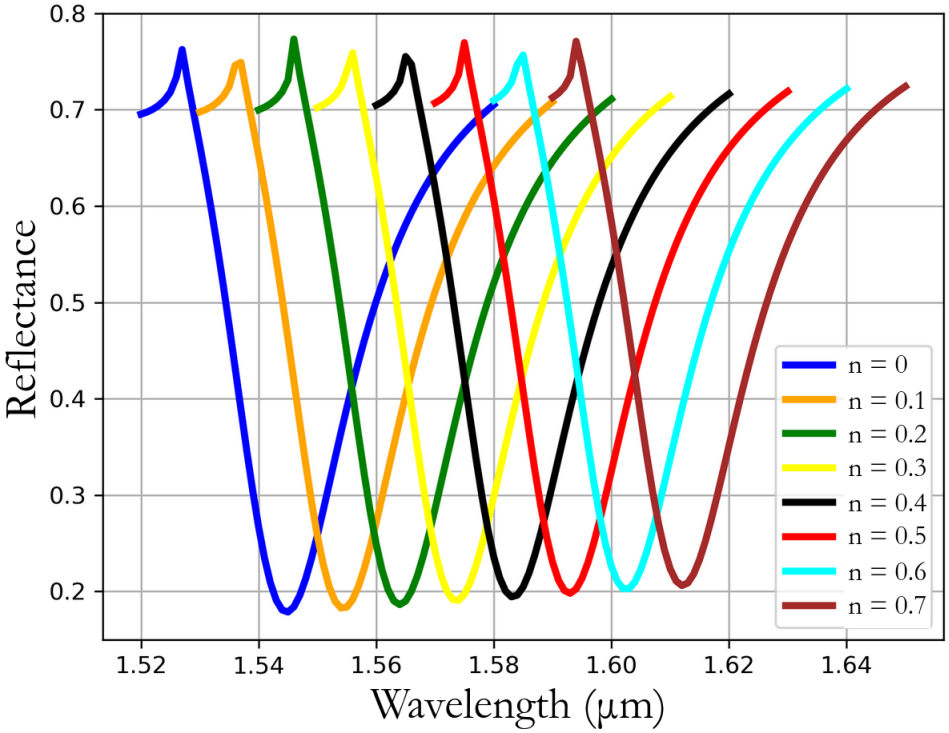

Figure 4.7: Effect of periodicity variation on Pd grating's resonance curve for different concentrations n.

It is evident that the use of flexible substrates can significantly enhance the system's sensitivity, as the resonance position is highly responsive to variations in the grating period. Another possibility is that, even with rigid substrates, some lateral expansion may occur in sufficiently thick films, where the upper part of the grating has some freedom to expand, potentially increasing sensitivity. The effect of periodicity variation has the potential to dominate the overall sensitivity of the device.

With each transduction mechanism analyzed separately, we can now examine how the device behaves in a scenario more representative of real-world conditions. Considering a rigid substrate, Figure 4.8 presents the results of optical and mechanical variations in response to hydrogen concentration, evaluated simultaneously.

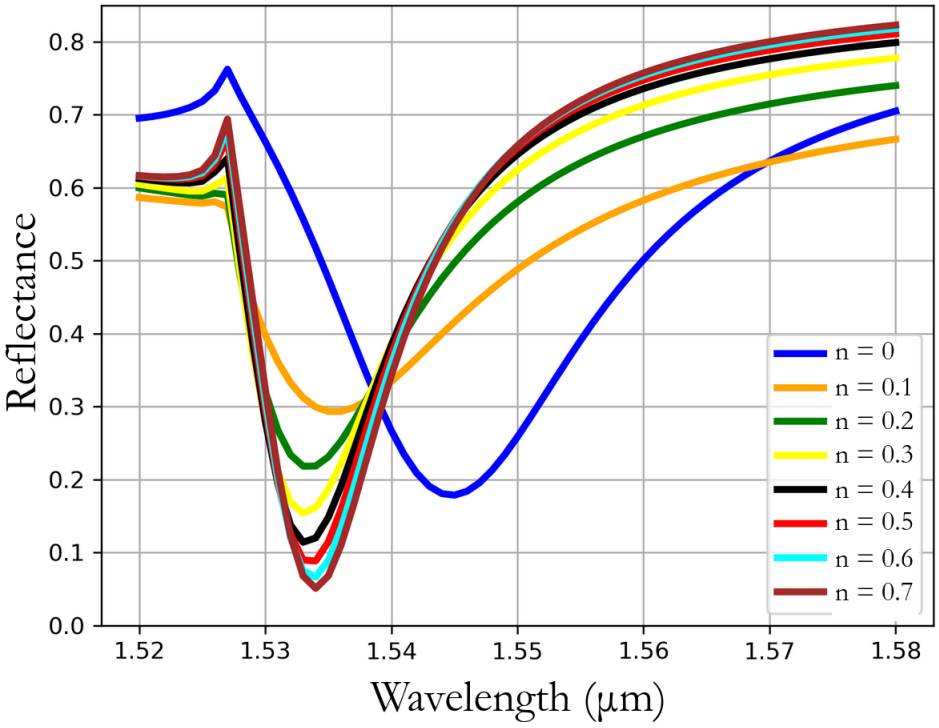

Figure 4.8: Effect of gas presence on Pd grating's resonance curve with rigid substrate for different atomic concentrations for different concentrations n.

For a scenario that involves an ideally flexible substrate, Fig. 4.9 presents the results for the same concentration range.

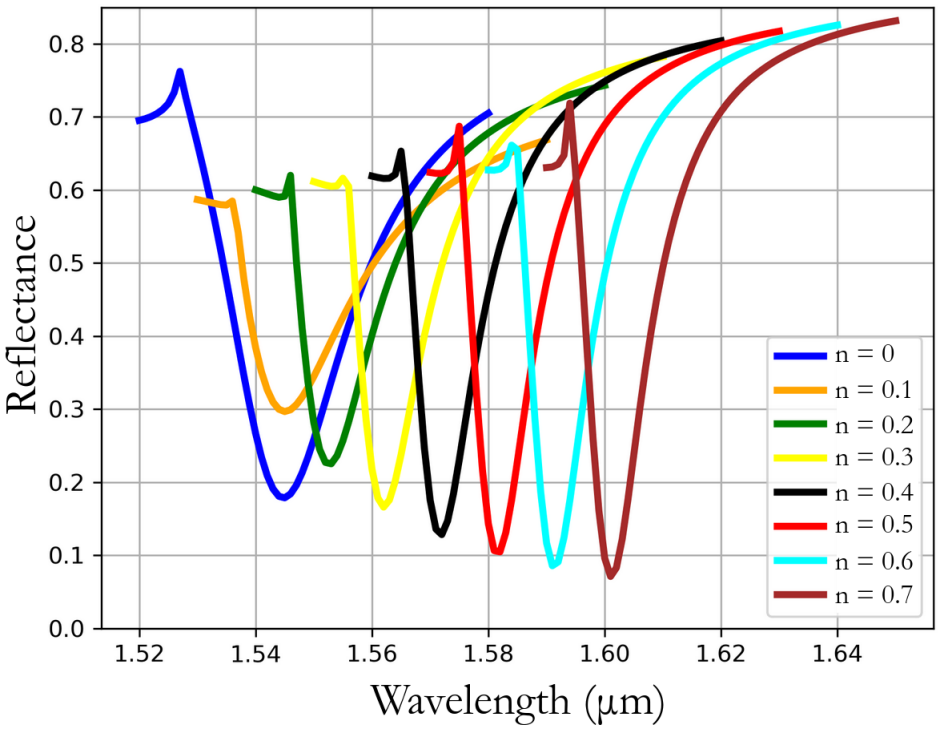

Figure 4.9: Effect of gas presence on Pd grating's resonance curve with flexible substrate for different concentrations n.

In the case of gratings designed with Nb, we analyzed the effects of absorption on the optical constants and structural parameters simultaneously for both substrate types, considering the grating presented in Table 4.1.

To perform the simulation, it is first necessary to determine the atomic concentration at which Nb begins to undergo plastic deformation. Beyond this concentration, the grating will no longer return to its initial dimensions if the concentration decreases. According to the phenomenological model(Hamm et al.,2015), this condition can be expressed as

$$n_{pl}^{Nb} = \frac{1.2}{d} \cdot Ln(5d), \tag{4.30}$$

for the critical concentration at which plastic deformation begins, as a function of film thickness d, we consider, for example, a 150 nm thick metal film, yielding $n_{pl} = 0.053$. Based on this value, simulations for the Nb device were conducted for $x \leq 0.05$. Figs 4.10 and 4.11 present the results for rigid and flexible substrates, respectively.

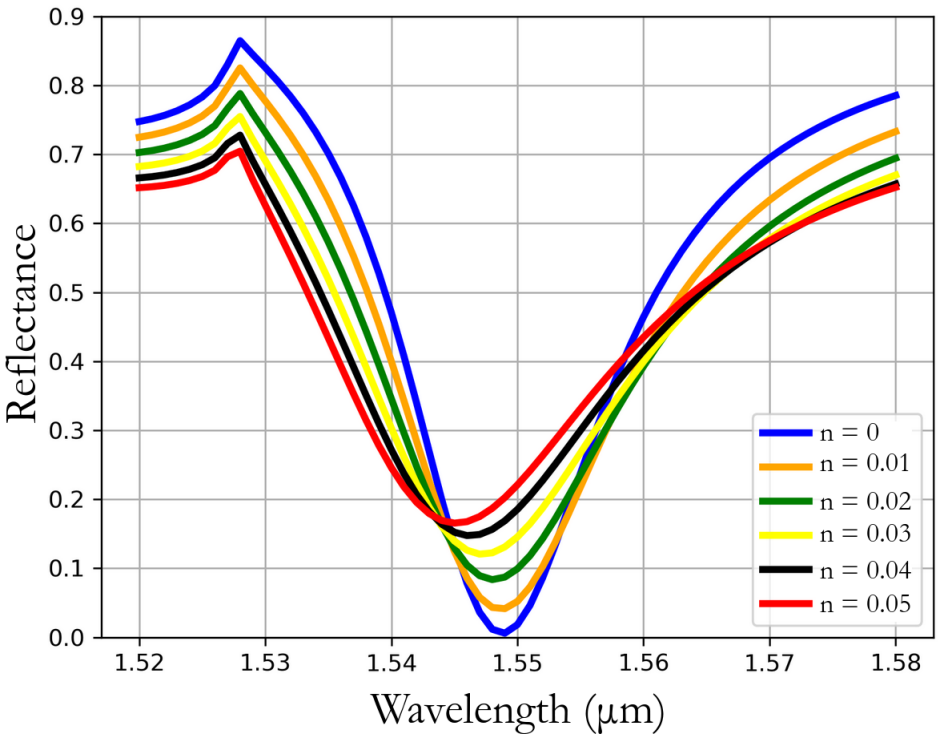

Figure 4.10: Effect of gas presence on Nb grating's resonance curve with rigid substrate for different concentrations n.

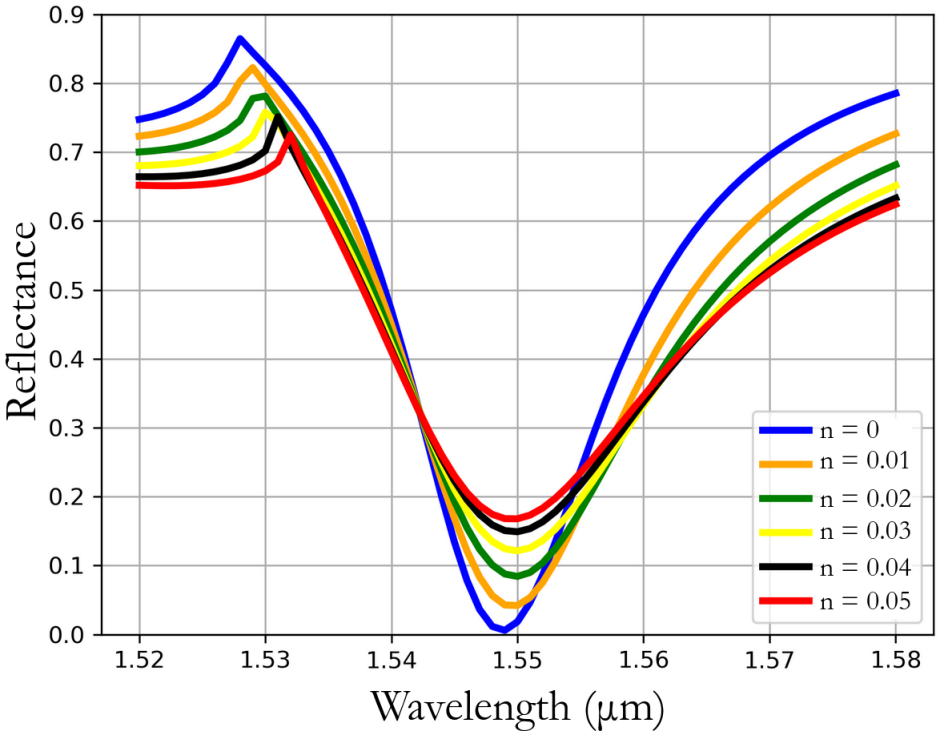

Figure 4.11: Effect of gas presence on Nb grating's resonance curve with flexible substrate for different concentrations n.

4.4.2 Wavelength Modulation Techniques

FFT-based detection

In order to achieve higher sensitivities while maintaining the same system architecture, the sensor is analyzed under sinusoidal wavelength modulation of the employed laser source. Under this condition, the laser current is modulated at 1 kHz, resulting in a beam with a similar modulation frequency in wavelength. It is relevant to mention that this modulation frequency can also be object of an optimization study.

For this simulation, a 1 mW optical power beam is used. The detection subsystem consists of a Transimpedance Amplifier (TIA) circuit, incorporating a photodetector with a responsivity of 0.9 A/W, with its current signal mapped to a 0V–5V range. Further calculations proceed with a Discrete Fourier Transform (DFT) implemented using the radix-2 Cooley-Tukey algorithm. Defining the DFT as

$$A_k = \sum_{n=0}^{N-1} a_n exp(-\frac{2\pi j}{N} nk) \tag{4.31}$$

with k being an integer between 0 and $N-1$, the fast algorithm consists in calculating separately the even and odd indexed inputs a_{2n} and a_{2n+1} and combining these results to produce the DFT of the whole sequence. Separating the even and odd sums,

$$A_k = \sum_{n=0}^{N/2-1} a_{2n} exp(-\frac{2\pi j}{N}(2n)k) + \sum_{n=0}^{N/2-1} a_{2n+1} exp(-\frac{2\pi j}{N}(2n+1)k) \tag{4.32}$$

which can be rewritten as

$$A_k = E_k + exp(-\frac{2\pi j}{N}k)O_k, \tag{4.33}$$

with

$$E_k = \sum_{n=0}^{N/2-1} a_{2n} exp(-\frac{2\pi j}{N/2} nk) \tag{4.34}$$

and

$$O_k = \sum_{n=0}^{N/2-1} a_{2n+1} exp(-\frac{2\pi j}{N/2} nk). \tag{4.35}$$

That means that the transform A_k previously calculated for $0 \leq k \leq N-1$ is now described as two transforms for $0 \leq k \leq N/2-1$. Employing the periodicity of the complex exponential function one can write

$$A_{k+N/2} = E_k - exp(-\frac{2\pi j}{N}k)O_k. \tag{4.36}$$

With Eqs. 4.33 and 4.36, it is possible to calculate, recursively, the desired transform of the signal. It is important to mention that the laser is tuned to have its central wavelength at the point of maximum sensitivity of the curve for $n = 0$,

this results in a signal with a weak second harmonic and the detection is focused on the first harmonic of the reflection signal.

The results for Pd and Nb are presented in Fig 4.12 and 4.13, respectively. The sign of the signal derivative can vary depending on the substrate nature since the shifting of the resonance is highly affected by it.

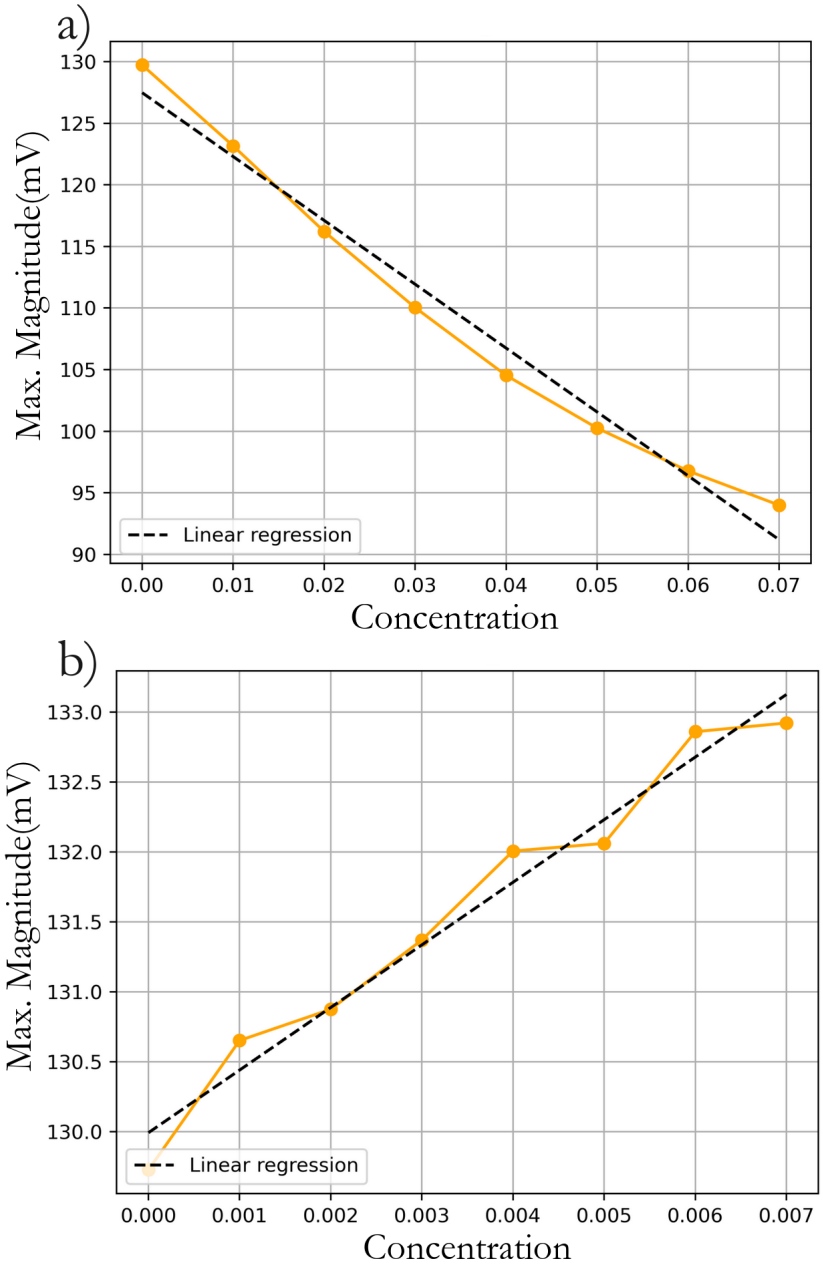

Figure 4.12: Result for maximum magnitude of the FFT for both cases of a) rigid and b) flexible substrate in Pd grating for different concentrations n

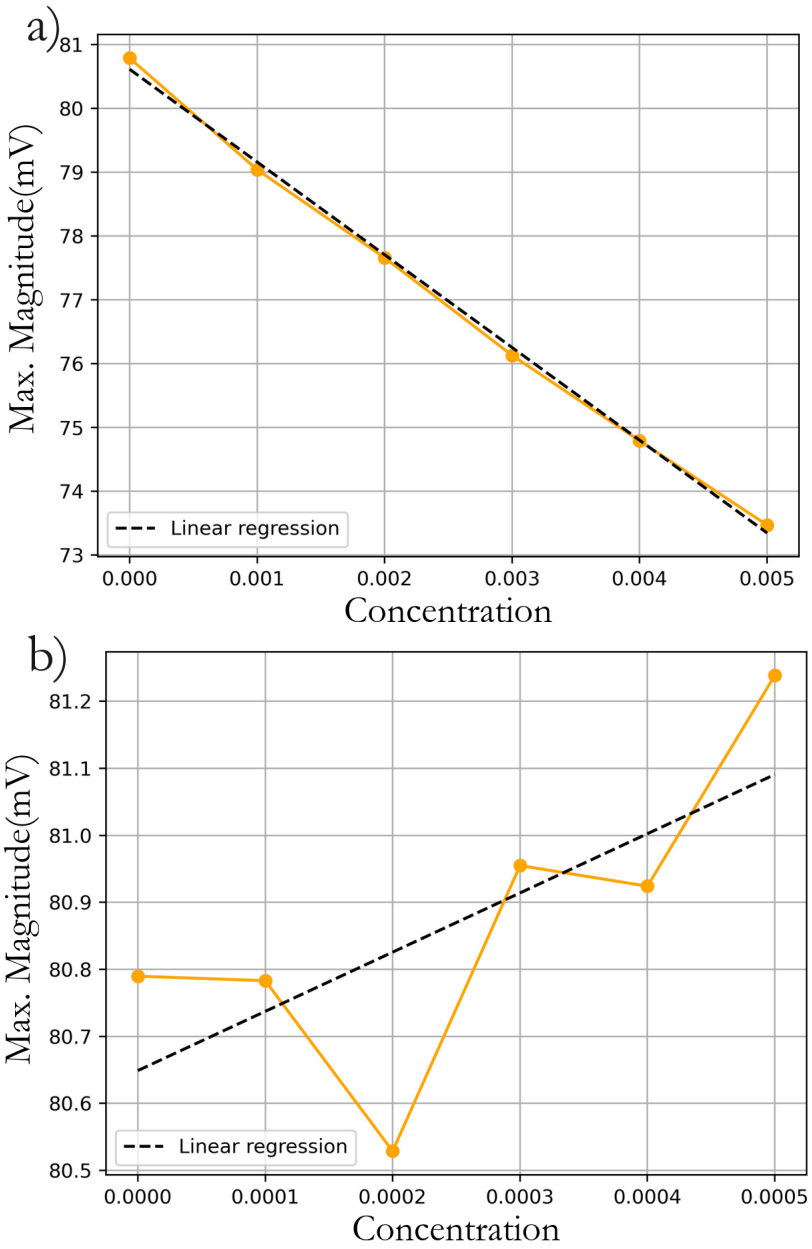

Figure 4.13: Result for maximum magnitude of the FFT for both cases of a) rigid and b) flexible substrate in Nb grating for different concentrations n

Since the modulated incident beam is expected to enhance sensitivity, the investigated concentration range is reduced by one order of magnitude compared to the previously used range for the rigid substrate and by two orders for the flexible substrate. The results indicate a significant degree of non-linearity for Pd in both substrate cases. For Nb, the rigid substrate scenario exhibited high linearity, which was not observed for flexible substrates.

To minimize the lowest detectable concentration and explore measurement schemes

with higher linearity, the signals were analyzed using a computationally implemented digital lock-in technique.

Lock-in-based Detection

The lock-in amplifier is an alternative detection scheme that can be implemented for the optical signal under wavelength modulation. This technique is proposed not only due to its well-established success in spectroscopy(Augulis e Zigmantas,2011:Bonati et al.,2022) but also because its digital implementation using embedded electronic devices remains compatible with a portable system architecture.

The digital lock-in amplifier consists in sampling the signal with the use an ADC, mixing it separately with a reference signal produced by a local oscilator and with the same reference signal with a $\pi/2$ phase shift. Both signals are then filtered by a Low Pass Filter (LPF) implemented as an integration based on the rectangle rule. This produces two components of the signal, the in phase and quadrature components, X and Y, respectively. Another two components are obtained from the first two, the magnitude component M, defined as

$$M = \sqrt{X^2 + Y^2}, \tag{4.37}$$

and the phase component Θ, defined as

$$\Theta = arctg^2(Y, X). \tag{4.38}$$

In this case the squared *arctg* function is used in order to obtain a phase signal that covers the four trigonometric quadrants. Fig. 4.14 shows the architecture of the digitally implemented lock-in amplifier.

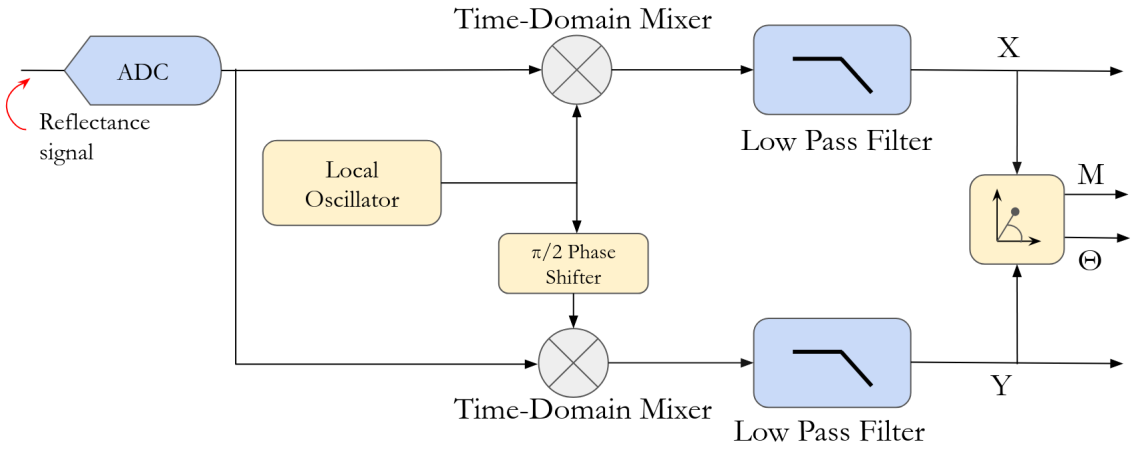

Figure 4.14: Architecture of digital lock-in amplifier implementation.

In this work, lock-in detection is computationally implemented to calculate the magnitude, phase, and both in-phase and quadrature components of the received signal, locked at the modulation frequency.

The results for Pd gratings with rigid and flexible substrates are presented in Figures 4.15 and 4.16, respectively. Similarly, the results for Nb gratings are shown in Figures 4.17 and 4.18. The investigated concentration ranges are reduced by one order of magnitude compared to those analyzed using FFT-based detection.

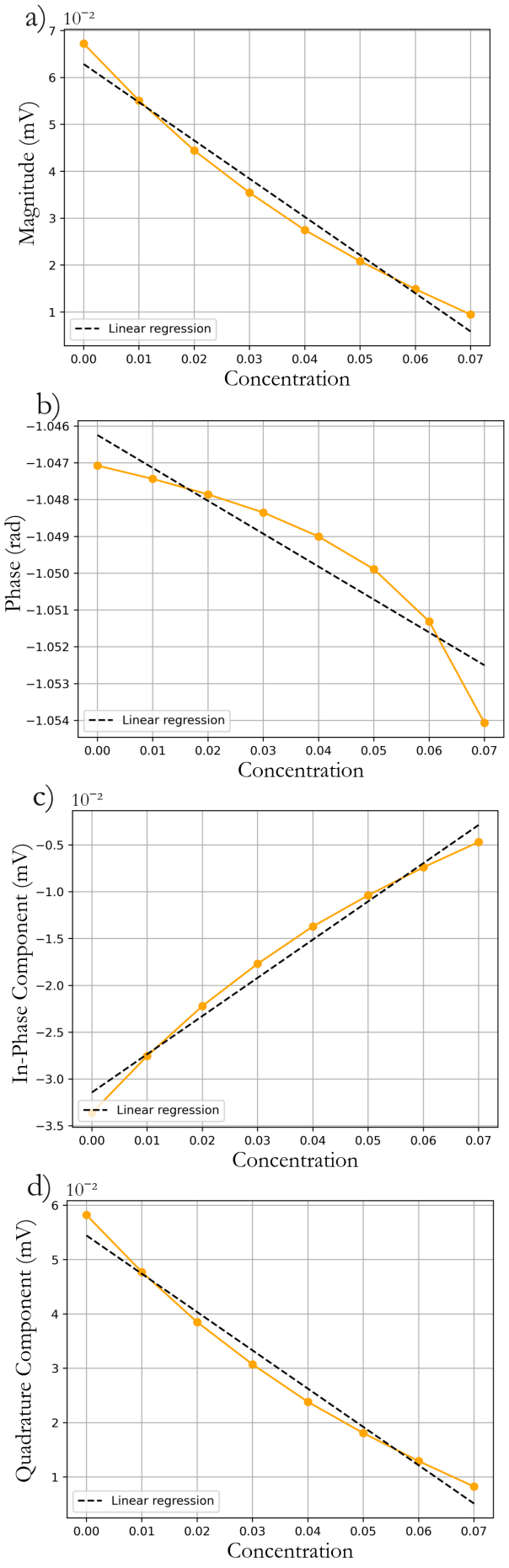

Figure 4.15: Results for lock-in detection in the case of rigid substrate Pd grating. a) Magnitude of lock-in signal, b) Phase, c) In-phase and d) Quadrature components for different concentrations n.

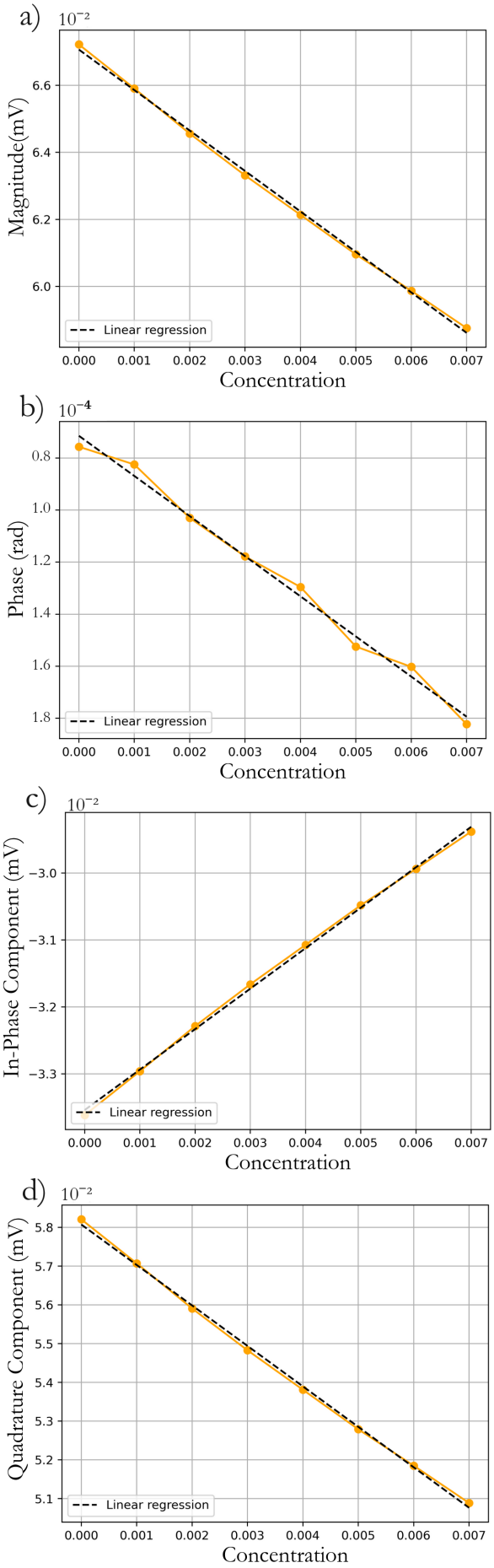

Figure 4.16: Results for lock-in detection in the case of flexible substrate Pd grating. a) Magnitude of lock-in signal, b) Phase, c) In-phase and d) Quadrature components for different concentrations n.

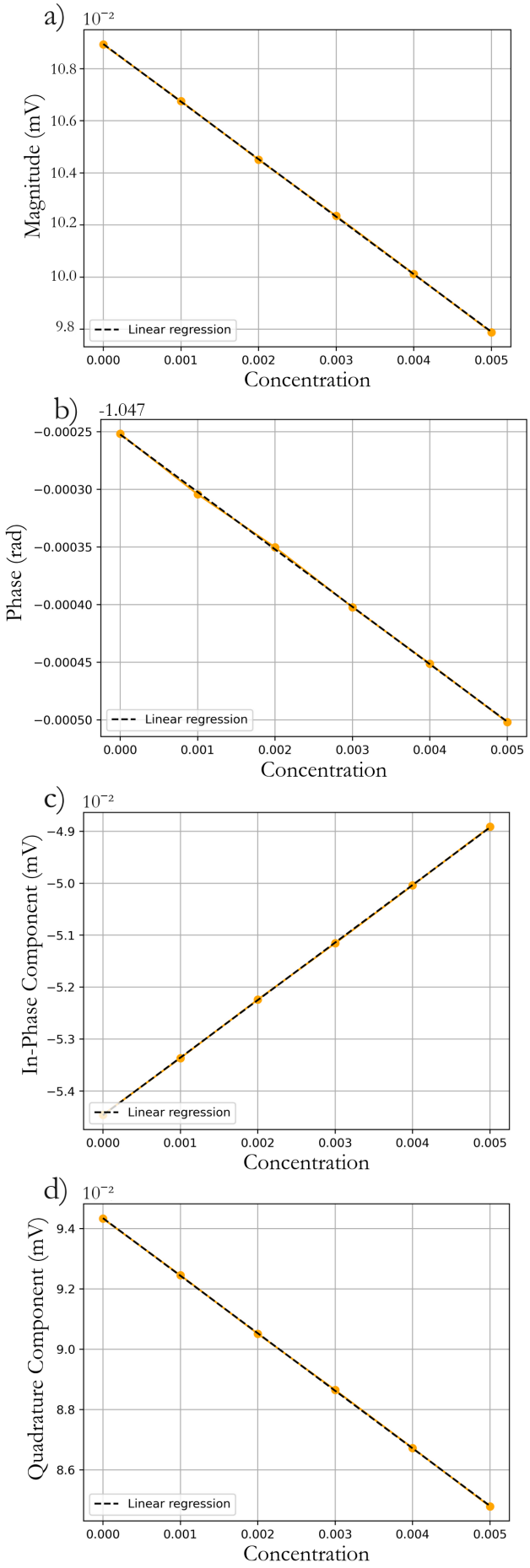

Figure 4.17: Results for lock-in detection in the case of rigid substrate Nb grating. a) Magnitude of lock-in signal, b) Phase, c) In-phase and d) Quadrature components for different concentrations n.

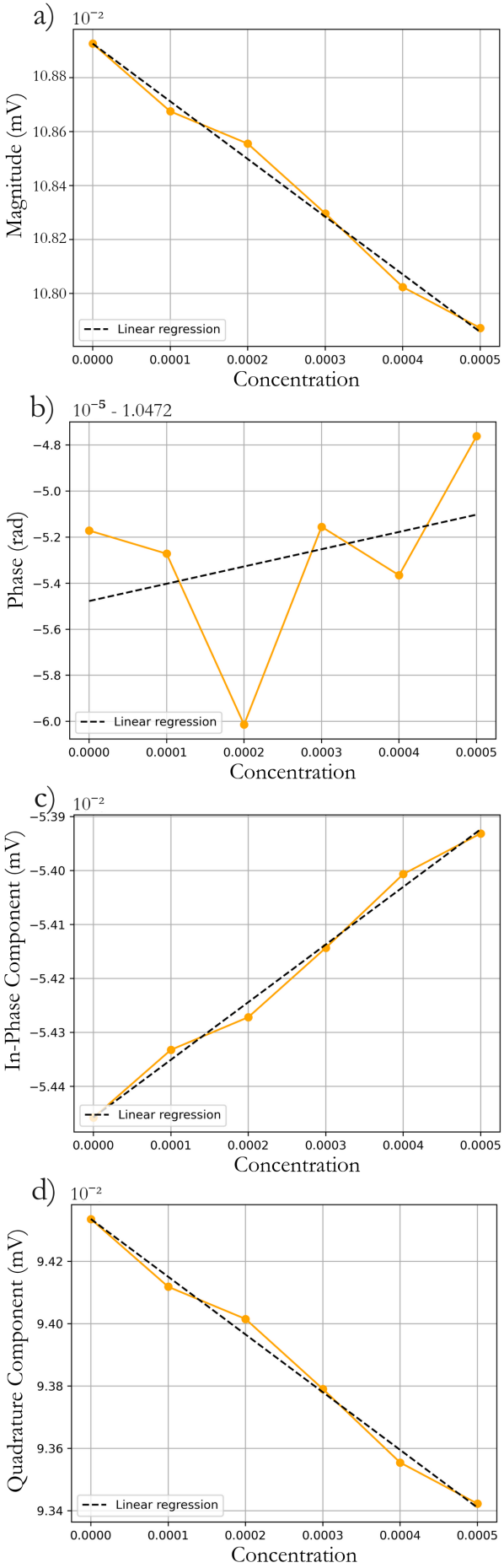

Figure 4.18: Results for lock-in detection in the case of flexbile substrate Nb grating. a) Magnitude of lock-in signal, b) Phase, c) In-phase and d) Quadrature components for different concentrations n.

It is important to make a consideration about the Limit of Detection (LOD) of the proposed scheme to ensure the investigated concentration ranges are above it. To estimate the LOD in terms of minimum detectable reflectance change, one can write

$$LOD = \delta v \cdot \frac{i_{max}}{v_{max} R_e P}, \tag{4.39}$$

where δv is the resolution of the Analog-to-Digital Converter (ADC) used in the TIA, i_{max} is the maximum photocurrent of the photodiode, v_{max} is the maximum voltage readable by the ADC, R_e is the responsivity of the photodiode, and P is the emitted laser power. Considering a 0V–5V range and a 16-bit ADC, we have $\delta v = 0.076$ mV and $v_{max} = 5V$. For $i_{max} = 0.9$ mA, $R_e = 0.9$ A/W, and $P = 1$ mW, the limit of detection (LOD) is calculated as $1.52 \cdot 10^{-5}$.

Numerical simulations confirm that a reflectance change is observed for a concentration variation of $\delta n = 10^{-3}$ in the Pd grating, yielding $\delta R = 3.1 \cdot 10^{-3}$. For the Nb grating, with $\delta n = 10^{-4}$, the corresponding reflectance change is $\delta R = 2.24 \cdot 10^{-5}$. This indicates that all investigated concentration ranges for both structures are above the LOD. Both δR calculations were performed considering incidence at the wavelength of maximum sensitivity.

To facilitate comparisons, it is useful to establish a relation between atomic and volumetric concentrations. For this purpose, the total volume of the hydride can be expressed as

$$V_T = V_m + V_H = N_a^m V_a^m + n N_a^m V_a^H \tag{4.40}$$

with V_m and V_H being the volumes of metal and hydrogen, respectively, N_a^m the number of metal atoms and V_a^m and V_a^H the atomic volumes of the metal and hydrogen. To obtain the volume percent concentration of hydrogen $c(\%)$ one can write

$$c(\%) = 100 \cdot \frac{V_H}{V_T}, \tag{4.41}$$

and considering a spheric geometry for each atom one can obtain

$$c(\%) = \frac{xR_H^3}{R_{Pd}^3 + xR_H^3}. \tag{4.42}$$

Applying the equation above with $R_{Pd} = 137$ pm (Slater, 1964) and $n = 10^{-3}$ one can obtain $c(\%) = 0.67\%$. For Nb one can employ $R_{Nb} = 146$ pm (Slater, 1964) and $n = 10^{-4}$ to obtain $c(\%) = 0.0055\%$. It is important to note that the latter concentration is equivalent to 55 ppm, indicating that this technique employed with the Nb grating could achieve ppm limit of detection.

The saturation of the proposed technique is directly related to the maximum concentration of hydrogen the metal can absorb for a particular temperature and pressure. For ambient temperature and 1 atm pressure, Pd forms the hydride with a concentration of up to $PdH_{0.7}$, for Nb this concentration is around 0.5 (Pryde e Titcomb, 1969). Such values can change according to temperature and pressure, but it requires high pressure (GPa) and high temperature (10^2 °C) to obtain higher concentrations (Wang et al., 2024). Since such temperature and pressure ranges are not likely to be observed in practical sensing scenarios, one should not expect that this factor could significantly affect the saturation of the proposed technique.

Another important environmental factor is humidity and its effect on the grating resonance. The air relative humidity can affect the sensing medium refractive index, however, a grating made of metals such as Nb and Pd is insensitive to refractive index variations due to larger resonance widths caused by lower imaginary refractive indexes compared to standard plasmonic materials such as gold and silver. A humidity-related effect that would provide a significant change to the instrument's response is the dew point. In that case, the formation of droplets of water on the grating surface would require a separate analysis to investigate its effect on the grating resonance.

4.4.3 Sensor Response Time

The sensor response time is calculated using Eq. 4.11 for the previously considered concentration ranges. The values for the diffusion coefficient for Pd and Nb are obtained from (Katsuta et al., 1979) and (Cantelli et al., 1969), respectively. The results are presented in Fig. 4.19.

It is important to mention that this response time calculation is a "pure" approach, in which the goal is to validate the choice of material and spectral range to be employed in order to achieve better response times but the characteristics of the sensing medium is also very important for the response time since the model considers a fixed concentration on the surface, but in a practical situation the time of gas injection and geometry of the sensing medium is of great importance. It is also important to mention that the response time of the photodiodes also add up to the total response time of the measuring system.

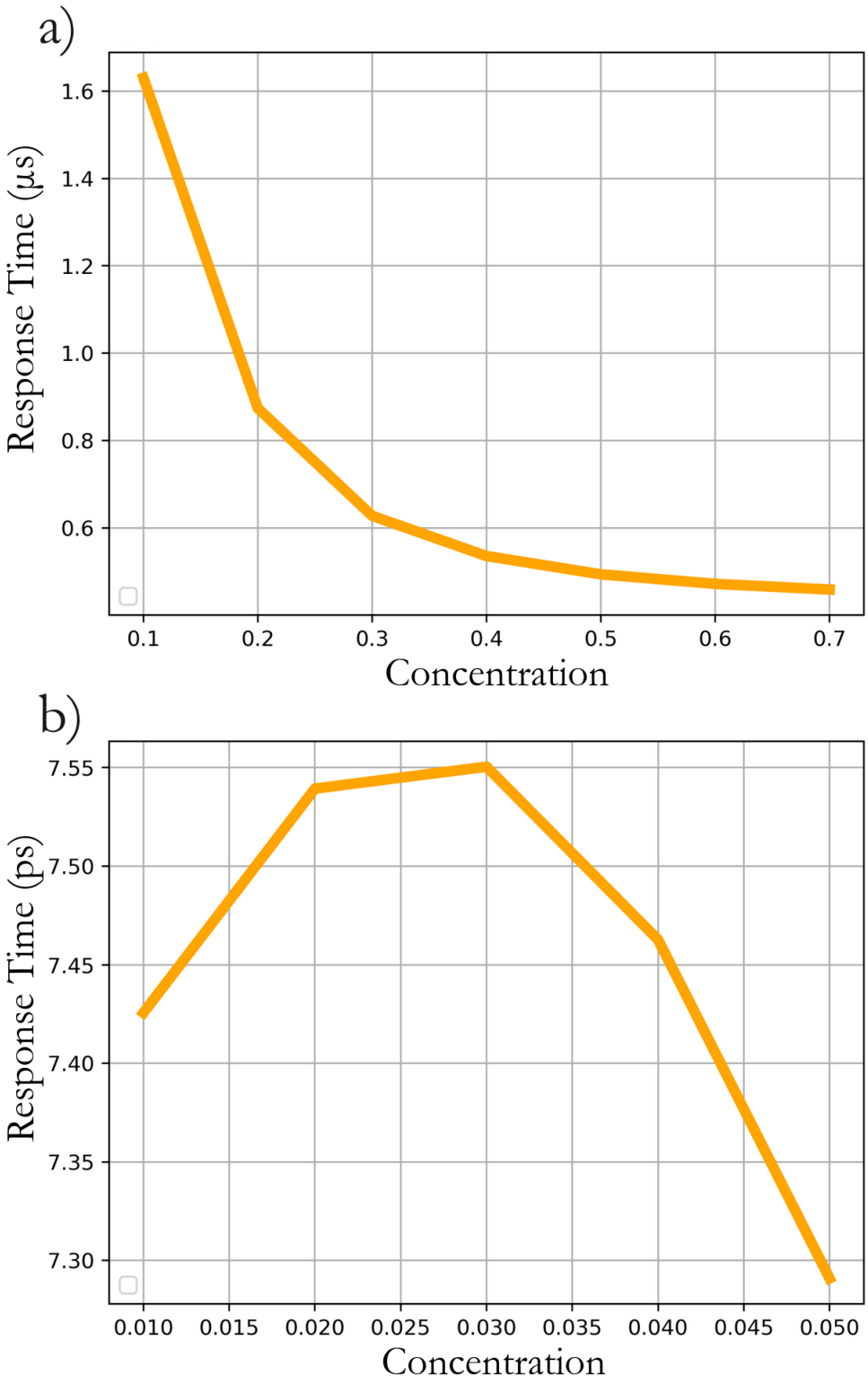

Figure 4.19: Results for response time. a) Pd b) Nb for different concentrations n.

Chapter 5

Oxide/Metal/Hydride Plasmonic Devices for Hydrogen Sensors Based on D-shaped Optical Fibers

This chapter brings results about the design of Oxide/Metal/Hydride planar structures for D-shaped single mode fibers (SMF) with the aim of proposing hydrogen sensitive devices. The text discusses, firstly, the Kretschamnn configuration in D-shaped optical fibers, it details the construction of a numerical model associated with an eignevalue solver for modal analysis, the optimization of the structure as wells as computational experiments concerning the contact of the device with a hydrogen gas concentration.

5.1 Kretschmann configuration in D-shaped optical fibers

Until now, this work has dealt with the SPR effect in diffraction grating, but its observation on planar surfaces is the most commonly employed type of structure on which sensors are based. This configuration refers, structurally, to a metal layer, with typical thickness on the order of tens of nanometers, between a dielectric and a

sensing medium that could be gaseous or liquid. The SPR effect was first observed in this configuration with a prism-based coupling scheme (Kretschmann,1971), but can also be observed in different optical fiber structures such as the D-shaped one.

This type of fiber structure employ a polishing procedure to obtain D-shaped sectional profile, leaving the core of the fiber closer to the external medium. This type of fiber has found a great number of applications in the field of sensors and instrumentation since it is very sensitive to optical and structural variations on the external medium. Fig. 5.1 provides a schematic for a general D-shaped fiber with d_h, d_m and d_o being the hydride, metal and oxide thicknesses, respectively. Fig. 5.2 shows a three-dimensional representation of the proposed device.

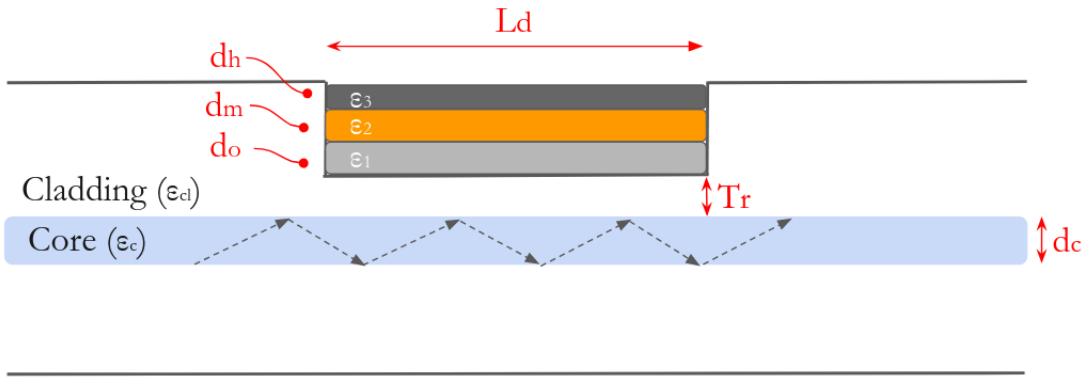

Figure 5.1: Longitudinal scheme for D-shaped optical fiber with a multilayer structure.

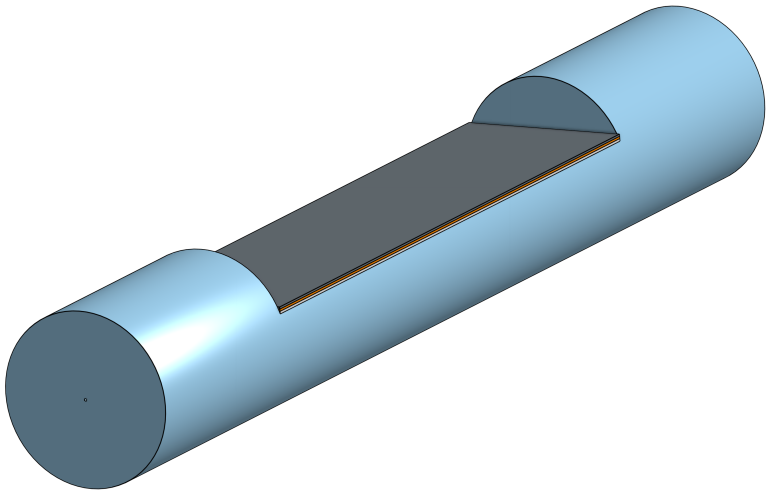

Figure 5.2: Three-dimensional scheme of the proposed sensor structure.

In this work, we introduce the Oxide/Metal/Hydride structure, in which a particular oxide of choice is employed to tune the plasmonic resonance. This is achieved by the refractive index difference between the clad and the oxide on the D region, enabling the sensor to operate in a more practical wavelength and to tune the point of maximum sensitivity to the central wavelength propagating on the fiber's core. The metal layer permits the enhancement of the device's sensitivity by employing materials with better plasmonic properties such as Au, Ag, Cu, or Al even considering that such metals alone would not lead to a transducer specific to hydrogen. The hydride layer is composed of a hydride-forming metal such as Pd and Nb which would benefit from hydrogen specificity and its optical and structural variations could be employed to enhance sensitivity. It is important to mention that the OMH structure would provide better transducing performances than the Oxide/Hydride (OH) structure considering the fact that planar structures in a wavelength-resolved measurement lead to much wider resonance widths compared to the inclusion of Au for example, that means the OH structure would benefit from specificity but would result in lower sensitivity compared to the OHM structure.

Since the sensing methodology consists of the interaction between the light that escapes the core to the clad with the external medium, it involves the out-coupling of the beam propagating on the core to the clad and external medium and then coupling again on the core. That means that, from a practical perspective, the sensor should be interrogated in terms of its transmission. For this goal, one can employ Fresnel relations to the problem.

First, one should consider the number of reflections on the D region, shown in Fig. 5.1. One can readily state that the number of reflections δ can be written as

$$\delta = \frac{L_d}{d_c} tan(\theta). \tag{5.1}$$

with θ being the incident angle. Considering that along the D-shaped section there are δ reflections by the multilayer structure deposited on the fiber, the transmission of the device is written as

$$T = R_m^{\delta} \tag{5.2}$$

with R_m denoting the Transversal Electric (TE) Fresnel reflection of the m layer structure and given by

$$R_{m-1} = \left| \frac{\Gamma_{(m-1),m} + \Gamma_m exp(-2jk_m d)}{1 + \Gamma_{(m-1),m}\Gamma_m exp(-2jk_m d)} \right|^2, \tag{5.3}$$

with reflection coefficients given by

$$\Gamma_{m-1,m} = \frac{\epsilon_m k_{m-1} - \epsilon_{m-1} k_m}{\epsilon_m k_1 + \epsilon_1 k_m}, \tag{5.4}$$

and

$$k_m = k_0 \sqrt{\epsilon_m - \epsilon_1 (sen\theta)^2}. \tag{5.5}$$

Although the Fresnel-based description provides a reasonable explanation of the observation of the effect this model does not provide an accurate description of the fiber response since it ignores the cylindrical to D-shaped to cylindrical geometry changes and therefore it cannot account for the losses due to the polished area. This indicates that conducting optimization based on such a model would be inadequate since there are behaviors that are important to the sensor performance that are not taken into account. One good alternative to this model would be the construction of a numerical model based on the Finite Element Method (FEM) to describe precisely the geometry of the device and obtain computational results that are close to the experimental situation. In the next section, such a model is detailed.

5.2 Numerical modeling of OMH structures over D-shaped optical fiber

To obtain the response of a D-shaped SMF with a multilayer structure over the polished region it is possible to implement a bi-dimensional model, as seen in Fig. 5.3. For this calculation, the COMSOL *ewfd* interface is also employed to search for possible modes that, for the desired geometry, correspond to a propagating wave according to the wave equation.

The mode analysis, consists in searching for a particular number of modes given by the user, based on an initial guess. The process then inputs a mode frequency into the Helmholtz equation for electric fields and then searches for a solution in the form of a wave traveling in the D-shaped fiber. That means two numerical routines are employed together, the FEM for solving the wave equation and an eigenvalue solver.

The eigenvalue algorithm used was the Arnoldi iteration (Arnoldi,1951). This algorithm finds approximations to eigenvalues of a matrix A by means of the construction of an orthonormal basis on the Krylov subspace, defined as the span of an arbitrary vector under v powers of A. The search starts with an arbitrary vector $\vec{q}$ then a power iteration takes place to calculate A^0q, Aq, A^2q, ... , to form the matrix

$$K_v = (b, Aq, \cdots, A^{v-1}b). \tag{5.6}$$

Since the matrix A is not necessarily orthogonal, one can employ the Gram-Schmidit orthogonalization process,

$$u_v = K_v - \sum_{j=1}^{v-1} proj_{u_j} K_v \tag{5.7}$$

to obtain an orthogonal basis of the Krylov subspace. This basis is then an approximation of the eigenvectors associated with the v largest eigenvalues, based on their absolute value, with $A^{v-1}b$ being the approximation of the dominant eigen-

vector.

The library employed is ARPACK which implements Implicitly Restarted Arnoldi Iteration (IRAI), which is a variant of the technique to improve convergence time developed in FORTRAN 77(Lehoucq et al.,1998).

Employing the process of inputting a mode into the Helmholtz equation and searching for solutions associated with the dominant eigenvalues, one can numerically obtain the modes associated with both TE and TM polarization states that propagate on the waveguide. These obtained modes can be described as the effective refractive index n_{ef} by which the beam propagating on the core of the fiber is subjected. With these values, one can calculate the transmittance of the device according to

$$T = exp[2Im(n_{ef})k_o L_d] \tag{5.8}$$

and with this procedure one can model the device response in a more realistic manner.

To explicit practical matters of how the model is built one should start with the model of the geometry of the device and associating the materials with each region. The geometry is defined as the transverse section of the fiber, in which the hydride layer is implemented by the use of the Transition Boundary Condition. This feature represents a layer with a particular thickness and associated refractive index that imposes a discontinuity in the tangential electric field and can be employed for thin layers, such as the case of Pd and Nb metals in this device. Fig. 5.3 shows the scheme for the geometry implemented with reduced cladding diameter for better visibility. Then a triangular mesh with a maximum and minimum element size of 5 μm and 0.155 μm, respectively, and a maximum element growth rate of 1.3 and curvature factor of 0.3 is built. The modeled geometry and the mesh can be seen in Fig. 5.4

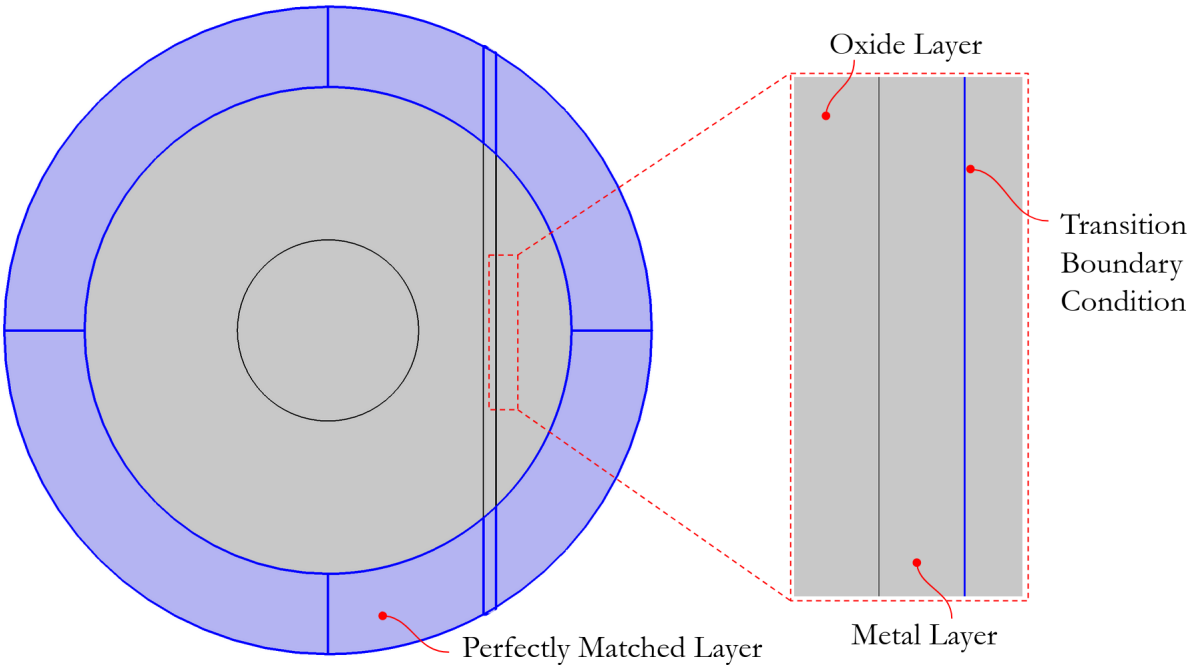

Figure 5.3: Geometry of modeled device and definition of domains.

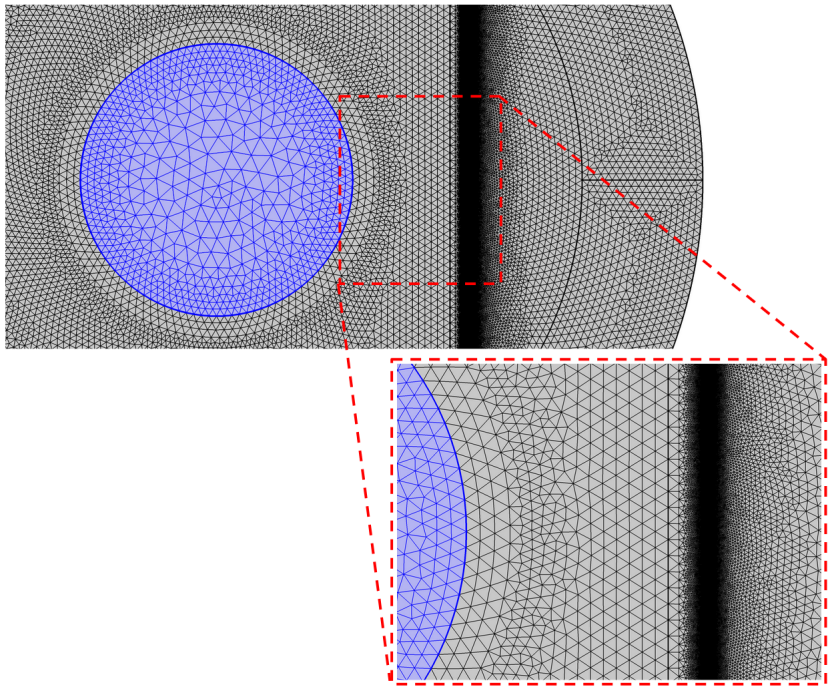

Figure 5.4: Employed mesh for FEM simulations.

An electric field

$$E_0(x, y, z) = E_0(x, y)exp(-jk_z z), \tag{5.9}$$

is emitted to propagate along the fiber with k_z being the wavevector associated

with the propagation along the fiber core and $E_0(x, y)$ an initial value for the field given by the user.

With this numerical model and Eq. 5.8, one can obtain reliable results for the structure Transmittance and therefore, conduct computational experiments and device optimization.

5.3 Optimization of Oxide/Metal/Hydride Structures

With the aid of the numerical model, a few computational experiments were conducted to observe the effect of the oxide, metal and hydride layer thicknesses. The first analysis is made for an oxide/metal/hydride structure implemented with TiO_2, Au and Pd with a fixed value for the oxide thickness d_o of 550 nm and hydride $d_h = 5$ nm. The oxide thickness was obtained after a few computations to shift the Au plasmonic resonance expected to be observed at the visible spectrum for the case of $d_o \to 0$ to the infrared, so the sensor can be interrogated on the low-loss spectral region of the fiber. This thickness value will be subject to optimization later on. The transmittance curve of the structure used as an initial guess is seen in Fig 5.5.

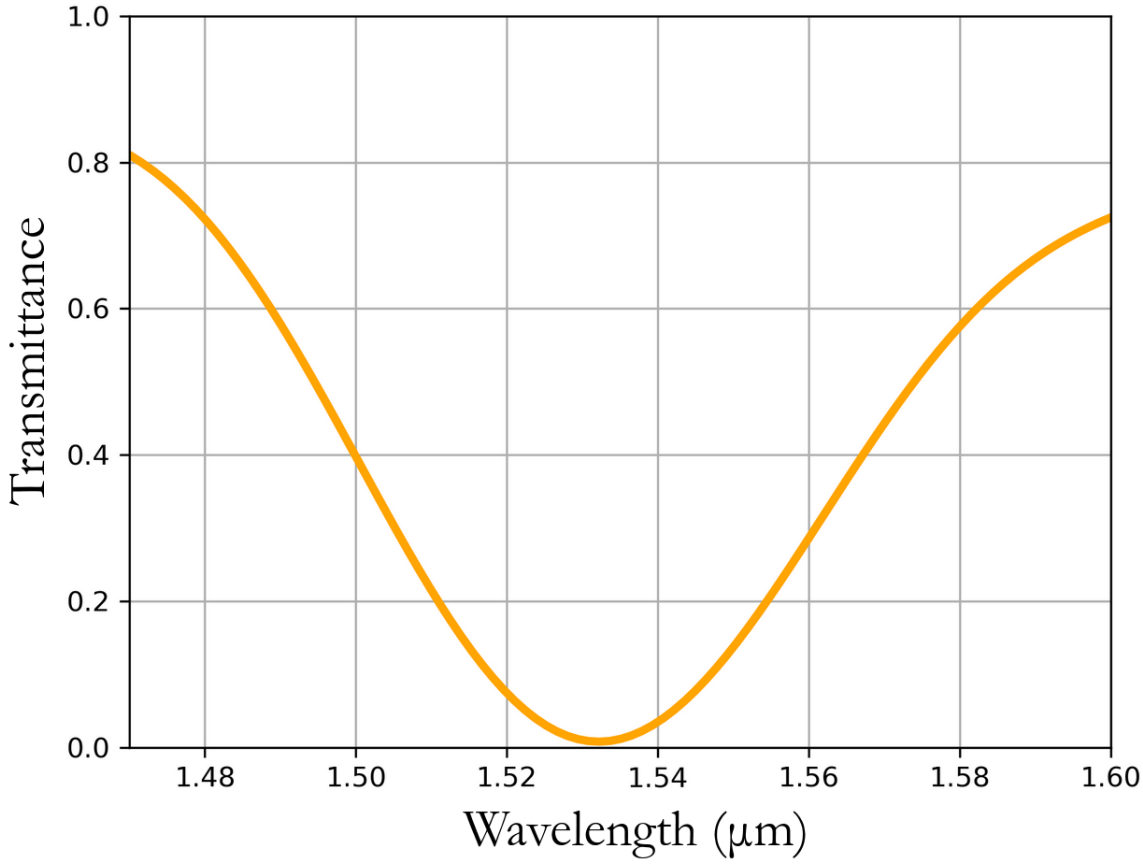

Figure 5.5: Transmittance curve for the structure used as an initial guess with $d_o = 550$ nm, $d_m = 10$ nm and $d_h = 5$ nm.

With the mentioned d_o and d_h values, a simulation was conducted with a sweep on the metal thickness. For this, a range of metal thickness d_m from 10 nm to 2 nm was investigated with a 2 nm step. Fig. 5.6 shows the results for the effect of d_m on the device sensitivity defined by

$$S(\lambda) = \left| \frac{\partial T}{\partial \lambda} \right| \tag{5.10}$$

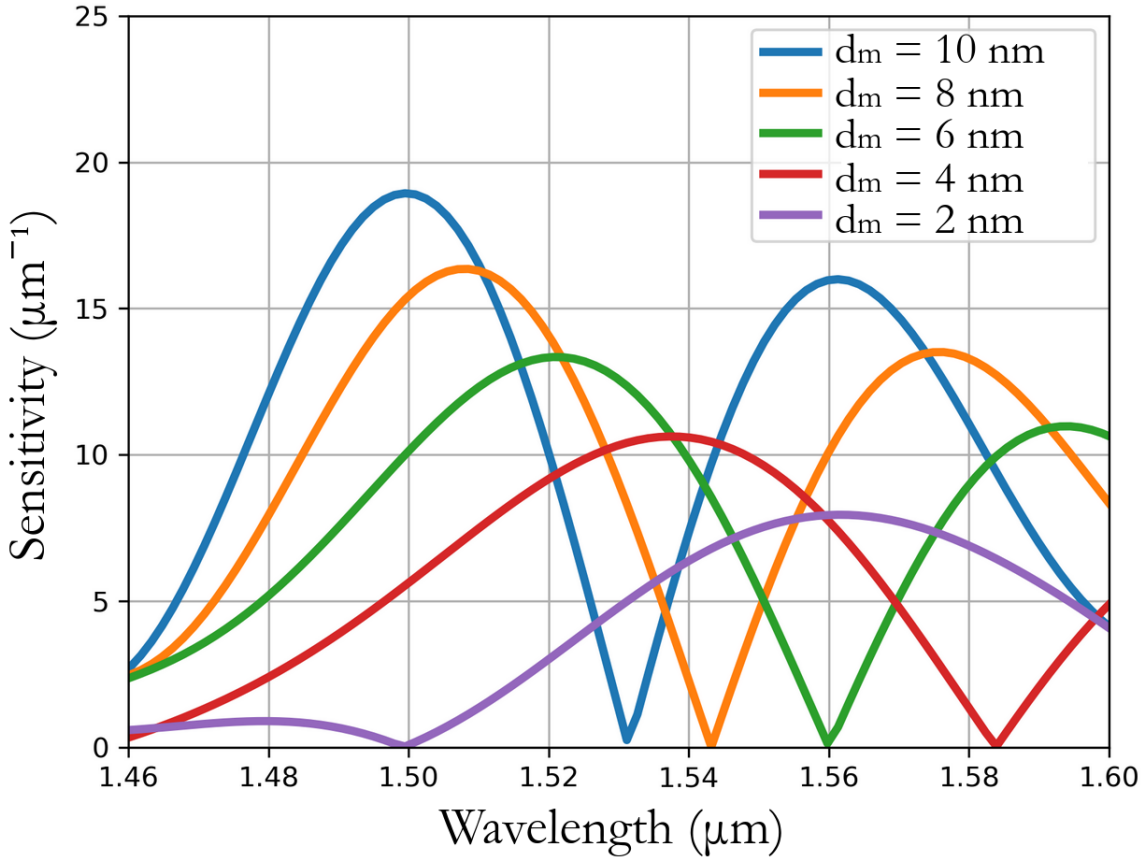

Figure 5.6: Effect of metal layer thickness variation on device sensitivity.

It is shown that higher sensitivities are observed for increasing values of d_m. In this case, the ideal situation would be employing a film thickness as thick as possible, without saturation of the resonance, that is,a flattening of the resonance dip. There are, of course, practical limitations related to film thickness. There could be limitations of the fabrication method to be employed or minimum and maximum thickness requirements for the mechanical stability of the device. In this work, the minimum/maximum metal layer thickness is a parameter inputted into the design procedure.

With $d_m = 10$ nm, a similar computational experiment was conducted with a sweep on the oxide thickness. The values investigated were between 550 nm and 580 nm with a 10 nm step. It is clear that a thicker oxide layer results in a resonance shift towards the infrared, as expected since this layer is employed to shift the Au resonance from the visible to around 1550 nm. Fig. 5.7 also shows that the oxide layer has an effect on the curve sensitivity, indicating that higher values of d_o result

in less sensitive structures, even though its influence is not as strong as the metal layer d_m.

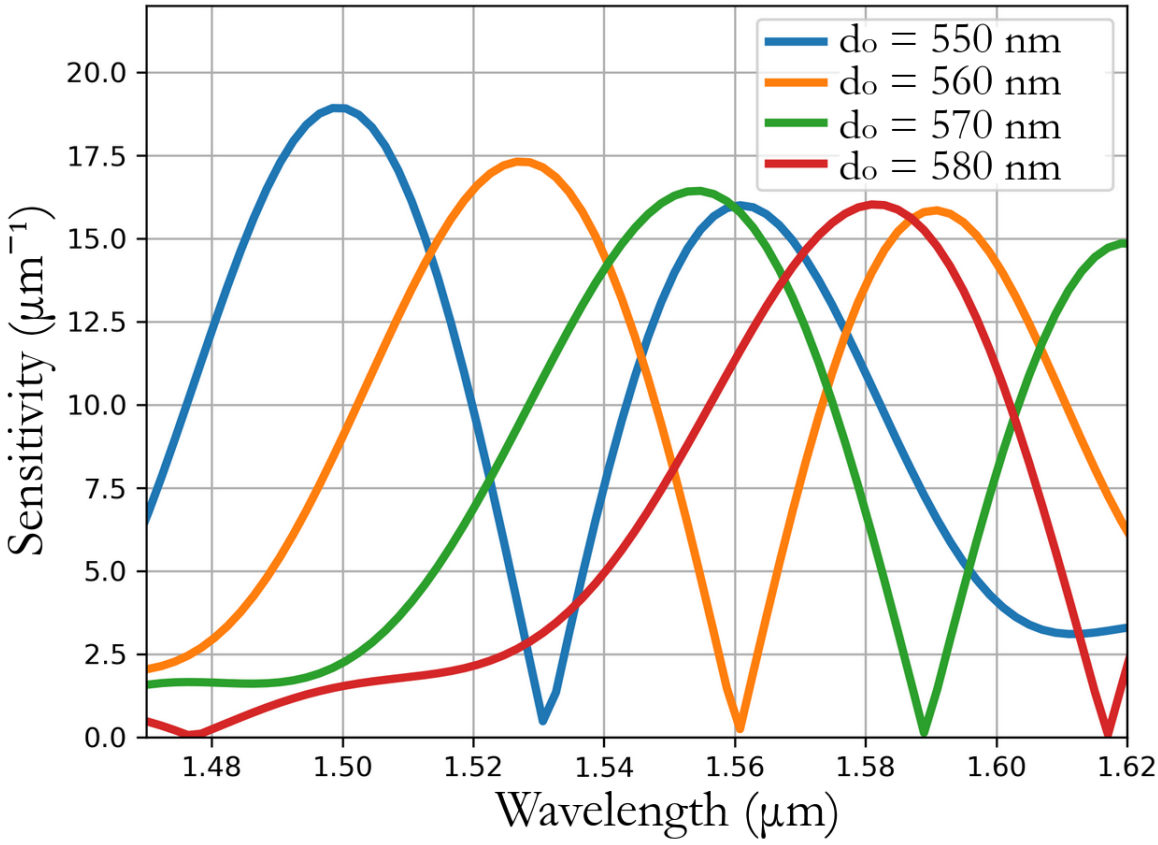

Figure 5.7: Effect of oxide layer thickness variation on device sensitivity.

The last computational experiment intended to explore the influence of each layer was conducted to inquire about the effect of the hydride forming layer, in our case, realized in Pd. Since the metal has a higher real refractive index than the air, which was the medium in contact with the Oxide/Metal structures previously explored, it is expected that its presence would enlarge the resonance of the underlying OM structure. Considering such an argument, lower values of Pd thickness d_h were investigated and its effect on the resonance and sensitivity of the device were analyzed. Fig. 5.8 shows the results for $d_m = 10$ nm and $d_o = 550$ nm.

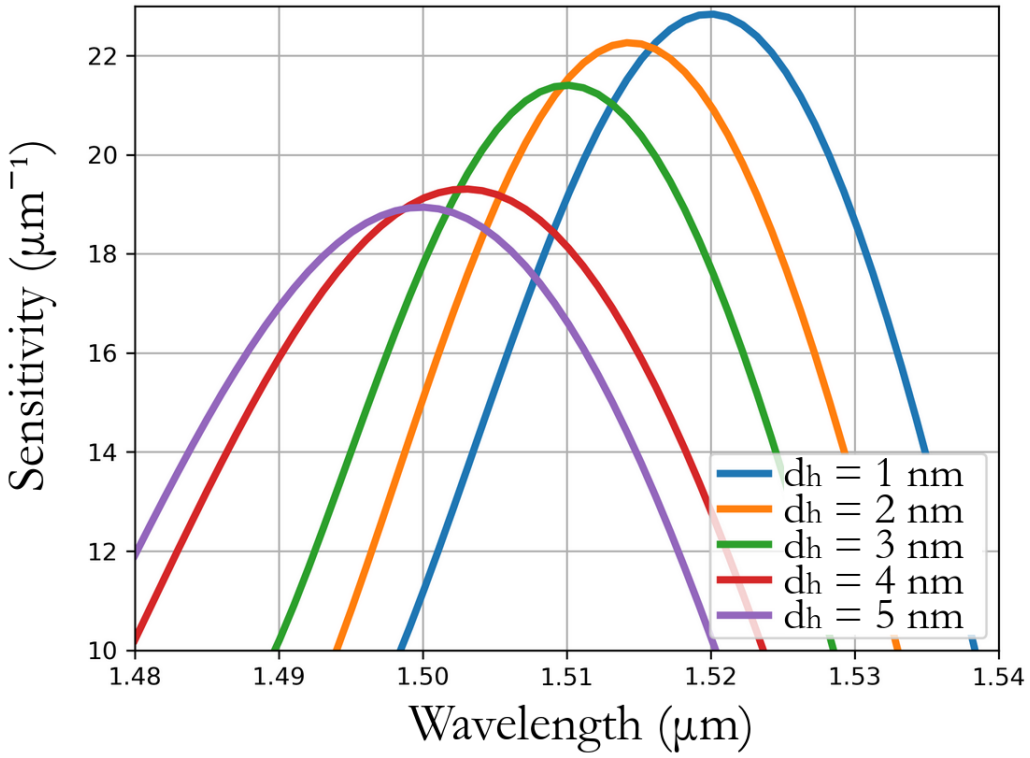

Figure 5.8: Effect of hydride layer thickness variation on device sensitivity.

It is evident that a thinner layer of Pd results in higher sensitivities, it is also clear that the hydride-forming layer also results in a resonance shift. It is concluded that all three layers have an effect on both resonance position on the spectrum and on the device sensitivity, ideally, the suggested optimization routine should take into consideration the maximum sensitivity obtainable at a particular wavelength of incidence.

Another effect that should be considered while optimizing an OMH structure, is the possible saturation of the resonance. Such saturation consists in the case of an arbitrarily wide spectral region in which the transmission of the device shows no variation, causing a flattening of the resonance dip. This is a design feature related to the experimental method and architecture that would be used to interrogate the fiber. Considering this, the following parameter is inputted by the user to avoid generating a design in which there would be a resonance saturation for a particular experimental setup

$$p_{sat} = \frac{\delta T}{\delta \lambda}. \tag{5.11}$$

This parameter consists of the minimum average sensitivity calculated for two points, one of them being the point of lowest transmission, that is, the resonance condition, and another one chosen by the designer. It is not recommended to choose two points over a wide spectral range since the saturation is indicated by an average value between them. In this work, it is considered that for a $\delta\lambda = 1$ nm the system can detect an intensity change $\delta T = 0.0001$, leading to a saturation parameter $p_{sat} = 0.0001\ nm^{-1}$.

To ensure that the designed device has its peak of sensitivity on the desired wavelength, the optimization of the oxide layer is given in terms of resonance tuning and not aiming for higher sensitivities, since it is shown from the computational experiment that this layer has a greater effect on the resonance position on the spectrum than on sensitivity. For this, the d_o parameter is optimized to minimize the function $g(\lambda) = |\lambda_{max} - \lambda_c|$, with λ_{max} being the wavelength of maximum sensitivity for a particular structure and λ_c being the desired wavelength of maximum sensitivity for the final structure. On the other hand, the metal and hydride layers are optimized for enhancing the device sensitivity, which means the parameters d_m and d_h are optimized to maximize the function $S(\lambda) = abs(\partial T/\partial \lambda)$.

To assess the fact that all three thickness parameters have an influence on resonance position and sensitivity, a recursive optimization routine is implemented. The previous analysis indicated that thinner layers of Pd would provide better sensitivity, which means the minimum craftable thickness could be employed. However, one could take into account that the thickness variation due to hydrogen absorbance is dependent on the original thickness of the film, with thicker films permitting a higher variation which could, potentially, impact the final sensitivity. If higher values of d_h are chosen, one should employ higher values of d_m to achieve similar $S(\lambda)$ sensitivity to the case with thinner Pd layers. This increase in the metal thickness is limited to the penetration depth of the light into the structure, since if the light does not

penetrate enough to interact with the Pd layer, the hydrogen specificity is lost. The optical power penetration depth for Au is given by

$$\phi_{Au} = \frac{1}{2k_0 Im(\eta)} = 11,48nm. \tag{5.12}$$

To choose a maximum value of the metal layer thickness to use as a constraint on the optimization routine with a safety margin, 90% of ϕ_{Au} is used. It is preferable to employ thinner values of Pd since the thickness variation occurs on the Pd layer with nanometric dimensions and this mechanism is not expected to provide a great contribution to the final sensitivity of the device. This is later explored in this chapter.

Then, the oxide layer is optimized to tune the resonance to the desired wavelength. The process then continues to optimize the metal layer, also considering the saturation and thickness criteria. Following this, the oxide layer is again optimized. This procedure is repeated until the final structure obeys the tuning stop criteria λ_{er}, which is the accepted error between the desired wavelength of maximum sensitivity and the wavelength of maximum sensitivity of the final device, and the saturation criteria considering final values obtained for each layer thickness. This procedure is highlighted in Algorithm 3.

The final structure obtained applying this optimization strategy was $d_o = 515.5$ nm, $d_m = 2$ nm and $d_h = 1$ nm. Fig 5.9 shows the transmittance curve and its sensitivity, ensuring that the final device obeys both the tuning and saturation criteria.

Algorithm 3 Pseudocode for OMH structure over D-shaped fiber optimization.

input Initial Guesses $\leftarrow \{d_h^0, d_m^0, d_o^0\}$
input $\{d_h^{min}, d_m^{min}, d_o^{min}\}$
$\{n, m, l\} \leftarrow \{0, 0, 0\}$;
while $abs[T(d_h^{n+1}, d_m^{n+1}, d_o^{n+1}, \lambda_{rps}) - T(d_h^{n+1}, d_m^{n+1}, d_o^{n+1}, \lambda_{rps-1})] \geq p_{sat}$ & $g(d_h^{n+1}, d_m^{n+1}, d_o^{n+1}, \lambda) \geq \lambda_{er}$ **do**
  while $abs[T(d_r^{n+1}, \lambda_{rps}) - T(d_r^{n+1}, \lambda_{rps-1})] \geq p_{sat}$ & $d_h^{n+1} \geq d_h^{min}$ **do**
    if $n == 0$ **then**
      $GradientOptimizationStep(S(\lambda), d_m^0)$
      n++;
    else
      $GradientOptimizationStep(S(\lambda), d_m^n)$;
      n++;
    end if
  end while
  while $abs[\lambda_{max} - \lambda_c] \geq \lambda_{er}$ **do**
    if $m == 0$ **then**
      $GradientOptimizationStep(error(d_0), d_o^0)$
      m++;
    else
      $GradientOptimizationStep(error(d_0), d_o^{n+1})$
      m++;
    end if
  end while
  while $abs[T(d_m^{n+1}, \lambda_{rps}) - T(d_m^{n+1}, \lambda_{rps-1})] \geq p_{sat}$ & $d_m^{n+1} \geq d_m^{min}$ **do**
    if $l == 0$ **then**
      $GradientOptimizationStep(S(\lambda), d_m^0)$
      l++;
    else
      $GradientOptimizationStep(S(\lambda), d_m^{n+1})$
      l++;
    end if
  end while
  while $abs[\lambda_{max} - \lambda_c] \geq \lambda_{er}$ **do**
    $GradientOptimizationStep(error(d_0), d_o^{n+1})$
    m++;
  end while
end while
Generate plots;

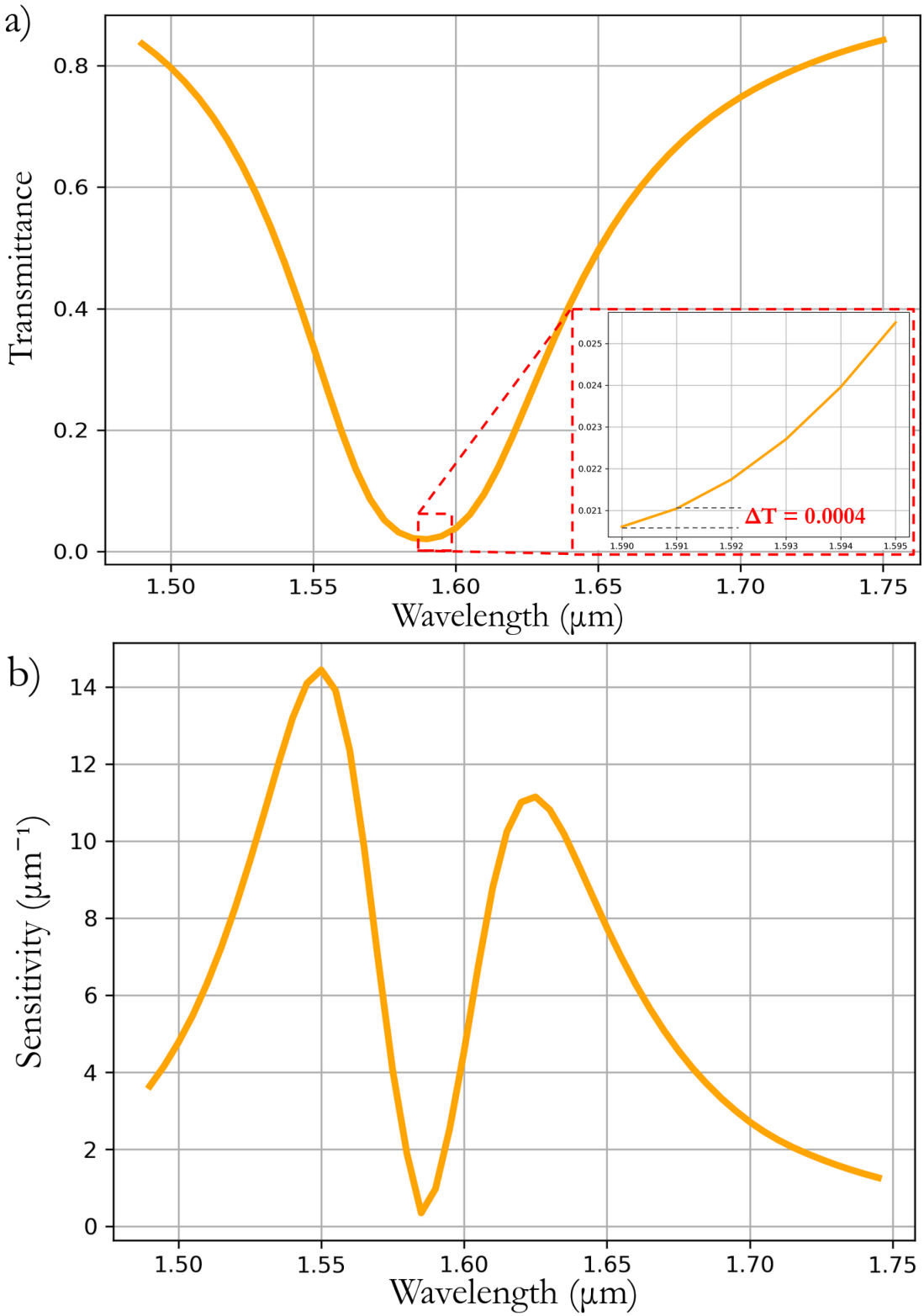

Figure 5.9: Resonance for optimized device. a) Transmittance curve with inset indicating that the p_{sat} condition is satisfied and b) Sensitivity curve showing that its maxima occurs at the desired wavelength of 1550 nm.

Since the principle of operation of the sensor is based on the variation of transmittance due to concentration variation, there must be a justification for an opti-

mization procedure that is being conducted in terms of wavelength. Considering that, ideally, the optimization should maximize the transmittance variation for a particular change in gas concentration at a particular wavelength, one should employ an initial guess for each layer of the OMH structure, and obtaining such an initial guess depends on the tuning of the resonance, a feature that is contemplated in Algorithm 3. Additionally, this optimization in terms of wavelength can be considered an approximation to the sensitivity $S(c(\%)) = |\partial T/\partial c(\%)|$ since under the condition of resonance, the wavevector on the Pd layer $k_{Pd} = k_{sp}$, with k_{sp} being the surface plasmon wavevector, is approximately invariant, leading to the claim that a variation on the refractive index of the Pd layer is directly proportional to a variation of refractive index. There are two arguments against this approximation, for example, the fact that for larger resonance widths, such as the case presented in Fig. 5.9, assuming the wavevector coupling condition is not adequate and the fact that the refractive index variation occurs on both real and imaginary parts. Nonetheless, this strategy is employed in order to obtain reasonable sensitivity for a wavelength of choice, and its result can then be applied to an optimization for maximizing $S(c(\%))$ as an initial guess.

It is important to notice that the optimization strategy is conducted with a fixed value of residual cladding T_r that is considered enough to guarantee the mechanical stability of the D-shaped section of the optical fiber. Employing thinner residual cladding would affect the resonance by increasing losses on the D section leading to deeper resonances for the same set of OMH thicknesses. It is expected, initially, that the same sensor performance would then be obtained from different values of d_m and d_h, and with a re-design of the OMH structure it would not necessarily lead to better sensitivity. Later on this chapter, a new design will be conducted to investigate this effect. Nonetheless, variations on residual cladding should be considered in the device design since the uncertainty of the fabrication method can impact the sensor performance and it is notably relevant for its possible impact on saturation.

To ensure that the uncertainty on the T_r value coming from the fabrication error does not impose a loss of resolution due to resonance saturation, the effect of residual cladding variation according to the uncertainty σ the polishing procedure described in (Alves et al.,2022) is adopted. With an uncertainty of $\sigma = \pm 90$ nm, Fig 5.10 shows the results of the variation on the device resonance and impact on sensitivity.

It is shown that, for the suggested fabrication procedure, there would be no significant loss of sensitivity due to the uncertainty of residual cladding. For the case in which $T_r = 2.5\mu m - \sigma$, it is calculated a $\Delta T = 0.009$ for $\Delta\lambda = 1$ nm, ensuring that the condition ρ_{sat} is still met.

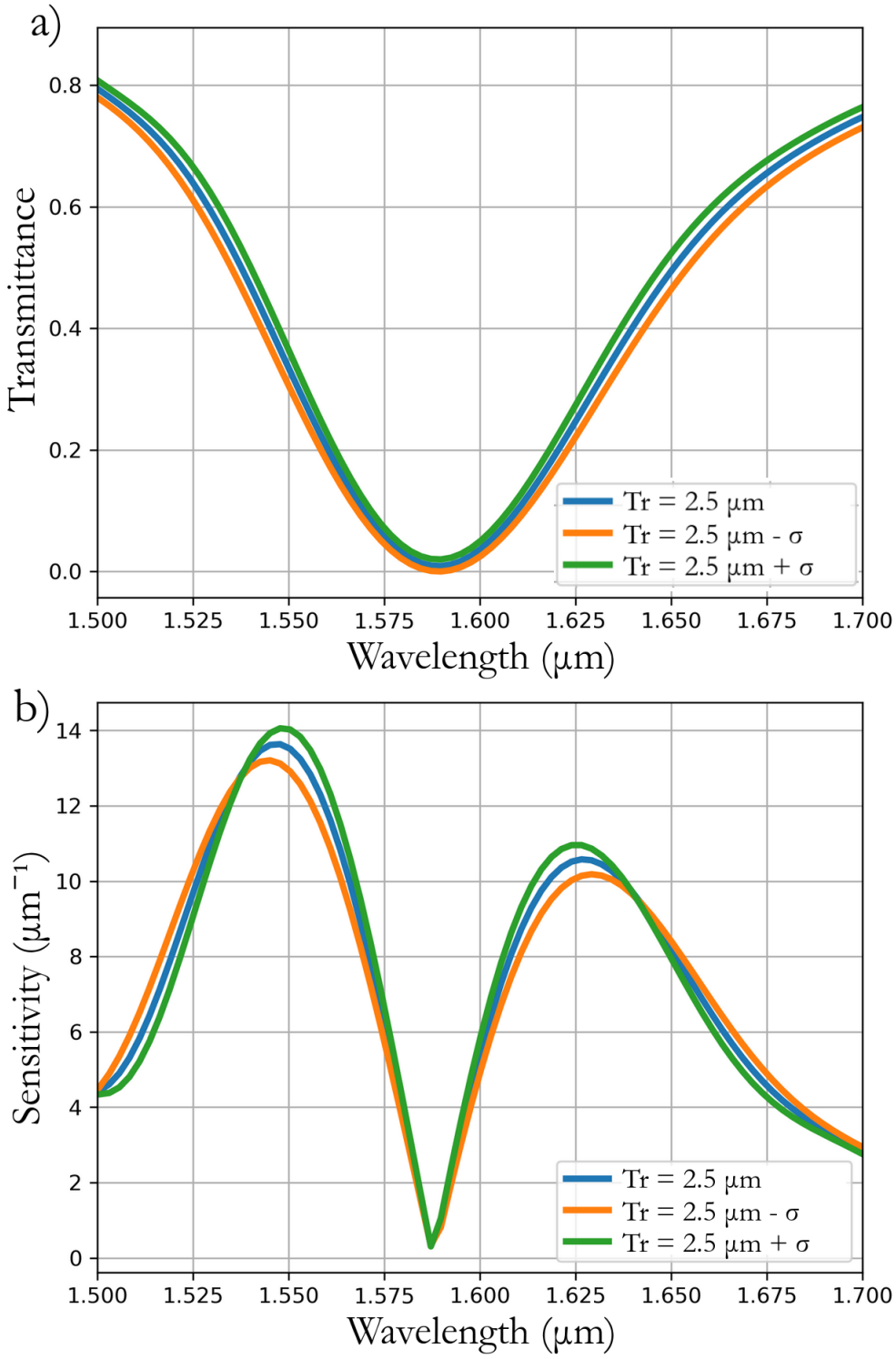

Figure 5.10: Impact of uncertainty of residual cladding on a) Transmittance curve and b) Sensitivity curve.

5.4 Computational Experiment on Designed Sensors Subjected to Hydrogen Gas Presence

With the optimized structure, a computational experiment was conducted to assess the performance of the device under hydrogen load. The effect of the gas presence on the device resonance is investigated and two different interrogation schemes are proposed, fixed wavelength and sinusoidally modulated wavelength, in the last case two different detection schemes were investigate, FFT-based and Lock-in amplifier-based detection.

Concentrations between 0% and 4% were investigated, that is, below the Lower Explosive Limit (LEL). The percentage concentration $c(\%)$ is related to atomic concentration n through Eq. 4.42 and the optical and thickness variation are calculated from Eqs. 4.22 and 4.29. From this procedure, for the mentioned concentration range, results for the effects of hydrogen absorption are shown in Table 5.1.

Table 5.1: Optical and mechanical variations for Pd grating.

n	$c(\%)$	$Re(\eta_{ef})$	$Im(\eta_{ef})$	d (nm)
0.0075	0.5	3.25	8.12	1.000942
0.015	1	3.57	7.93	1.001885
0.023	1.5	3.94	7.76	1.002890
0.03	2	4.28	7.64	1.003770
0.038	2.5	4.68	7.55	1.004775
0.046	3	5.09	7.50	1.005780
0.054	3.5	5.49	7.49	1.006786
0.061	4	5.84	7.51	1.007665

It is clear that the hydrogen-dependent variation that dominates the sensitivity is the optical one, with thickness changes being on the order of 10^{-3} nm, corroborating the argument previously presented on the possibility of employing thicker Pd layers for greater mechanical variation and, therefore, greater sensitivity. The results of the

effect of hydrogen presence on the device resonance is shown in Fig. 5.11, showing that there is significant transmission variation for the investigated concentration range.

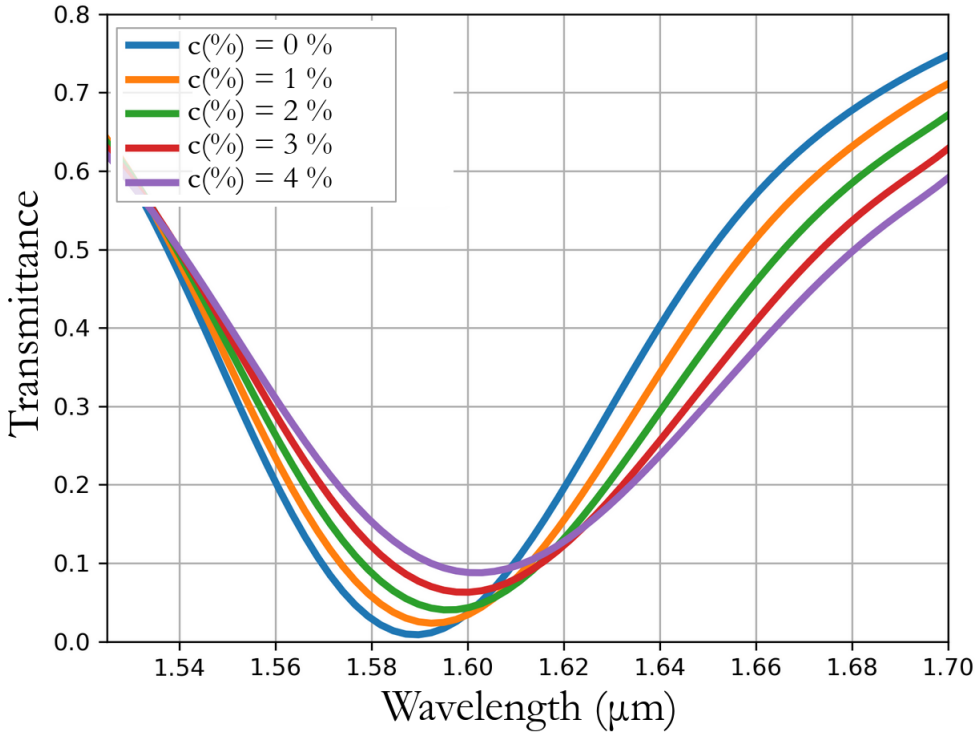

Figure 5.11: Effect of hydrogen gas presence on the device resonance between 0%-4% concentration range.

It is noticeable that a higher variation in transmittance is observed around 1.66 μm than in the previously chosen wavelength of 1.55 μm. This can be explained considering the results in table 5.1, in which the variation of $Re(\eta_{ef})$ with respect to $c(\%)$ is significantly linear, but $Im(\eta_{ef})$ shows stagnation for concentrations above 2.5%. For this reason, the gas presence has the effect of shifting the resonance and increasing its width with the $Re(\eta_{ef})$ variation being the dominant cause and this widening effect occurs mostly in the second half of the resonance, that is, beyond the wavelength of maximum coupling. With the possible problem of obtaining greater sensitivity on larger wavelengths at the risk of being on the spectrum of higher losses on the fiber, one can run the optimization described in Algorithm 3 in order to ensure that the second peak of sensitivity (see Fig. 5.9) is tuned at the desired wavelength.

Considering a practical operation of this device, it could be interesting to observe the effect of the gas concentration on the transmittance of the device for a fixed wavelength, in this case, $\lambda = 1550$ nm. Fig 5.12 shows the results. The obtained linear sensitivity was 0.01712 $\%^{-1}$

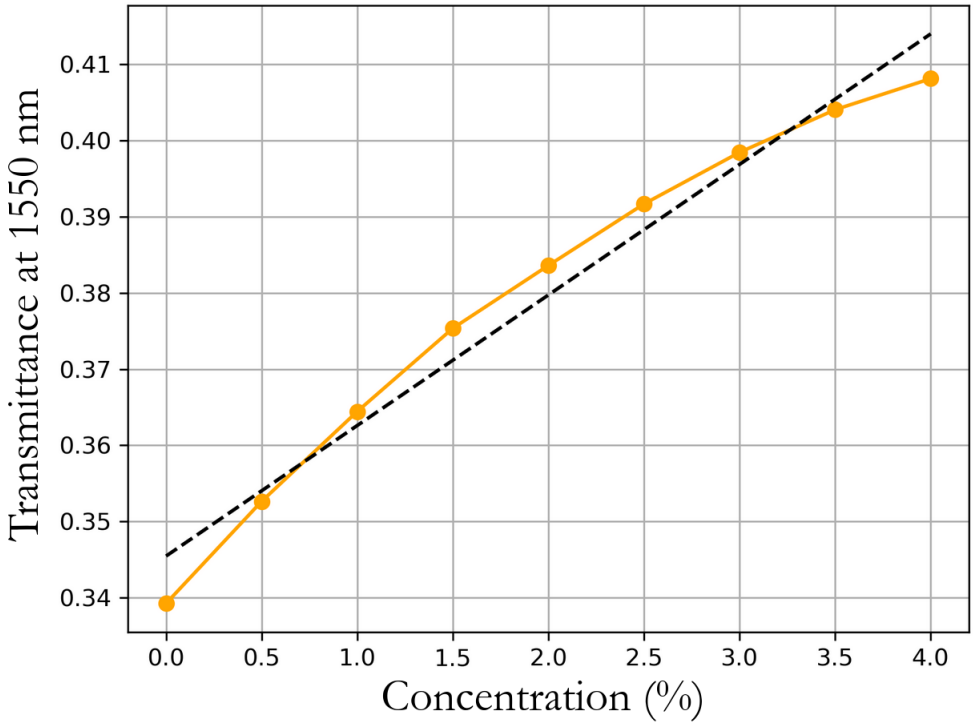

Figure 5.12: Effect of hydrogen gas presence on the transmittance at 1550 nm between 0%-4% concetration range.

The non-linearity of this proposed interrogation scheme is noticeable with the signal presenting a clear parabolic profile, even though it benefits from the simple experimental setup and control needed to implement this instrument. Harmonic detection techniques with FFT and lock-in amplifier-based detection schemes are employed to investigate the possibility of obtaining higher linearities.

5.5 Wavelength Modulation Techniques in D-shaped OMH structures

Considering the wavelength modulation interrogation, a sinusoidally modulated beam with central wavelength $\lambda = 1550$ nm and amplitude $\Delta\lambda = \pm 0.3$ nm was used.

The optoelectronic detection circuit and modulation frequency considered were the same as described in Section 4.4.2.

For the FFT-based detection, the same principles of using the magnitude of the transform at the modulation frequency as the sensor signal are used. Fig. 5.13 shows the result of the obtained response, it is clear that some degree of non-linearity is observed. The linear sensitivity calculated was 5.132 $mV/\%$.

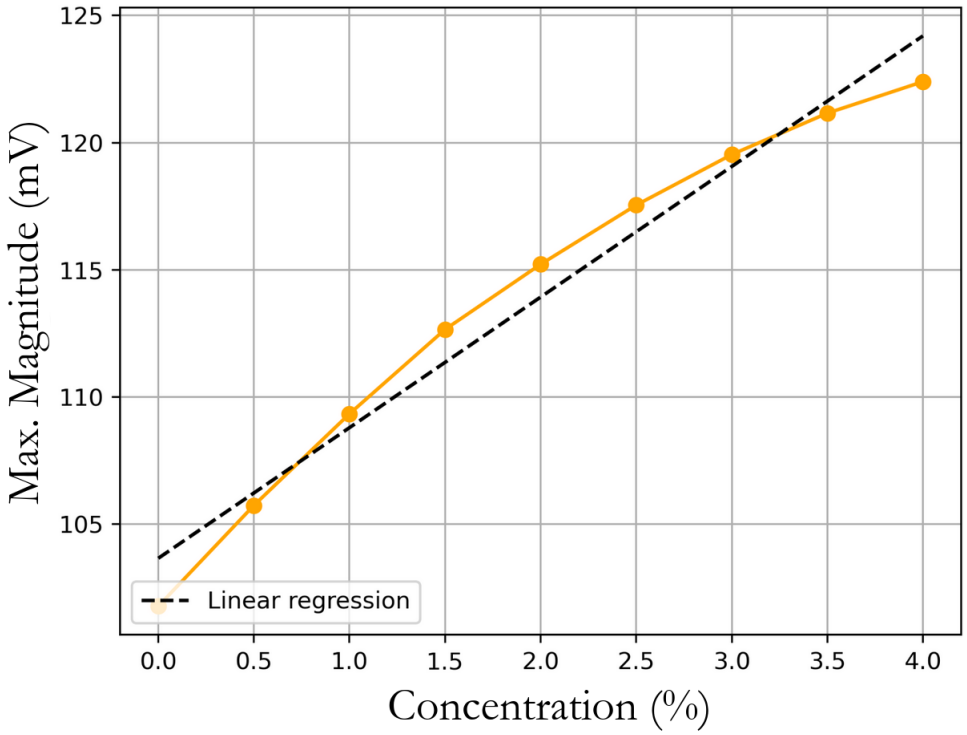

Figure 5.13: Maximum values of the FFT in function of hydrogen gas concentration.

The lock-in computational analysis explored all available signals, which are the in phase, quadrature, phase and magnitude signals. The lock-in based detection permitted highly linear measurements for in phase, quadrature and magnitude signals, with sensitivities of $1.2 \cdot 10^{-6} mV/\%$, $1.6 \cdot 10^{-6} mV/\%$ and $2.0 \cdot 10^{-6} mV/\%$ magnitude components. The phase signal resulted with a slightly higher degree of non-linearity compared to other lock-in signals with linear sensitivity of 3.8 mrad/%. Fig 5.14 show the obtained results.

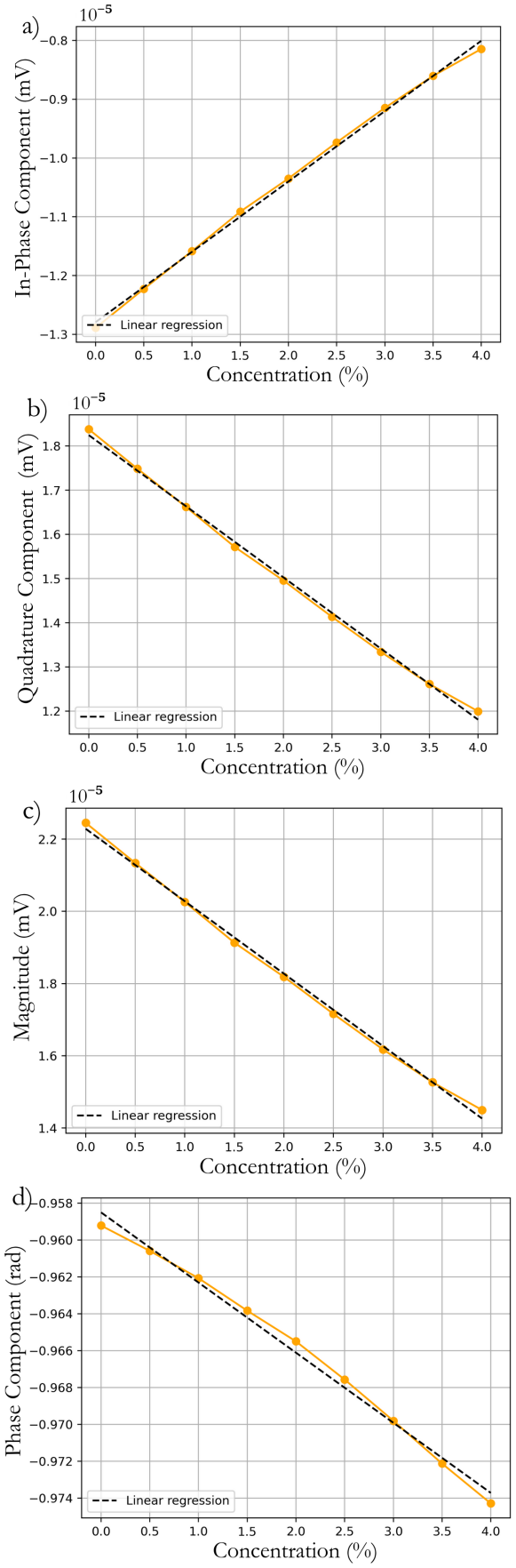

Figure 5.14: Lock-in analysis for the sensor response. a) In-phase, b) Quadrature, c) Magnitude and d) Phase components

To find the Limit of Detection (LOD) of this technique, the same optoelectronic detection circuit is considered, as described in Section 4.4.2 to provide easier comparison between both techniques. As previously explained, the LOD based on minimum detectable change of optical power is $1.52 \cdot 10^{-5}$. Considering this value, the numerical model was used to calculate, based on concentration dependent optical and mechanical variation, the concentration needed to provide such a optical power variation at 1550 nm incident wavelength. The resulting LOD in terms of hydrogen concentration is $LOD_{c(\%)} = 5,04 \cdot 10^{-4}\%$, corresponding to 5.04 ppm.

Two other situations are explored in order to investigate previously mentioned hypotheses. Firstly, a new design is generated to ensure that the choice of thinner layers of the hydride provide better results than employing thicker values. For that, it is used a fixed value for the Pd thickness layer of 5 nm and optimal values of d_o and d_m are obtained according to a procedure similar to Algorithm 1. The obtained structure is then $d_o = 568$ nm, $d_m = 9.5$ nm and $d_h = 5$ nm. The sensor response in a fixed wavelength interrogation is shown in Fig 5.15 with a linear sensitivity of -0.00985$\%^{-1}$. It is clear, in comparison with Fig. 5.12, that this approach does not lead to more sensitive devices since the signal variation for the same concentration range is smaller. This confirms the hypothesis that aiming for higher sensitivities by employing thicker films is an inefficient design strategy since the optical variations dominate the sensitivity of the fiber sensor and not the mechanical one.

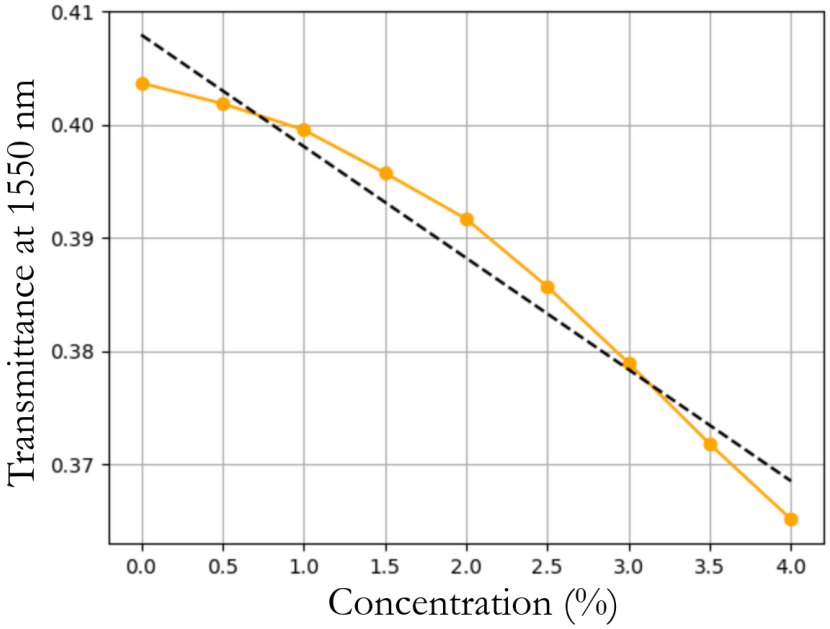

Figure 5.15: Fixed wavelength response to gas presence for structure with $d_o = 568$ nm, $d_m = 9.5$ nm and $d_h = 5$ nm.

The other hypothesis is that similar sensitivity could be achieved by employing different residual cladding thickness by adjusting the thicknesses of the OMH structure. To investigate this claim, a new design is conducted for a fixed value of $T_r = 1.5\mu$m. Using the same initial guesses for the oxide, metal and hydride layers and Algorithm 1, the obtained structure was $d_o = 566$ nm, $d_m = 2$ nm and $d_h = 8$ nm. The result is seen in Fig. 5.16.

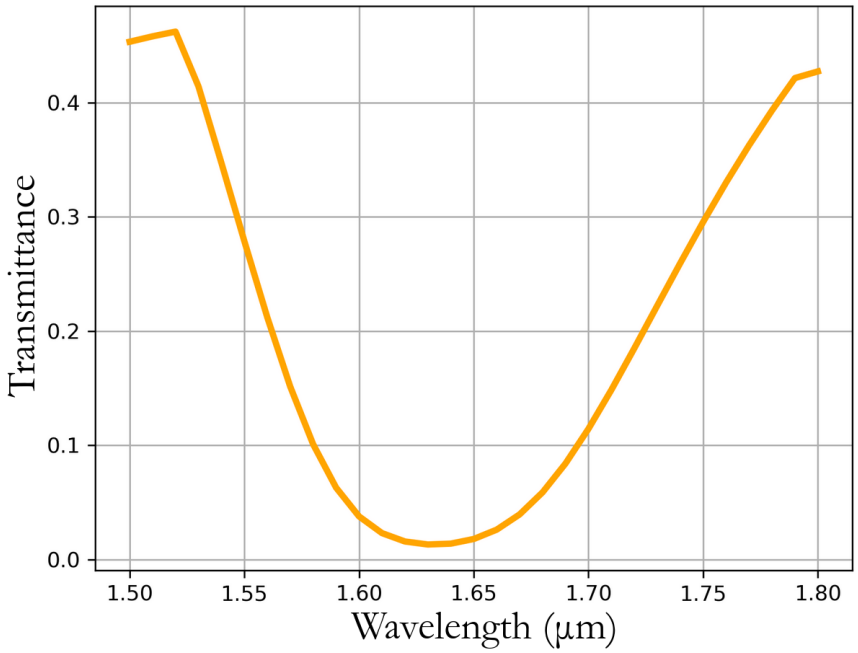

Figure 5.16: Transmitance curve for device with $T_r = 1.5\mu$m, $d_o = 566$ nm, $d_m = 2$ nm and $d_h = 8$ nm.

It is noticeable that decreasing the thickness of the residual cladding increases the losses in the D profile region, which was, of course, expected. But it is also noticeable that the losses influence a wide region of the spectrum, with a tendency to saturate the resonance valley and increase the resonance width. So, to avoid saturation, it is necessary to considerably reduce the sensitivity of the device by employing thinner metal layers and thicker hydride layers. It was also investigated the fixed wavelength response of the sensor, as shown in Fig. 5.17. The linear sensitivity obtained was -0.0109 $\%^{-1}$.

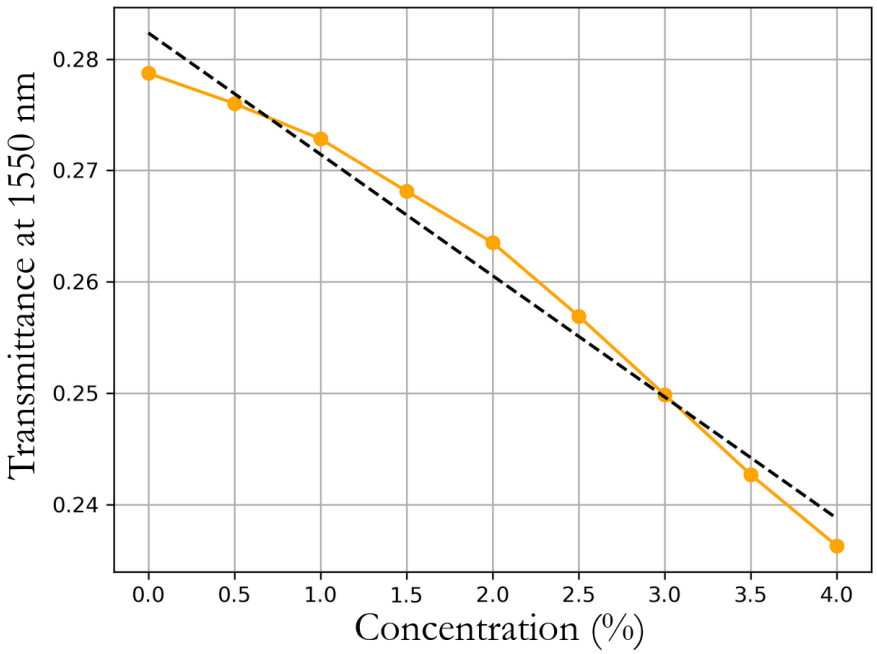

Figure 5.17: Transmitance curve for device with $T_r = 1.5\mu$m, $d_o = 566$ nm, $d_m = 2$ nm and $d_h = 8$ nm.

With this result one can conclude that the initial design defined by $T_r = 2.5\mu$m, $d_o = 515.5$ nm, $d_m = 2$ nm and $d_h = 1$ nm, presents the most sensitive one.

One should notice that every design considered here employs a 3 mm D section length, L_D. From a fabrication perspective, it could be interesting to employ higher values of L_d. The expected effect is that the increase of the D section length should bring higher losses, similarly to the decrease of T_r. A strategy of increasing L_d and decreasing T_r could result in a sensitive device if these two effects are correctly dimensioned.

Chapter 6

Conclusion and Future Works

6.1 Conclusion

This thesis concerns, mainly, the theory and computational engineering techniques in metal hydride plasmonics and its devices and systems. In light of the scenario of the state of the literature review presented in Chapter 2, this work suggested the Harmonic Minimization Method for optimal design of plasmonic diffraction grating sensors, the Tunable Diode Laser Plasmonic Grating Spectroscopy technique for portable plasmonic sensing and its application to hydrogen gas detection with Pd and Nb gratings. This thesis also proposes a sensor based on Oxide/Metal/Hydride structure over D-shaped optical fiber for hydrogen sensing and a fabrication constraint-aware optimization procedure.

Concerning the HMM computational data results presented, it can be concluded that with the development of such method for the design of metallic diffraction gratings sensors is effective in terms of obtaining maximum sensitivity structures, particularly when compared to those designed using a C method-based approach.

The proposed method, when integrated with a Rayleigh-based optimization algorithm, introduces no significant additional computational cost, achieving an average computation time of approximately 8.22 seconds, with 89.23% of this time attributed to compilation. Furthermore, it was observed that the structural parameters converge appropriately with an increase in the number of harmonics used in

the optimization process for both rectangular and triangular gratings profile.

A batch of devices was fabricated in accordance with a design obtained using the HMM, and the structural parameters of a sample were measured using AFM and SEM. The experimental characterization data were subsequently employed in numerical calculations of the grating's spectrum, allowing its sensitivity to be compared with the structure defined by the nominal parameters. Real and designed devices show similar sensitivities.

The Tunable Diode Laser Plasmonic Grating Spectroscopy (TDLPGS) technique introduced in this work presents a well-founded system architecture suitable for implementing portable plasmonic measurement systems, applicable in both gaseous and liquid environments. The proposed simulation method, based on homogenization theory for effective dielectric function modeling and the elastic expansion model, is well suited for analyzing the plasmonic properties of hydrogen-absorbing metal sensors.

Simulation results demonstrate that for the system architecture evaluated under wavelength modulation interrogation—through a computational implementation of FFT analysis of the detected optical signal—reasonable linearity was observed in Pd gratings for concentration ranges of $0 \leq n \leq 0.07$ and $0 \leq n \leq 0.007$ for both substrate cases. For Nb-based structures, good linearity was obtained for $0 \leq n \leq 0.005$ under a rigid substrate, but highly non-linear detection was observed for a flexible substrate in the range $0 \leq n \leq 0.0005$.

For Pd structures, detection based on a digital lock-in detection scheme resulted in highly linear detection for all four signal components under a flexible substrate for $0 \leq n \leq 0.007$. For Nb gratings with a rigid substrate, high linearity was also achieved for all four components within the concentration range $0 \leq n \leq 0.005$. For a flexible substrate, good linearity was observed for the magnitude, in-phase, and quadrature components for $0 \leq n \leq 0.0005$. Additionally, it is calculated that for the implementation with Nb diffraction gratings using the lock-in amplifier, the system could achieve a ppm detection limit while maintaining good linearity.

An estimation of the sensor response time is also proposed in order to permit the designer to choose adequate materials and spectral ranges in order to optimize the response time, even tough other considerations of experimental nature, such as the design of the gas chamber and velocity of gas flow, would be very important to determine the system final response time.

The presented work on Oxide/Metal/Hydride structure over D-shaped optical fibers presented a proposal of a device, optimization routine and measurement method. The device design considers a TiO_2 layer for resonance shifting from the visible spectrum to the infrared spectrum in order to obtain a response on the low loss spectral region of a single mode fiber, together with a Au layer with the purpose of increasing the sensitivity of the device since it has a greater imaginary refractive index compared to Pd. The third layer is a hydride-forming material, in the case of this device, Pd. The last layer is in contact with the sensing medium containing a hydrogen gas concentration and is used to provide specificity to the sensor.

The optimization procedure is based on declaring the fabrication constraints in terms of minimal and maximum layer thickness limits, as wells as central wavelength of operation and employing a recursive gradient-based optimization to result in thicknesses of each layer of the OMH structure. Such procedure results in a structure with the central wavelength previously declared being the point of maximum sensitivity with respect to wavelength variations.

The main transduction mechanism of the fiber-based device is the modulation of the real and imaginary refractive index of the Pd layer that occurs with the formation of the hydride. Since optimal structures are obtained with thin hydride layers, the thickness variation due to hydrogen absorption is negligible and leads to no significant increase in the sensitivity of the device.

The device, when operated in a fixed wavelength interrogation mode showed good sensitivity but also a significant degree of non-linearity for the 0% to 4% concentration range. However, this interrogation method permits a very simple operation from an experimental perspective. Harmonic detection systems are also suggested

to be employed with the fiber-based device, in which the FFT and Lock-in analysis were investigated in order to obtain higher sensitivities and better linearities. It was shown that with a sinusoidal modulated incident beam with 1550 nm of central wavelength and 0.3 nm amplitude, the lock-in amplifier analysis resulted in highly-linear measurements.

This thesis provides a contribution to existing knowledge of a number of engineering techniques for hydrogen gas sensing. The HMM, in which the idea of aligning a low complexity diffraction formalism with a profile translation algorithm based on harmonic analysis was first proposed. This computational method permits the design of multiple gratings with different profiles based on a single sinusoidal grating, permitting easy comparison of different structures in terms of sensitivity and adequacy of fabrication with minimum computational complexity. This method can be employed for the design of diffraction grating for different target analytes and different materials, being transferable for multiple scenarios in which the design of grating-based sensing is important. Future works on the HMM will include a thorough investigation of profiles and materials not yet researched, as well as validation of the choice of algorithm parameters in different regions of the spectra. The behavior of the non-linear regression quality parameters for different scenarios should also be studied in the near future. Another possibility is the investigation of the HMM capability of designing grating with modulated widths.

The TDLPGS technique proposed has its greater significance in the proposal of a system architecture that permits the construction of portable plasmonic measurement systems, with this setup finding applications in different sensing scenarios as well. The principle of using the grating periodicity variation as a direct contribution to the device's final sensitivity was also presented for the first time in the literature, as far as the knowledge of the author goes. Future work will include a comprehensive analysis of the effects of plastic deformation under hydrogen loading on plasmonic coupling properties and its contribution to device reversibility. It will also be the subject of research on how to include reversibility in the design

procedure of the grating device. Furthermore, the experimental implementation of the proposed technique remains a key objective of the research group. Only then can the models suggested here be compared to experimental data, enabling further refinements and developments of the model. The optimization of the modulation frequency will also be investigated.

Also, a design routine has been proposed for OMH structures for D-shaped optical fiber. Considering that until this work there was no clear design methodology proposed in the literature for plasmonic sensors in D-fibers. This work presents a computational analysis of the effect of each device parameter and provides an analysis of the presence of hydrogen gas on the designed structure. The optimization strategy will still be refined to include an extra step for maximizing the transmittance variation for a particular change in gas concentration, using the wavelength-based optimization result as an initial guess. The effect of the choice of which sensitivity peak to use will also be thoroughly investigated in light of the effect of $Re(n_{ef})$ variation. Future works concerning the proposal of this device will deal with the fabrication of OMH structures for D-shaped fiber and its experimental characterization and validation as a sensor.

Chapter 7

Accomplishments

This chapter brings the accomplishments of this thesis work in terms of published journal articles, conference papers, recognitions and prizes.

7.1 Journal Articles

- Prospects for Developing Pressure and Tactile Sensors Based on Surface Plasmon Resonance - *IEEE Sensors Journal*. Vol 22, Issue 19, pages 18620 - 18630. José Otávio Maciel Neto, **Gabriel de Freitas Fernandes**, Gustavo Oliveira Cavalcanti, Ignacio Llamas-Garro, Jung-Mu Kim, Eduardo Fontana. DOI: 10.1109/JSEN.2022.3199730.

- Tunable Diode Laser Plasmonic Grating Spectroscopy for Hydrogen Sensing - *IEEE Photonics Journal*. Vol. 17, Issue 3. **Gabriel de Freitas Fernandes**, Ignacio Llamas-Garro, Joaquim Ferreira Martins-Filho, Eduardo Fontana. DOI: 10.1109/JPHOT.2025.3567000.

- Harmonic minimization method for plasmonic diffraction grating sensor design - *Applied Optics*. Vol 64, Issue 15, pages 4415-4425. **Gabriel de Freitas Fernandes**, Felipe José Lucena de Araújo, Ernande Ferreira de Melo, Ignacio Llamas-Garro, Joaquim Ferreira Martins-Filho, Eduardo Fontana. DOI: 10.1364/AO.560988

- Non Invasive Profilometry of Sealed Otto Chip Devices by Scanning Optical Reflectometry - *IEEE Transactions on Instrumentation and Measurement.* Vol 72. **Gabriel de Freitas Fernandes**, Jung-Mu Kim, Ignacio Llamas-Garro, Gustavo Oliveira Cavalcanti, Joaquim Ferreira Martins-Filho, Eduardo Fontana. DOI: 10.1109/TIM.2025.3590830

- Oxide/Metal/Hydride Plasmonic Devices for Hydrogen Sensors Based on D-shaped Optical Fibers. (Under development). **Gabriel de Freitas Fernandes**, Henrique Patriota Alves, Joaquim Ferreira Martins Filho.

7.2 Conference Papers

- Tunable diode laser surface plasmon spectroscopy - *2022 International Optics and Photonics Conference.* **Gabriel de Freitas Fernandes**, Raoni Freitas de Góes, Ernande Ferreira de Melo, Eduardo Fontana. DOI: 10.1109/SBFotonIOPC54450.2022.9992903

- Harmonic Minimization Method for Pd Plasmonic Diffraction Grating Design - *2024 International Optics and Photonics Conference.* **Gabriel de Freitas Fernandes**, Ernande Ferreira de Melo, Eduardo Fontana. DOI: 10.1109/SBFotonIOPC62248.2024.10813538

- Design of Oxide/Metal/Hydride Plasmonic Devices Based on D-shaped Optical Fibers for H_2 Sensing. Submitted to *2025 International Optics and Photonics Conference.* **Gabriel de Freitas Fernandes**, Henrique Patriota Alves, Joaquim Ferreira Martins-Filho.

7.3 Recognitions and Prizes

- 1st place in Doctorate admission process, awarded with CNPq scholarship - Universidade Federal de Pernambuco. 2021

- Best paper award - 2022 International Optics and Photonics Conference. 2022
- CAPES Print Scholarship. 2023
- Startup 20 prize. Prize conceded during Startup 20 event, a G20 forum, to TerraSafe, a solution for in depth soil moisture sensing for landslide prevention. 2024

References

(2016). Elsevier.

Alleyne, C. J., Kirk, A. G., McPhedran, R. C., Nicorovici, N.-A. P., e Maystre, D. (2007). Enhanced spr sensitivity using periodic metallic structures. *Optics Express*, 15(13):8163.

Alves, H. P., Castro de Barros, T. H., Silva Nascimento, D. L., Peixoto e Silva, M. S., do Nascimento, J. F., Fontana, E., e Martins-Filho, J. F. (2022). Influence of surface roughness on the sensitivity of a d-shaped optical fiber-based refractive index sensor. *Sensors and Actuators A: Physical*, 344:113702.

Angstenberger, S., Floess, M., Schmid, L., Ruchka, P., Steinle, T., e Giessen, H. (2025). Coherent control in quartz-enhanced photoacoustics: fingerprinting a trace gas at ppm-level within seconds. *Optica*, 12(1):1.

Ans, S., Zamkotsian, F., e Demésy, G. (2024). Topology optimization of blazed gratings under conical incidence. *Journal of the Optical Society of America A*, 41(8):1531.

Arnoldi, W. E. (1951). The principle of minimized iterations in the solution of the matrix eigenvalue problem. *Quarterly of Applied Mathematics*, 9(1):17–29.

Arora, P., Talker, E., Mazurski, N., e Levy, U. (2018). Dispersion engineering with plasmonic nano structures for enhanced surface plasmon resonance sensing. *Scientific Reports*, 8(1).

Augulis, R. e Zigmantas, D. (2011). Two-dimensional electronic spectroscopy with double modulation lock-in detection: enhancement of sensitivity and noise resistance. *Optics Express*, 19(14):13126.

Avetisov, V., Bjoroey, O., Wang, J., Geiser, P., e Paulsen, K. G. (2019). Hydrogen sensor based on tunable diode laser absorption spectroscopy. *Sensors*, 19(23):5313.

Bao, G., Chen, Z., e Wu, H. (2005). Adaptive finite-element method for diffraction gratings. *Journal of the Optical Society of America A*, 22(6):1106.

Bathe, K.-J. (2008). Finite element method.

Bautista-Morales, M. d. R., Martínez-Manuel, R., López-Cortés, D., Pineda-Arellano, C. A., Esteban, , e Shlyagin, M. G. (2018). Multi-point fiber-optic refractometer using the fresnel reflections at fiber tips. In *26th International Conference on Optical Fiber Sensors*, volume 19 of *OFS*, página ThE28. OSA.

Bdour, Y. e Sabat, R. G. (2024). Real-time plasmonic strain sensors based on surface relief diffraction gratings. *Micromachines*, 15(7):863.

Beaumont, M., Ventrillard, I., e Romanini, D. (2024). Optical cavity spectroscopy using heterodyne detection with optical feedback laser frequency locking. *Applied Optics*, 63(9):2227.

Bijalwan, A. e Rastogi, V. (2017). Sensitivity enhancement of a conventional gold grating assisted surface plasmon resonance sensor by using a bimetallic configuration. *Applied Optics*, 56(35):9606.

Bijalwan, A. e Rastogi, V. (2018). Design analysis of refractive index sensor with high quality factor using au-al2o3 grating on aluminum. *Plasmonics*, 13(6):1995–2000.

Bijalwan, A. e Rastogi, V. (2019). Design and simulation of a palladium-aluminum nanostructure-based hydrogen sensor with improved figure of merit. *IEEE Sensors Journal*, 19(15):6112–6118.

Bolef, D. I. (1961). Elastic constants of single crystals of the bcc transition elements v, nb, and ta. *Journal of Applied Physics*, 32(1):100–105.

Bolshov, M., Kuritsyn, Y., e Romanovskii, Y. (2015). Tunable diode laser spectroscopy as a technique for combustion diagnostics. *Spectrochimica Acta Part B: Atomic Spectroscopy*, 106:45–66.

Bonati, C., Fay, V., Dornier, R., Loterie, D., e Moser, C. (2022). Lock-in raman difference spectroscopy. *Optics Express*, 30(16):28601.

Bondi, A. (1964). van der waals volumes and radii. *The Journal of Physical Chemistry*, 68(3):441–451.

Borile, G., Rossi, S., Filippi, A., Gazzola, E., Capaldo, P., Tregnago, C., Pigazzi, M., e Romanato, F. (2019). Label-free, real-time on-chip sensing of living cells via grating-coupled surface plasmon resonance. *Biophysical Chemistry*, 254:106262.

Brand, C., Fiedler, J., Juffmann, T., Sclafani, M., Knobloch, C., Scheel, S., Lilach, Y., Cheshnovsky, O., e Arndt, M. (2015). A green's function approach to modeling molecular diffraction in the limit of ultra-thin gratings. *Annalen der Physik*, 527(9-10):580–591.

Brolo, A. G., Gordon, R., Leathem, B., e Kavanagh, K. L. (2004). Surface plasmon sensor based on the enhanced light transmission through arrays of nanoholes in gold films. *Langmuir*, 20(12):4813–4815.

Bruggeman, D. A. G. (1935). Berechnung verschiedener physikalischer konstanten von heterogenen substanzen. i. dielektrizitätskonstanten und leitfähigkeiten der mischkörper aus isotropen substanzen. *Annalen der Physik*, 416(7):636–664.

Butler, M. A. (1984). Optical fiber hydrogen sensor. *Applied Physics Letters*, 45(10):1007–1009.

Butler, M. A. (1991). Fiber optic sensor for hydrogen concentrations near the explosive limit. *Journal of The Electrochemical Society*, 138(9):L46–L47.

Butler, M. A. e Ginley, D. S. (1988). Hydrogen sensing with palladium-coated optical fibers. *Journal of Applied Physics*, 64(7):3706–3712.

Bévenot, X., Trouillet, A., Veillas, C., Gagnaire, H., e Clément, M. (2000). Hydrogen leak detection using an optical fibre sensor for aerospace applications. *Sensors and Actuators B: Chemical*, 67(1–2):57–67.

Cai, D., Lu, Y., Lin, K., Wang, P., e Ming, H. (2008). Improving the sensitivity of spr sensors based on gratings by double-dips method (ddm). *Optics Express*, 16(19):14597.

Calvani, R., Caponi, R., Naddeo, C., Roccato, D., e Rosso, M. (1995). Ultrashort pulses from a gain-switched DFB laser by fiber compensation of the chirp and thermal tuning of the cavity. *Optical Fiber Technology*, 1(4):346–351.

Cantelli, R., Mazzolai, F. M., e Nuovo, M. (1969). Internal friction due to long-range diffusion of hydrogen in niobium (gorsky effect). *physica status solidi (b)*, 34(2):597–600.

Cao, J., Sun, Y., Kong, Y., e Qian, W. (2019). The sensitivity of grating-based spr sensors with wavelength interrogation. *Sensors*, 19(2):405.

Cao, R., Wu, J., Liang, G., Ohodnicki, P. R., e Chen, K. P. (2020). Functionalized pdau alloy on nanocones fabricated on optical fibers for hydrogen sensing. *IEEE Sensors Journal*, 20(4):1922–1927.

Carvalho, J. P., Frazão, O., Baptista, J. M., Santos, J. L., e Barbero, A. P. (2012). DFB laser based electrical dynamic interrogation for optical fiber sensors. In Berghmans, F., Mignani, A. G., e Moor, P. D., editors, *Optical Sensing and Detection II*. SPIE.

Chadwick, B. e Gal, M. (1993). Enhanced optical detection of hydrogen using the excitation of surface plasmons in palladium. *Applied Surface Science*, 68(1):135–138.

Chai, J., Lin, Z., Wang, Y., Liu, X., Chai, Y., Wang, L., e Kang, G. (2025). Low-cost, high-performance refractive index sensing with ultranarrow resonance line width for wearable sensing. *ACS Applied Materials amp; Interfaces*.

Chamanzar, M., Mehrany, K., e Rashidian, B. (2006). Planar diffraction analysis of homogeneous and longitudinally inhomogeneous gratings based on legendre expansion of electromagnetic fields. *IEEE Transactions on Antennas and Propagation*, 54(12):3686–3694.

Chandezon, J., Dupuis, M., Cornet, G., e Maystre, D. (1982). Multicoated gratings: a differential formalism applicable in the entire optical region. *Journal of the Optical Society of America*, 72:839–846.

Chandezon, J., Gavaix, A., Parriaux, O., e Kneale, C. (2019). Application of heisenberg uncertainty relation for the optimal modeling of surface diffraction. *Journal of the Optical Society of America A*, 36(4):594.

Chandezon, J., Raoult, G., e Maystre, D. (1980). A new theoretical method for diffraction gratings and its numerical application. *Journal of Optics*, 11(4):235–241.

Chen, L., Li, J., Liu, J., e Yang, H. (2020). A ag–au bimetallic nanograting surface plasmon resonance sensor based on a prism structure. *Optics Communications*, 461:125105.

Cooley, J. W. e Tukey, J. W. (1965). An algorithm for the machine calculation of complex fourier series. *Mathematics of Computation*, 19(90):297–301.

da Silva, V. M., Filho, J. F. M., e do Nascimento, J. F. (2021). Cascaded refractive index and corrosion sensors in a d-shaped optical fiber using lmr and spr effects. In *2021 SBFoton International Optics and Photonics Conference (SBFoton IOPC)*, página 1–5. IEEE.

de Araujo, F. J. L., de Melo, E. F., e Fontana, E. (2023). Particle swarm optimizer for the surface plasmon resonance effect on metal gratings. *Applied Optics*, 62(23):6120.

De Freitas Fernandes, G., De Freitas Gois, R., De Melo, E. F., e Fontana, E. (2022). Tunable diode laser surface plasmon spectroscopy. In *2022 SBFoton International Optics and Photonics Conference (SBFoton IOPC)*, página 1–4. IEEE.

De Freitas Fernandes, G., De Melo, E. F., e Fontana, E. (2024). Harmonic minimization method for pd plasmonic diffraction grating design. In *2024 SBFoton International Optics and Photonics Conference (SBFoton IOPC)*, página 1–3. IEEE.

de Melo, E. F. (2013). Otimização de sensores Ópticos por ressonância de plásmons de superfície em grades de difração metalizadas. *Programa de Pós-Graduação em Engenharia Elétrica*.

Dhawan, A., Canva, M., e Vo-Dinh, T. (2011). Narrow groove plasmonic nano-gratings for surface plasmon resonance sensing. *Optics Express*, 19(2):787.

Dostálek, J. e Homola, J. (2008). Surface plasmon resonance sensor based on an array of diffraction gratings for highly parallelized observation of biomolecular interactions. *Sensors and Actuators B: Chemical*, 129(1):303–310.

Díaz-Thomas, D. A., Ayache, D., Fagot, M., Loghmari, Z., Gilbert, A., Rouillard, Y., Baranov, A. N., Rodriguez, J.-B., Tournié, E., Vicet, A., e Cerutti, L. (2025). Single mode, distributed feedback interband cascade lasers grown on si for gas sensing. *Applied Physics Letters*, 126(3).

Edee, K., Plumey, J., e Chandezon, J. (2013). On the rayleigh–fourier method and the chandezon method: Comparative study. *Optics Communications*, 286:34–41.

Farahi, F., Leilabady, P. A., Jones, J. D. C., e Jackson, D. A. (1987). Interferometric fibre-optic hydrogen sensor. *Journal of Physics E: Scientific Instruments*, 20(4):432–434.

Fernandes, G., Araújo, F., Melo, E., Llamas-Garro, I., Martins-Filho, J., e Fontana, E. (2025). Harmonic minimization method for plasmonic diffraction grating sensor design. *Applied Optics*.

Fontana, E. (2004). Theoretical and experimental study of the surface plasmon resonance effect on a recordable compact disk. *Applied Optics*, 43(1):79.

Fontana, E., Kim, J.-M., Llamas-Garro, I., e Cavalcanti, G. O. (2015). Microfabricated otto chip device for surface plasmon resonance-based optical sensing. *Applied Optics*, 54(31):9200.

Garnett, J. M. (1904). XII. colours in metal glasses and in metallic films. *Philosophical Transactions of the Royal Society of London. Series A, Containing Papers of a Mathematical or Physical Character*, 203(359-371):385–420.

Gibson, W. C. (2021). *The Method of Moments in Electromagnetics*. CRC Press.

Golovashkin, A., Leksina, I., Motulevich, G., e Shubin, A. (1969a). Optical properties of niobium. *SOV PHYS JETP*, 29(1):27–34.

Golovashkin, A. I., Leksina, I. E., Motulevich, G. P., e Shubin, A. A. (1969b). Optical properties of niobium. *Journal Of Experimental and theoretical Physics*.

Goodman, J. W. (1969). Introduction to fourier optics. *Physics Today*, 22(4):97–101.

Goray, L. e Dashkov, A. (2020). Gpu-based optimizations of the boundary integral equation method to solve direct and inverse diffraction grating problems. *2020 Days on Diffraction (DD)*, null:31–37.

Goray, L., Jark, W., e Eichert, D. (2018). Rigorous calculations and synchrotron radiation measurements of diffraction efficiencies for tender x-ray lamellar gratings: conical versus classical diffraction. *Journal of synchrotron radiation*, 25 Pt 6:1683–1693.

Granet, G., Chandezon, J., Plumey, J., e Raniriharinosy, K. (2001). Reformulation of the coordinate transformation method through the concept of adaptive spatial resolution. application to trapezoidal gratings. *Journal of the Optical Society of America. A, Optics, image science, and vision*, 18 9:2102–8.

Grego, S., Gilchrist, K. H., Carlson, J. B., e Stoner, B. R. (2012). A compact and multichannel optical biosensor based on a wavelength interrogated input grating coupler. *Sensors and Actuators B: Chemical*, 161(1):721–727.

Gu, F., Wu, G., e Zeng, H. (2015). Hybrid photon–plasmon mach–zehnder interferometers for highly sensitive hydrogen sensing. *Nanoscale*, 7(3):924–929.

Guo, X., Du, J., Guo, Y., e Yao, J. (2006). Large-area surface-plasmon polariton interference lithography. *Optics Letters*, 31(17):2613.

Hamm, M., Burlaka, V., Wagner, S., e Pundt, A. (2015). Achieving reversibility of ultra-high mechanical stress by hydrogen loading of thin films. *Applied Physics Letters*, 106(24).

Harrington, R. F. (1993). *Field Computation by Moment Methods*. IEEE.

Hoa, X., Kirk, A., e Tabrizian, M. (2009). Enhanced spr response from patterned immobilization of surface bioreceptors on nano-gratings. *Biosensors and Bioelectronics*, 24(10):3043–3048.

Huang, Z., Yang, W., Zhang, Y., Yin, J., Sun, X., Sun, J., Ren, G., Tian, S., Wang, P., e Wan, H. (2024). Miniaturized electrochemical gas sensor with a functional nanocomposite and thin ionic liquid interface for highly sensitive and rapid detection of hydrogen. *Analytical Chemistry*, 96(45):17960–17968.

Iqbal, T., Noureen, S., Afsheen, S., Khan, M. Y., e Ijaz, M. (2020). Rectangular and sinusoidal au-grating as plasmonic sensor: A comparative study. *Optical Materials*, 99:109530.

Jang, J., Ullal, C., Maldovan, M., Gorishnyy, T., Kooi, S., Koh, C., e Thomas, E. (2007). 3d micro- and nanostructures via interference lithography. *Advanced Functional Materials*, 17(16):3027–3041.

Jeddi Golfazani, A., Alipour, A., Bakhshipour, M., Farmani, A., e Mir, A. (2020). Analytical and numerical models of a highly sensitive mdm plasmonic nano-structure in near-infrared range. *Plasmonics*, 16(2):413–418.

Johnson, P. B. e Christy, R. W. (1972). Optical constants of the noble metals. *Physical Review B*, 6:4370.

Karabchevsky, A., Krasnykov, O., Abdulhalim, I., Hadad, B., Goldner, A., Auslender, M., e Hava, S. (2009). Metal grating on a substrate nanostructure for sensor applications. *Photonics and Nanostructures - Fundamentals and Applications*, 7(4):170–175.

Karlsson, R., Andersson, K., e Wass, C. (2012). Method and system for determination of molecular interaction parameters. *US Patent*, US9316636B2.

Katsuta, H., Farraro, R., e McLellan, R. (1979). The diffusivity of hydrogen in palladium. *Acta Metallurgica*, 27(7):1111–1114.

Kawae, T., Inagaki, Y., Wen, S., Hirota, S., Itou, D., e Kimura, T. (2020). Superconductivity in palladium hydride systems. *Journal of the Physical Society of Japan*, 89(5):051004.

Khavasi, A., Jahromi, A. K., e Mehrany, K. (2008). Longitudinal legendre polynomial expansion of electromagnetic fields for analysis of arbitrary-shaped gratings. *Journal of the Optical Society of America. A, Optics, image science, and vision*, 25 7:1564–73.

Khavasi, A., Mehrany, K., e Rashidian, B. (2007). Three-dimensional diffraction analysis of gratings based on legendre expansion of electromagnetic fields. *Journal of the Optical Society of America B*, 24(10):2676.

Kim, D. (2005). Effect of the azimuthal orientation on the performance of grating-coupled surface-plasmon resonance biosensors. *Applied Optics*, 44(16):3218.

Kim, R. M., Lee, S. M., Han, J. H., Cho, S. H., Lv, J., Im, S. W., Ha, I. H., Lee, Y. H., Lim, D., Kim, H., Cho, N. H., Lee, H.-E., Namgung, S. D., e Nam, K. T. (2024). Helicoid grating-coupled surface plasmon resonance sensor. *Nano Letters*, 24(49):15668–15675.

Kishore, K. e Akbar, S. A. (2020). Evolution of lock-in amplifier as portable sensor interface platform: A review. *IEEE Sensors Journal*, 20(18):10345–10354.

Kissinger, T., James, S. W., e Tatam, R. P. (2017). Simultaneous optical interrogation of multiple tuning fork resonators using range-resolved interferometry. In *2017 IEEE SENSORS*. IEEE.

Klein, E. (1968). Landolt-börnstein: Zahlenwerte und funktionen aus naturwissenschaften und technik. neue serie. gesamtherausgabe: K.-h. hellwege. gruppe ii: Atom- und molekularphysik. band 4: Molekelkonstanten aus mikrowellenspektroskopischen messungen. von barbara starck; herausgeber: K.-h. hellwege und a. m. hellwege. springer-verlag, berlin, heidelberg, new york 1967. ix und 225-seiten. preis: Gebunden dm 110, -. *Berichte der Bunsengesellschaft für physikalische Chemie*, 72(1):121–121.

Klinkhammer, S., Woggon, T., Vannahme, C., Geyer, U., Mappes, T., e Lemmer, U. (2010). Optical spectroscopy with organic semiconductor lasers. *Organic Photonics IV, Proc. SPIE*.

Kluczynski, P., Lundqvist, S., Belahsene, S., Rouillard, Y., Nähle, L., Fischer, M., e Koeth, J. (2012). Detection of propane using tunable diode laser spectroscopy at 3.37 m. *Applied Physics B*, 108(1):183–188.

Koo, W.-T., Cho, H.-J., Kim, D.-H., Kim, Y. H., Shin, H., Penner, R. M., e Kim, I.-D. (2020). Chemiresistive hydrogen sensors: Fundamentals, recent advances, and challenges. *ACS Nano*, 14(11):14284–14322.

Korlapati, N. V. S., Khan, F., Noor, Q., Mirza, S., e Vaddiraju, S. (2022). Review and analysis of pipeline leak detection methods. *Journal of Pipeline Science and Engineering*, 2(4):100074.

Korotcenkov, G., Han, S. D., e Stetter, J. R. (2009). Review of electrochemical hydrogen sensors. *Chemical Reviews*, 109(3):1402–1433.

Kretschmann, E. (1971). Die bestimmung optischer konstanten von metallen durch anregung von oberflächenplasmaschwingungen. *Zeitschrift für Physik A Hadrons and nuclei*, 241(4):313–324.

Laudahn, U., Pundt, A., Bicker, M., v. Hülsen, U., Geyer, U., Wagner, T., e Kirchheim, R. (1999). Hydrogen-induced stress in nb single layers. *Journal of Alloys and Compounds*, 293–295:490–494.

Le, P.-A., Trung, V. D., Nguyen, P. L., Bac Phung, T. V., Natsuki, J., e Natsuki, T. (2023). The current status of hydrogen energy: an overview. *RSC Advances*, 13(40):28262–28287.

Lee, B. G., Belkin, M., Audet, R., Macarthur, J., Diehl, L., Pflugl, C., Capasso, F., Oakley, D., Chapman, D., Napoleone, A., Bour, D., Corzine, S., Höfler, G., e Faist, J. (2007). Widely tunable single-mode quantum cascade laser source for mid-infrared spectroscopy. *Applied Physics Letters*, 91:231101.

Lee, B. G., Belkin, M., Pflügl, C., Diehl, L., Zhang, H., Audet, R., MacArthur, J., Bour, F. I. D. P., Corzine, S., Höfler, G. E., e Capasso, F. I. F. (2009). Dfb quantum cascade laser arrays. *IEEE Journal of Quantum Electronics*, 45:554–565.

Lee, Y., Sim, S.-M., dos Santos, M. R. N., Fernandes, G. D. F., Cavalcanti, G. O., Llamas-Garro, I., Fontana, E., e Kim, J.-M. (2018). Reflectance analysis of the otto chip using an automated reflectometer. In *2018 International Conference on Optical MEMS and Nanophotonics (OMN)*. IEEE.

Lehoucq, R. B., Sorensen, D. C., e Yang, C. (1998). *ARPACK Users' Guide: Solution of Large-Scale Eigenvalue Problems with Implicitly Restarted Arnoldi Methods*. Society for Industrial and Applied Mathematics.

Li, C., He, Y., Qiao, S., e Ma, Y. (2025). A low-cost full-range hydrogen sensor based on quartz tuning fork. *IEEE Sensors Journal*, 25(10):16943–16949.

Li, J., Parchatka, U., e Fischer, H. (2013). Development of field-deployable qcl sensor for simultaneous detection of ambient n2o and co. *Sensors and Actuators B: Chemical*, 182:659–667.

Li, L. e Chandezon, J. (1996). Improvement of the coordinate transformation method for surface-relief gratings with sharp edges. *Journal of The Optical Society of America A-optics Image Science and Vision*, 13:2247–2255.

Li, R., Wu, D., Liu, Y., Yu, L., Yu, Z., e Ye, H. (2017). Infrared plasmonic refractive index sensor with ultra-high figure of merit based on the optimized all-metal grating. *Nanoscale Research Letters*, 12(1).

Liedberg, B., Nylander, C., e Lunström, I. (1983). Surface plasmon resonance for gas detection and biosensing. *Sensors and Actuators*, 4:299–304.

Lin, K., Lu, Y., Chen, J., Zheng, R., Wang, P., e Ming, H. (2008). Surface plasmon resonance hydrogen sensor based on metallic grating with high sensitivity. *Optics Express*, 16(23):18599.

Liu, N., Xu, L., Zhou, S., Zhang, L., e Li, J. (2020). Simultaneous detection of multiple atmospheric components using an nir and mir laser hybrid gas sensing system. *ACS Sensors*, 5(11):3607–3616.

Liu, X., Stefanou, P., Wang, B., Woggon, T., Mappes, T., e Lemmer, U. (2013). Organic semiconductor distributed feedback (dfb) laser as excitation source in raman spectroscopy. *Optics express*, 21 23:28941–7.

Loewen, E. G. e Popov, E. (2018). Diffraction gratings and applications.

Lu, X., Zheng, G., e Zhou, P. (2019). High performance refractive index sensor with stacked two-layer resonant waveguide gratings. *Results in Physics*, 12:759–765.

Luo, Y., An, B., Bai, J., Wang, Y., Cheng, X., Wang, Q., Li, J., Yang, Y., Wu, Z., e Xie, E. (2021). Ultrahigh-response hydrogen sensor based on pdo/nio co-doped in2o3 nanotubes. *Journal of Colloid and Interface Science*, 599:533–542.

Luo, Y., Zhang, C., Zheng, B., Geng, X., e Debliquy, M. (2017). Hydrogen sensors based on noble metal doped metal-oxide semiconductor: A review. *International Journal of Hydrogen Energy*, 42(31):20386–20397.

Luong, H. M., Pham, M. T., Madhogaria, R. P., Phan, M.-H., Larsen, G. K., e Nguyen, T. D. (2020). Bilayer plasmonic nano-lattices for tunable hydrogen sensing platform. *Nano Energy*, 71:104558.

Lyaschuk, Y. M., Kukhtaruk, S. M., Janonis, V., e Korotyeyev, V. V. (2021). Modified rigorous coupled-wave analysis for grating-based plasmonic structures with a delta-thin conductive channel: far- and near-field study. *Journal of the Optical Society of America A*, 38(2):157.

Ma, Y., Qiao, S., Wang, R., He, Y., Fang, C., e Liang, T. (2024). A novel tapered quartz tuning fork-based laser spectroscopy sensing. *Applied Physics Reviews*, 11(4).

Maciel-Neto, J. O., de Freitas Fernandes, G., Cavalcanti, G. O., Llamas-Garro, I., Kim, J.-M., e Fontana, E. (2022). Prospects for developing pressure and tactile sensors based on surface plasmon resonance. *IEEE Sensors Journal*, 22(19):18620–18630.

Maeda, E., Matsuki, T., Yamada, I., e Delaunay, J.-J. (2012). Hole shape effect induced optical response to permittivity change in palladium sub-wavelength hole arrays upon hydrogen exposure. *Journal of Applied Physics*, 111(8).

Maeda, E., Mikuriya, S., Endo, K., Yamada, I., Suda, A., e Delaunay, J.-J. (2009). Optical hydrogen detection with periodic subwavelength palladium hole arrays. *Applied Physics Letters*, 95(13).

Mansouri, M., Mir, A., Farmani, A., e Izadi, M. (2020). Numerical modeling of an integrable and tunable plasmonic pressure sensor with nanostructure grating. *Plasmonics*, 16(1):27–36.

Markel, V. A. (2016a). Introduction to the maxwell garnett approximation: tutorial. *Journal of the Optical Society of America A*, 33(7):1244.

Markel, V. A. (2016b). Introduction to the maxwell garnett approximation: tutorial. *Journal of the Optical Society of America A*, 33(7):1244.

Masson, J.-F. (2020). Portable and field-deployed surface plasmon resonance and plasmonic sensors. *The Analyst*, 145(11):3776–3800.

Matuschek, M., Singh, D. P., Jeong, H., Nesterov, M., Weiss, T., Fischer, P., Neubrech, F., e Liu, N. (2017). Chiral plasmonic hydrogen sensors. *Small*, 14(7).

Melendez, J. L., Carnn, R. A., e Keller, R. C. (1997). Integrally formed surface plasmon resonance sensor. *US Patent*, US5912456.

Michels, W. C. e Curtis, N. L. (1941). A pentode lock-in amplifier of high frequency selectivity. *Review of Scientific Instruments*, 12(9):444–447.

Millar, R. F. (1969). On the rayleigh assumption in scattering by a periodic surface. *Mathematical Proceedings of the Cambridge Philosophical Society*, 65(3):773–791.

Moharam, M. e Gaylord, T. (1982). Diffraction analysis of dielectric surface-relief gratings. *Journal of the Optical Society of America*, 72:1385–1392.

Moharam, M. e Gaylord, T. (1983a). Rigorous coupled-wave analysis of grating diffraction— e-mode polarization and losses. *Journal of the Optical Society of America*, 73:451–455.

Moharam, M. e Gaylord, T. (1983b). Three-dimensional vector coupled-wave analysis of planar-grating diffraction. *Journal of the Optical Society of America*, 73:1105–1112.

Moharam, M. e Gaylord, T. (1986). Rigorous coupled-wave analysis of metallic surface-relief gratings. *Journal of The Optical Society of America A-optics Image Science and Vision*, 3:1780–1787.

Moharam, M. G. e Gaylord, T. K. (1981). Rigorous coupled-wave analysis of planar-grating diffraction. *Journal of the Optical Society of America*, 71(7):811.

Mondal, B., Basumatari, B., Das, J., Roychaudhury, C., Saha, H., e Mukherjee, N. (2014). Zno–sno2 based composite type gas sensor for selective hydrogen sensing. *Sensors and Actuators B: Chemical*, 194:389–396.

Moses, E. I. e Tang, C. L. (1977). High-sensitivity laser wavelength-modulation spectroscopy. *Optics Letters*, 1(4):115.

Neethu, S., Verma, R., Kamble, S., Radhakrishnan, J., Krishnapur, P., e Padaki, V. (2014). Validation of wavelength modulation spectroscopy techniques for oxygen concentration measurement. *Sensors and Actuators B: Chemical*, 192:70–76.

Neto, J. O. M., Cavalcanti, G. O., Llamas-Garro, I., Kim, J.-M., e Fontana, E. (2016). Open otto chip as an SPR pressure transducer. In *2016 URSI Asia-Pacific Radio Science Conference (URSI AP-RASC)*. IEEE.

Nugroho, F. A. A., Eklund, R., Nilsson, S., e Langhammer, C. (2018). A fiber-optic nanoplasmonic hydrogen sensor via pattern-transfer of nanofabricated pdau alloy nanostructures. *Nanoscale*, 10(44):20533–20539.

Nugroho, F. A. A., Iandolo, B., Wagner, J. B., e Langhammer, C. (2016). Bottom-up nanofabrication of supported noble metal alloy nanoparticle arrays for plasmonics. *ACS Nano*, 10(2):2871–2879.

Ohshima, T. e Sasada, H. (1989). 1.5-m dfb semiconductor laser spectroscopy of deuterated water. *Journal of Molecular Spectroscopy*, 136:250–263.

Osamah, S., Fakhri, M. A., Alwahib, A. A., Salim, E. T., Ibrahim, R. K., Mohammed, A.-B. F. A., Gopinath, S. C. B., Qaeed, M. A., Ibrahim, H. I.,

Ahmed, A. S., Shakir, H. A., e Hadi, B. K. (2024). A novel design of symmetrical grating built on d-shaped optical fiber sensor-based surface plasmon resonance. *Advances in Natural Sciences: Nanoscience and Nanotechnology*, 15(3):035015.

Oskooi, A. F., Roundy, D., Ibanescu, M., Bermel, P., Joannopoulos, J., e Johnson, S. G. (2010). Meep: A flexible free-software package for electromagnetic simulations by the fdtd method. *Computer Physics Communications*, 181(3):687–702.

Östergren, I., Pourrahimi, A. M., Darmadi, I., da Silva, R., Stolaś, A., Lerch, S., Berke, B., Guizar-Sicairos, M., Liebi, M., Foli, G., Palermo, V., Minelli, M., Moth-Poulsen, K., Langhammer, C., e Müller, C. (2021). Highly permeable fluorinated polymer nanocomposites for plasmonic hydrogen sensing. *ACS Applied Materials amp; Interfaces*, 13(18):21724–21732.

Otto, A. (1968a). Excitation of nonradiative surface plasma waves in silver by the method of frustrated total reflection. *Zeitschrift für Physik A Hadrons and nuclei*, 216(4):398–410.

Otto, A. (1968b). Excitation of nonradiative surface plasma waves in silver by the method of frustrated total reflection. *Zeitschrift fur Physik A Hadron and nuclei*, 216:398–410.

Palm, K. J., Murray, J. B., Narayan, T. C., e Munday, J. N. (2018). Dynamic optical properties of metal hydrides. *ACS Photonics*, 5(11):4677–4686.

Peisl, H. (1978). *Lattice strains due to hydrogen in metals*, página 53–74. Springer Berlin Heidelberg.

Penner, R. M. (2017). A nose for hydrogen gas: Fast, sensitive h2 sensors using electrodeposited nanomaterials. *Accounts of Chemical Research*, 50(8):1902–1910.

Perrotton, C., Javahiraly, N., Slaman, M., Dam, B., e Meyrueis, P. (2011). Fiber optic surface plasmon resonance sensor based on wavelength modulation for hydrogen sensing. *Optics Express*, 19(S6):A1175.

Perrotton, C., Westerwaal, R. J., Javahiraly, N., Slaman, M., Schreuders, H., Dam, B., e Meyrueis, P. (2013). A reliable, sensitive and fast optical fiber hydrogen sensor based on surface plasmon resonance. *Optics Express*, 21(1):382.

Plumey, J., Guizal, B., e Chandezon, J. (1997). Coordinate transformation method as applied to asymmetric gratings with vertical facets. *Journal of The Optical Society of America A-optics Image Science and Vision*, 14:610–617.

Polo, V., Borotau, P., Lerin, A., e Prat, J. (2014). DFB laser reallocation by thermal wavelength control for statistical udWDM in PONs. In *2014 The European Conference on Optical Communication (ECOC)*. IEEE.

Poole, Z. L., Ohodnicki, P. R., Yan, A., Lin, Y., e Chen, K. P. (2016). Potential to detect hydrogen concentration gradients with palladium infused mesoporous-titania on d-shaped optical fiber. *ACS Sensors*, 2(1):87–91.

Preist, T. W., Harris, J., Wanstall, N. P., e Sambles, J. (1997). Optical response of blazed and overhanging gratings using oblique chandezon transformations. *Journal of Modern Optics*, 44:1073–1080.

Project, T. J. (2025). Julia language documentation (accessed in 24-03-2025).

Pryde, J. A. e Titcomb, C. G. (1969). Solution of hydrogen in niobium. *Transactions of the Faraday Society*, 65:2758.

PubChem (Accessed: 23rd January 2025).

Rao, X., Zhu, H., Wang, X., Chen, Y., Qi, Y., e Yang, H. (2025). High-sensitivity plasmonic refractive index sensor based on embedded gratings with triple self-reference characteristics. *Journal of the Optical Society of America B*, 42(2):431.

Rayleigh, L. (1907). On the dynamical theory of gratings. *Proceedings of the Royal Society of London. Series A, Containing Papers of a Mathematical and Physical Character*, 79(532):399–416.

Ruffato, G., Pasqualotto, E., Sonato, A., Zacco, G., Silvestri, D., Morpurgo, M., De Toni, A., e Romanato, F. (2013). Implementation and testing of a compact and high-resolution sensing device based on grating-coupled surface plasmon resonance with polarization modulation. *Sensors and Actuators B: Chemical*, 185:179–187.

Sasada, H. (1988). 1.5 m dfb semiconductor laser spectroscopy of hcn. *Journal of Chemical Physics*, 88:767–777.

Seliem, Y. e Abdellatif, S. O. (2024). Gratings for enhanced sensitivity: advancing d-shaped optical fiber surface plasmon resonance sensors with ag-fe2o3 structures. *Applied Optics*, 64(9):C11.

Sharma, A. K. e Pandey, A. K. (2019). Design and analysis of plasmonic sensor in communication band with gold grating on nitride substrate. *Superlattices and Microstructures*, 130:369–376.

Shcherbakov, A. (2019). Curvilinear coordinate generalized source method for gratings with sharp edges. *Journal of the Optical Society of America. A, Optics, image science, and vision*, 36 8:1402–1409.

Shcherbakov, A. e Tishchenko, A. (2013). Efficient curvilinear coordinate method for grating diffraction simulation. *Optics express*, 21 21:25236–47.

Shlyagin, M., Manuel, R. M., e Esteban, Ó. (2013). Optical-fiber self-referred refractometer based on fresnel reflection at the fiber tip. *Sensors and Actuators B: Chemical*, 178:263–269.

Sil, D., Gilroy, K. D., Niaux, A., Boulesbaa, A., Neretina, S., e Borguet, E. (2014). Seeing is believing: Hot electron based gold nanoplasmonic optical hydrogen sensor. *ACS Nano*, 8(8):7755–7762.

Silva, S., Coelho, L., Almeida, J. M., Frazao, O., Santos, J. L., Malcata, F. X., Becker, M., Rothhardt, M., e Bartelt, H. (2013). H2 sensing based on a pd-coated tapered-fbg fabricated by duv femtosecond laser technique. *IEEE Photonics Technology Letters*, 25(4):401–403.

Silver, J. A. (1992). Frequency-modulation spectroscopy for trace species detection: theory and comparison among experimental methods. *Applied Optics*, 31(6):707.

Slater, J. C. (1964). Atomic radii in crystals. *The Journal of Chemical Physics*, 41(10):3199–3204.

Sonato, A., Agostini, M., Ruffato, G., Gazzola, E., Liuni, D., Greco, G., Travagliati, M., Cecchini, M., e Romanato, F. (2016). A surface acoustic wave (saw)-enhanced grating-coupling phase-interrogation surface plasmon resonance (spr) microfluidic biosensor. *Lab on a Chip*, 16(7):1224–1233.

Srivastava, S. K. e Abdulhalim, I. (2015). Self-referenced sensor utilizing extra-ordinary optical transmission from metal nanoslits array. *Optics Letters*, 40(10):2425.

Strohfeldt, N., Tittl, A., Schäferling, M., Neubrech, F., Kreibig, U., Griessen, R., e Giessen, H. (2014). Yttrium hydride nanoantennas for active plasmonics. *Nano Letters*, 14(3):1140–1147.

Strohfeldt, N., Zhao, J., Tittl, A., e Giessen, H. (2015). Sensitivity engineering in direct contact palladium-gold nano-sandwich hydrogen sensors [invited]. *Optical Materials Express*, 5(11):2525.

Subramanian, S., Kumar, K., e Dhawan, A. (2020). Palladium-coated narrow groove plasmonic nanogratings for highly sensitive hydrogen sensing. *RSC Advances*, 10(7):4137–4147.

Sun, K., Chao, X., Sur, R., Goldenstein, C. S., Jeffries, J. B., e Hanson, R. K. (2013). Analysis of calibration-free wavelength-scanned wavelength modulation spectroscopy for practical gas sensing using tunable diode lasers. *Measurement Science and Technology*, 24(12):125203.

Sun, X., Shu, X., e Chen, C. (2015). Grating surface plasmon resonance sensor: angular sensitivity, metal oxidization effect of al-based device in optimal structure. *Applied Optics*, 54(6):1548.

Supplee, J. M., Whittaker, E. A., e Lenth, W. (1994). Theoretical description of frequency modulation and wavelength modulation spectroscopy. *Applied Optics*, 33(27):6294.

Sutapun, B. (1999). Pd-coated elastooptic fiber optic bragg grating sensors for multiplexed hydrogen sensing. *Sensors and Actuators B: Chemical*, 60(1):27–34.

Syrenova, S., Wadell, C., Nugroho, F. A. A., Gschneidtner, T. A., Diaz Fernandez, Y. A., Nalin, G., Świtlik, D., Westerlund, F., Antosiewicz, T. J., Zhdanov, V. P., Moth-Poulsen, K., e Langhammer, C. (2015). Hydride formation thermodynamics and hysteresis in individual pd nanocrystals with different size and shape. *Nature Materials*, 14(12):1236–1244.

Tabares, S., Polo, V., e Prat, J. (2022). Fast wavelength thermal tuning of DFB lasers for ultra dense WDM-PONs. *IEEE Photonics Technology Letters*, 34(20):1085–1087.

Tabassum, R. e Gupta, B. D. (2015). Surface plasmon resonance-based fiber-optic hydrogen gas sensor utilizing palladium supported zinc oxide multilayers and their nanocomposite. *Applied Optics*, 54(5):1032.

Thorlabs (2023). Sl10108. `https://www.thorlabs.com/newgrouppage9.cfm?objectgroup_id=12057&pn=SL100061`. Acesso: 2023-30-08.

Tishchenko, A. (2000). Generalized source method: New possibilities for waveguide and grating problems. *Optical and Quantum Electronics*, 32:971–980.

Torcal-Milla, F. J., Harder, I., e Lindlein, N. (2010). Effect of fabrication errors on the diffraction pattern produced by sawtooth gratings. *Applied optics*, 49 9:1599–606.

Torcal-Milla, F. J. e Sanchez-Brea, L. (2016). Diffraction by random ronchi gratings. *Applied optics*, 55 22:5855–9.

Torcal-Milla, F. J. e Sanchez-Brea, L. (2017). Diffraction by gratings with random fill factor. *Applied optics*, 56 18:5253–5257.

Travo, D. A., Muniz, R. A., Liscidini, M., e Sipe, J. E. (2017). Green's function method to study thin diffraction gratings. *Physical Review B*, 96(20).

Trouillet, A., Marin, E., e Veillas, C. (2006). Fibre gratings for hydrogen sensing. *Measurement Science and Technology*, 17(5):1124–1128.

Ueno, Y., Mochizuki, K., Hasegawa, K., e Nogami, M. (2015). Fast wavelength switching with dfb lasers utilizing thermal compensation. In *2015 Opto-Electronics and Communications Conference (OECC)*, página 1–3. IEEE.

Unfricht, D. W., Colpitts, S. L., Fernandez, S. M., e Lynes, M. A. (2005). Grating-coupled surface plasmon resonance: A cell and protein microarray platform. *PROTEOMICS*, 5(17):4432–4442.

Upadhyay, A., Wilson, D., Lengden, M., Chakraborty, A. L., Stewart, G., e Johnstone, W. (2017). Calibration-free WMS using a cw-DFB-QCL, a VCSEL, and an edge-emitting DFB laser with in-situ real-time laser parameter characterization. *IEEE Photonics Journal*, 9(2):1–17.

Vala, M. e Homola, J. (2014). Flexible method based on four-beam interference lithography for fabrication of large areas of perfectly periodic plasmonic arrays. *Optics Express*, 22(15):18778.

Vallius, T. (2002). Comparing the fourier modal method with the c method: analysis of conducting multilevel gratings in tm polarization. *Journal of the Optical Society of America. A, Optics, image science, and vision*, 19 8:1555–62.

van den Berg, P. M. (1981). Reflection by a grating: Rayleigh methods. *Journal of the Optical Society of America*, 71(10):1224.

van den Berg, P. M. e Fokkema, J. T. (1979). The rayleigh hypothesis in the theory of reflection by a grating. *Journal of the Optical Society of America*, 69(1):27.

Wadell, C., Nugroho, F. A. A., Lidström, E., Iandolo, B., Wagner, J. B., e Langhammer, C. (2015). Hysteresis-free nanoplasmonic pd–au alloy hydrogen sensors. *Nano Letters*, 15(5):3563–3570.

Wagner, S., Kramer, T., Uchida, H., Dobron, P., Cizek, J., e Pundt, A. (2016). Mechanical stress and stress release channels in 10–350 nm palladium hydrogen thin films with different micro-structures. *Acta Materialia*, 114:116–125.

Wang, C., Li, J., Luo, C., Wang, X., Yang, M., Xiong, Z., Gu, J., Gong, Z., Wei, Z., e Qian, F. (2025a). Sno2-based resistive hydrogen gas sensor: A comprehensive review from performance to function optimization. *Materials Science in Semiconductor Processing*, 188:109209.

Wang, Q., Zhang, S., Guo, J., e Chen, P. (2024). Advances in highly hydrided palladium. *Frontiers in Materials*, 11.

Wang, R., Sprengel, S., Boehm, G., Baets, R., Amann, M.-C., e Roelkens, G. (2017). Broad wavelength coverage 2.3m iii-v-on-silicon dfb laser array. *Optica*, 4(8):972.

Wang, X., Zhu, J., Wen, X., Wu, X., Wu, Y., Su, Y., Tong, H., Qi, Y., e Yang, H. (2019). Wide range refractive index sensor based on a coupled structure of au nanocubes and au film. *Optical Materials Express*, 9(7):3079.

Wang, X., Zhu, Y., e Gao, W. (2025b). Design of hydrogen sensor relying on pd-mwcnt/wo3 sensing materials for selective and rapid hydrogen detection. *Sensors and Actuators B: Chemical*, 422:136648.

Weber, M., Kim, J.-H., Lee, J.-H., Kim, J.-Y., Iatsunskyi, I., Coy, E., Drobek, M., Julbe, A., Bechelany, M., e Kim, S. S. (2018). High-performance nanowire hydrogen sensors by exploiting the synergistic effect of pd nanoparticles and metal–organic framework membranes. *ACS Applied Materials amp; Interfaces*, 10(40):34765–34773.

Woggon, T., Klinkhammer, S., e Lemmer, U. (2010). Compact spectroscopy system based on tunable organic semiconductor lasers. *Applied Physics B*, 99:47–51.

Xu, B.-Z., Liu, J.-T., Hu, H.-F., Wang, L.-N., Wei, X., e Song, G.-F. (2013). A high sensitivity index sensor based on magnetic plasmon resonance in metallic grating with very narrow slits. *Chinese Physics Letters*, 30(4):040702.

Xu, L., Zhou, S., Liu, N., Zhang, M., Liang, J., e Li, J. (2020). Multigas sensing technique based on quartz crystal tuning fork-enhanced laser spectroscopy. *Analytical Chemistry*, 92(20):14153–14163.

Xu, X. e Li, L. (2014). Simple parameterized coordinate transformation method for deep- and smooth-profile gratings. *Optics letters*, 39 23:6644–7.

Xu, X. e Li, L. (2015). Enlarging applicability domain of the c method with piecewise linear parameterization: gratings of deep and smooth profiles.

Xu, X. e Li, L. (2017). Numerical stability of the c method and a perturbative preconditioning technique to improve convergence. *Journal of the Optical Society of America. A, Optics, image science, and vision*, 34 6:881–891.

Yan, F., Li, L., Wang, R., Tian, H., Liu, J., Liu, J., Tian, F., e Zhang, J. (2019). Ultrasensitive tunable terahertz sensor with graphene plasmonic grating. *Journal of Lightwave Technology*, 37(4):1103–1112.

Yang, F., Wang, T., Deng, X., Dang, J., Huang, Z., Hu, S., Li, Y., e Ouyang, M. (2021). Review on hydrogen safety issues: Incident statistics, hydrogen diffusion, and detonation process. *International Journal of Hydrogen Energy*, 46(61):31467–31488.

Yang, N., Fang, B., Zhao, W., Wang, C., Cheng, F., Hu, X., Chen, Y., Zhang, W., Ma, W., Zhao, G., e Chen, W. (2022). Optical-feedback cavity-enhanced absorption spectroscopy for oh radical detection at 2.8µm using a dfb diode laser. *Optics express*, 30 9:15238–15249.

Yang, Y., She, X., Liu, Z., Zhang, N., Shen, Y., e Jin, C. (2025). Tunable plasmonic system based on disordered palladium nanoparticles and its application to optical hydrogen sensors. *ACS Materials Letters*, 7(3):804–810.

Yang, Z., Zhang, M., Liao, Y., Tian, Q., Li, Q., Zhang, Y., e Zhuang, Z. (2010). Extrinsic fabry–perot interferometric optical fiber hydrogen detection system. *Applied Optics*, 49(15):2736.

Ye, S., Che, M., Kuboki, T., e Kato, K. (2022). Fast wavelength switching at tunable DFB laser array by current/temperature cooperative control. *IEEE Photonics Technology Letters*, 34(1):51–54.

Yesudasu, V., Pradhan, H. S., e Pandya, R. J. (2021). Recent progress in surface plasmon resonance based sensors: A comprehensive review. *Heliyon*, 7(3):e06321.

Yoon, K. H., Shuler, M. L., e Kim, S. J. (2006). Design optimization of nano-grating surface plasmon resonance sensors. *Optics Express*, 14(11):4842.

Yu, R., Xia, H., Pang, T., Wu, B., Li, Z., Sun, P., Guo, Q., Zhang, Z., e Cai, Y. (2023). Simultaneous detection of co2/ch4 based on off-axis integrated cavity output spectroscopy and time-division-multiplexing-based wavelength modulation spectroscopy. *Optics Communications*, 545:129731.

Yu, Z., Jin, L., Chen, L., Li, J., Ran, Y., e Guan, B.-O. (2015). Microfiber bragg grating hydrogen sensors. *IEEE Photonics Technology Letters*, 27(24):2575–2578.

Zeakes, J., Murphy, K., Elshabini-Riad, A., e Claus, R. (1994). Modified extrinsic fabry-perot interferometric hydrogen gas sensor. In *Proceedings of LEOS'94*, volume 2 of *LEOS-94*, página 235–236. IEEE.

Zeller, W., Naehle, L., Fuchs, P., Gerschuetz, F., Hildebrandt, L., e Koeth, J. (2010). Dfb lasers between 760 nm and 16 µm for sensing applications. *Sensors*, 10(4):2492–2510.

Zhang, A., Feng, J., Yan, J., Hu, M., Zhang, L., e Zeng, H. (2022a). Laser reshaping of gold nanoparticles for highly sensitive SERS detection of ciprofloxacin. *Applied Surface Science*, 583:152543.

Zhang, C., Boudiba, A., De Marco, P., Snyders, R., Olivier, M.-G., e Debliquy, M. (2013). Room temperature responses of visible-light illuminated wo3 sensors to no2 in sub-ppm range. *Sensors and Actuators B: Chemical*, 181:395–401.

Zhang, C., Chen, X., Liu, X., Shen, C., Huang, Z., Wang, Z., Lang, T., Zhao, C., Zhang, Y., e Liu, Z. (2022b). High sensitivity hydrogen sensor based on tilted fiber bragg grating coated with pdms/wo3 film. *International Journal of Hydrogen Energy*, 47(9):6415–6420.

Zhao, G., Tan, W., Hou, J., Qiu, X., Ma, W., Li, Z., Dong, L., Zhang, L., Yin, W., Xiao, L., Axner, O., e Jia, S. (2016). Calibration-free wavelength-modulation spectroscopy based on a swiftly determined wavelength-modulation frequency response function of a dfb laser. *Optics express*, 24 2:1723–33.

Zhao, J., Wang, W., Liu, Y., Ma, J., Li, X., Du, Y., e Lu, G. (2011). Ordered mesoporous pd/sno2 synthesized by a nanocasting route for high hydrogen sensing performance. *Sensors and Actuators B: Chemical*, 160(1):604–608.

Zhu, Y., Zhang, H., Li, D., Zhang, Z., Zhang, S., Yi, J., e Wang, W. (2018). Magnetic plasmons in a simple metallic nanogroove array for refractive index sensing. *Optics Express*, 26(7):9148.